Ion outflow and soft X-ray radiation from a micro capillary discharge source and laser produced plasma

Tue N. Hansen

Submitted for the degree of

Doctor of Philosophy

University of Dublin

Trinity College

Department of Physics

October 2001

DECLARATION

This thesis has not been submitted as an exercise for a degree in any other university

This thesis is entirely my own work, except for the advice and assistance mentioned in the acknowledgments

I agree that the library may lend or copy the thesis on request.

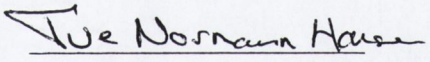

Tue Normann Hansen

October 2001

SUMMARY

This thesis concerns itself with the study of pulsed plasma sources. The plasma is produced either in an electrical discharge or by a laser pulse. The plasma is generated on a nanosecond time scale, after which it evolves due to internal relaxation processes.

The aim of the thesis is to characterise a novel electrical discharge, that proceed by a dielectric surface self-breakdown in vacuum through a preformed micro capillary hole in a dielectric foil separating two circular parallel electrodes. This geometrical constriction helps to pin down the plasma during its early development.

Pulsed power and plasma physics techniques are employed to characterise the plasma evolution. Electrical measurements should be specially designed as the discharge source is operated at several kV. Ion probes and a Thomson parabola analyser are used in the streaming plasma to yield information about the ion flow and charge state. The measurements are correlated with that of a laser produced plasma, which is a more studied source in the literature. Time-resolved spectroscopic investigations were performed as well. This allowed a direct comparison to be made between the deduced initial parameters in a laser produced plasma with that obtained from scaling the measurements done with an ion probe. The scaling follows that of an isentropic hydrodynamic expansion model discussed in the thesis as well.

ACKNOWLEDGEMENTS

I would like to acknowledge the following people for their help and contributions towards the work presented here.

To my supervisor Prof. James G. Lunney, for his guidance throughout the years. And for employing me in the first place and bringing me to Ireland.

To all the people I have met through the FACADIX network. Especially, Senior researcher Dr. Jean Larour for his assistance during the times I worked at LTPT, France, and for proof reading part of this manuscript. And Pierre Loiseleur for his collaboration on the spectroscopic data presented in chapter 4.
For the financial support of the European Commission: TMR contract ERBFMRXCT 980186.

Prof Jørgen Schou for his assistance during the stays in his laboratory at Risø, Denmark, where I worked with electrostatic probes applied to a laser produced plasma.

Of course, the warmest thanks to the lads in the Laser Application Group in Trinity College who were my company throughout the years; Massimo, Juan, Donagh, Eduardo, Brendan, Frederic and Oonagh. You are the ones who really got me through this.

Most of all to my family for supporting my wish in pursuing the Ph.d degree, even if it meant being abroad; "*Tak for alt jeres støtte*".

TABLE OF CONTENTS

CHAPTER 1

Introduction

1.1 Pulsed plasma introduction

This thesis presents a study of the evolution of pulsed plasmas created, respectively, in a high voltage discharge source and in pulsed laser ablation. We have investigated the ion outflow as well as the soft X-ray emission from the hot initial plasma plumes. The soft X-ray region is taken here to represent the wavelength region from about 0.2 – 30 nm or the equivalent of 0.04 – 6.2 keV [Elton 1990].

A plasma is a high-energy state of matter, and since not in equilibrium with its surroundings it will quickly cease to exist. On a microscopic scale the plasma is described by the interactions between the charged ions and electrons through the fields of these particles and their relative velocities. This problem is often simplified so as to treat the plasma as a macroscopic object described by macroscopic charge densities and currents. In this thesis a hydrodynamic isentropic model is employed to describe the macroscopic outflow of the plasma plume. The model was suggested by [Anisimov *et al.* 1993 & 1996] for predicting the plume expansion from a pulsed laser ablation experiment, but extended here to provide the scaling of plasma parameters also for the electrical discharge plasma source. At this level of description the plasma state of the plume is basically only incorporated by the introduction of a reduced effective adiabatic exponent γ.

In the high-energy plasma state electrons and ions will undergo several collisional processes in between free-free, free-bound and bound-bound states. These transitions

are the source of emission of both continuum and line radiation. The recordings of the line emission from the two investigated plasma sources are presented in this thesis. The results are discussed on the basis of theoretical descriptions of the collisional processes in the plasma e.g. [Griem 1997], [Thorne *et al.* 1999].

Both the ion outflow and the radiation emission provide a diagnostic tool of the plasma. Measurements of these features allow one to characterise the processes taking place as the energy equilibrates and is the subject of numerous books, e.g. [Huddlestone & Leonard 1965]. At this level, the generation of a high-energy plasma state and the information deduced from experiments on various atomic processes are of interest from a fundamental physics perspective. There is also a strong interest in pulsed plasma and specifically the soft X-ray emission for technological applications, as described recently by [Attwood 1999] and [Turcu & Dance 1999]. The micro capillary discharge and the laser produced plasma sources investigated here, both represent pulsed plasma sources that have technological and fundamental interest.

1.2 The FACADIX network

The postgraduate study of the author was made possible through the EU-sponsored network: TMR contract no ERBFMRXCT980186, in the 4th framework program on training and mobility of researcher of the European union. The network acronym is "FACADIX" which is a cover for the elaborate title "Soft X-ray Sources of Ultra-high Brightness from Fast Capillary Discharges – Development and Applications".

The network partners are found at the following institutions:

LPTP: Ecole Polytechnique, Palasaieu, France. Dr. Peter Choi (coordinator) and Dr. Jean Larour.

GREMI: Universite d'Orleans, France. Prof. Claude Fleurier.

RUB: Ruhr Universitat Bochum, Germany. Prof. Hans-Joachim Kunze.

BGU: Ben-Gurion University of the Negev, Israel. Prof. Michael Mond.

ISAN: Russian Academy of Science, Russia. Prof Konstatin Koshelev.

There are two industrial partners involved as well, they are:

JCS: John Count Scientific Ltd. Great Britain. Mr. John Count.

EPPRA: France. Dr. Peter Choi.

The project aim is to investigate the use of capillary discharges as sources of both coherent and incoherent soft X-rays.

Table 1.1: FACADIX network tasks.

Characterisation of ionisation growth in long capillary discharge
Development of a laser ablation scheme for filling the capillary
Optimisation of hollow cathode geometry for on axis current initiation
Creation of optically thick atomic species in a long capillary discharge
Development of a hybrid 2-D fluid code to model discharge formation
Development of atomic physics model for plasma modelling
Development of gain guiding formalism for high aspect ratio lasing medium
Development of an ultra-fast energy storage scheme for driving capillary discharge
Development of an ultra-fast (ns) time and space resolved VUV spectrograph
Development of an ultra-fast (ns) time and space resolved soft X-ray spectrograph
Development of an ultra-fast (ns) time and 2-D space resolved soft X-ray camera
Development of soft X-ray absorption spectroscopy diagnostics
Development of tomographic plasma backlighting diagnostics
Development of a soft X-ray laser based on the collisional Ne-like scheme
Development of a soft X-ray amplifier
Development of a pseudo Plancian soft X-ray source
Development of an ultra-bright soft X-ray source
Development of a soft X-ray laser based on the recombination scheme
2-D MH simulation of capillary discharge formation

To achieve this several tasks have been identified as necessary for the network to collaborate on, these tasks are reproduced in Table 1.1. This table is not meant to indicate that the author is familiar with all of them or that they will all be discussed in this thesis – it is merely to give an impression of the overall network. With reference to Table 1.1 it can be said that the network partners have an extensive experience in plasma physics and more specifically high voltage capillary discharges. During the time of the contract, this experience manifested itself in notably the demonstration of soft X-ray lasing on the Carbon VI Balmer-α line at 18.22 nm [Ellwi *et al.* 2001] at the group of H-J. Kunze (RUB).

1.3 Summary of chapters

Chapter 2

We present the isentropic hydrodynamic expansion model for a plume into vacuum by Anisimov *et al.* This model, though a gas dynamic model, has been shown throughout this thesis to give a good description of the expansion from the pulsed plasma sources. A discussion based on a problem treated by Zel'dovich and Raizer on the relationship between the expansion velocities is detailed as well.

As we work with plasmas the second part of chapter 2 is used to introduce the necessary plasma formulary. A simple way of establishing the average ionisation in the plasma is discussed and compared to a calculation performed using a plasma physics computer code "FLY".

Chapter 3

The micro capillary discharge plasma source is at first described and the basic experimental arrangements, common to the later investigations, are presented. Characterisation of the electrical breakdown phase is done from electrical measurements.

Electrostatic probe (Langmuir probe) measurements at various distances are presented. Results are correlated with the hydrodynamic expansion model from chapter 2.

We describe the construction and implementation of a Thomson parabola analyser used with the micro capillary discharge to provide *charged resolved* time-of-flight information, something not possible with the electrostatic probes. The Thomson parabola analyser confirms the velocity measurements obtained with the probes and we present the (partial) charge velocity distribution in the late stage of the expanding plume.

Chapter 4

The soft X-ray emission of pulsed plasma sources is investigated using time-resolved emission spectroscopy in the wavelength region from ~10 - 40 nm. Measurements from a laser produced plasma source and the micro capillary plasma source are presented.

For a laser produced carbon plasma the detailed time evolution of the plasma parameters (electron temperature and density) is obtained from spectral investigations using the FLY-code. Again, a discussion of the results based on the scaling of the hydrodynamic model of chapter 2 is performed. The temporal

evolution of the spectrum from a micro capillary discharge cell equipped with a Mylar dielectric is presented and spectral line information is discussed.

Chapter 5

This chapter is used to first present the "classic" use of the expansion model of Chapter 2 to describe the asymptotic inertial expansion from a plane target of a laser produced plasma plume generated at low laser pulse energy. This is followed by the results of an investigation made on laser ablation with a modified target geometry, where the initial plume expansion is constricted.

Chapter 6

Partial conclusions from throughout the thesis are summarised.

Appendix A

Presents the computer code for solving the coupled differential equations of the hydrodynamic expansion model.

Appendix B

A discussion of a series of laser ablation experiments, where the angular distribution of the expanding plume is measured using ion probes, for different metal targets at different laser pulse energy densities on the target.

References

[chap 1] Anisimov S.I. Bäuerle D. and Luk'yanchuk B.S. (1993) "*Gas dynamics and film profiles in pulsed-laser deposition of materials*". Phys. Rev. B **48**(16) pp 12076.

[chap 1] Anisimov S.I. Luk'yanchuk B.S. and Luches A. (1996) "*An analytical model for three-dimensional laser plume expansion into vacuum in hydrodynamic regime*". Appl. Surf. Sci. **96-98** pp 24.

[chap 1] Attwood D. (1999). "*Soft X-rays and extreme ultraviolet radiation: principles and applications*". (Cambridge University Press).

[chap 1] Ellwi S.S. Juschkin L. Ferri S. Kunze H-J. Koshelev K.N. and Louis E. (2001). "*X-ray lasing as a result of an induced instability in an ablative capillary discharge*". J. Phys. D: Appl. Phys. **34**, pp 336.

[chap 1] Elton R.C. (1990). "*X-ray lasers*". (Academic Press, Ltd).

[chap 1] Griem H.R. (1997). "*Principles of plasma spectroscopy*". (Cambridge University Press).

[chap 1] Huddlestone R.H. and Leonard S.L. (1965). "*Plasma diagnostic techniques*". (Academic Press).

[chap 1] Thorne A. Litzen U. and Johansson S. (1999). "*Spectrophysics – Principles and Applications*". (Springer-Verlag).

[chap 1] Turcu I.C.E. and Dance J.B. (1999). "*X-ray From Laser Plasmas: Generation and Applications*". (John Wiley & Sons Ltd).

CHAPTER 2

Theory

The experiments described in this thesis concern *pulsed* plasmas formed in a "semi-constricted" geometry where the plasma typically has some areas in contact with a "cold" wall but at least one direction open to expand freely into vacuum. To form the initial plasma two kinds of external energy sources are used, either a pulsed *electrical discharge* or a pulsed *laser ablation*. However, the typical time scale over which the external energy input is deposited in the plume is of the same order of magnitude, some ~1 – 10 ns.

Obviously the details of how the deposited energy is coupled with the release of a volume of particles, where subsequent further interactions take place with the end results that a volume of plasma is created, differ substantially in the two cases. The novel electrical discharge microcapillary setup described in Chapter 3 is being modelled using a magneto-hydrodynamic model (MHD-model) [Chetry and Mond 2001]. For the case of pulsed laser interaction with matter, many references exist but we can mention [Torcu and Dance 1999] and [Phipps and Dreyfus 1993].

After the first ~10 ns, the energy input to the plume ceases and the plasma evolves due to internal processes. These include various collision and recombination processes, that will be dealt with later in this chapter, and which are of importance for e.g. interpreting the spectroscopic observations. The expansion into the free dimension may take place due to internal pressure forces or electric fields. Short of being able to treat the full kinetic theoretical problem, different simplified models are

presented below. Chapter 2.1 starts with the hydrodynamic description of a gas cloud.

2.1: Hydrodynamic expansion model

As given in [Zel'dovich and Raizer 1967] the three conservation equations of hydrodynamics can be written as:

(Continuity equation) $$\frac{D\rho}{Dt} + \rho\nabla \bullet \mathbf{u} = 0 \tag{2.1}$$

(Equation of motion) $$\rho\frac{D\mathbf{u}}{Dt} = -\nabla p \tag{2.2}$$

(Energy equation) $$\frac{D\varepsilon}{Dt} + p\frac{DV}{Dt} = Q \tag{2.3}$$

Where ρ, p, ε, $\mathbf{u}$, V and Q are the mass density, pressure, specific internal energy, fluid velocity, specific volume (V=1/ρ) and external power source per unit mass of the material, respectively. The total derivative, D/Dt, describing the time change in any parameter following a moving fluid particle, is related to the partial derivative at a specific point of space and time by:

$$\frac{D}{Dt} = \frac{\partial}{\partial t} + \mathbf{u} \bullet \nabla \tag{2.4}$$

In the formalism presented here no account has been made for viscosity or thermal conductivity.

2.1.1 Isentropic hydrodynamic expansion model by Anisimov

This section is used to present the hydrodynamic expansion model first discussed by Anisimov [Anisimov *et al.* 1993, 1996]. It describes the expansion of a

gas plume into vacuum in terms of a special set of elliptical solutions to the three hydrodynamic conservation equations given in Eq (2.1-3).

It is assumed that a gas cloud is formed on a target surface located at z = 0 (Figure 2.1). The cloud expands into vacuum on a time scale much longer than the time of formation. The vapour is considered as an ideal gas with a constant adiabatic index $\gamma = c_p/c_v$, hence the equation of state for a perfect gas holds:

$$p = nk_BT \tag{2.5}$$

where n is the particle density, and T the temperature. Further it is assumed that $Q = 0$ hence the cloud expands adiabatically into vacuum. And the fluid is taken to be in thermodynamic equilibrium, so that the relation holds

$$T\mathrm{d}S = \mathrm{d}\varepsilon + p\mathrm{d}V \tag{2.6}$$

where S is the entropy per unit mass.

In this case the three equations (2.1) – (2.3) can be re-written [Anisimov *et al.* 1996]

$$\frac{\partial \rho}{\partial t} + \nabla \bullet (\rho \mathbf{u}) = 0 \ , \ \frac{\partial \mathbf{u}}{\partial t} + (\mathbf{u} \bullet \nabla)\mathbf{u} + \frac{\nabla p}{\rho} = 0 \ , \ \frac{\partial S}{\partial t} + (\mathbf{u} \bullet \nabla)S = 0 \tag{2.7}$$

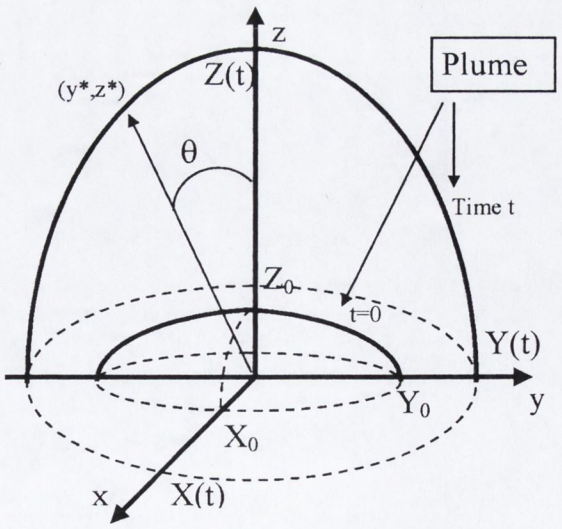

Figure 2.1: Definition of the gas cloud coordinates in the hydrodynamic model by Anisimov. X_0,Y_0 and Z_0 are the initial values of X(t), Y(t) and Z(t) the boundary coordinates of the cloud.

That allows for the description of an isentropic expansion of the gas plume into vacuum with a zero temperature at the cloud boundary, a physically more correct model than the assumption of an isothermal cloud, see discussion in [Anisimov *et al.* 1996].

The special solution to the set of equations (2.7) and (2.5) constrains the flow parameters to be constant on elliptical surfaces. For further reading on this class of solution see e.g. [Dyson 1968] and more recently [Gaffet 1996]. Here we present the theory as given by [Anisimov *et al.* 1993, 1996]. The solution to the above hydrodynamic equations for the flow parameters, in an *isentropic* expansion, can be written as:

$$
\begin{aligned}
n(x,y,z,t) &= \frac{N_0}{I_1 X(t)Y(t)Z(t)}\left[1-\left(\frac{x}{X(t)}\right)^2-\left(\frac{y}{Y(t)}\right)^2-\left(\frac{z}{Z(t)}\right)^2\right]^{1/(\gamma-1)} \\
p(x,y,z,t) &= \frac{E_0}{I_2 X(t)Y(t)Z(t)}\left[\frac{X_0Y_0Z_0}{XYZ}\right]^{\gamma-1}\left[1-\left(\frac{x}{X(t)}\right)^2-\left(\frac{y}{Y(t)}\right)^2-\left(\frac{z}{Z(t)}\right)^2\right]^{\gamma/(\gamma-1)} \\
S(x,y,z,t) &= \frac{1}{\gamma-1}\ln\left[\frac{E_0}{I_2 X_0Y_0Z_0}\left(\frac{I_1 X_0Y_0Z_0}{M}\right)^{\gamma}\left(1-\left(\frac{x}{X(t)}\right)^2-\left(\frac{y}{Y(t)}\right)^2-\left(\frac{z}{Z(t)}\right)^2\right)\right]
\end{aligned}
\qquad (2.8)
$$

Here $N_0 = \int n(\mathbf{r},t)dV$ and $E_0 = (\gamma-1)^{-1}\int p(\mathbf{r},t)dV$ are the initial number of particles and the initial energy of the vapour plume respectively. I_1 and I_2 are functions of γ, the adiabatic exponent, and from their definition it follows that $I_1/I_2 = (5\gamma\text{-}3)(\gamma\text{-}1) / (2\gamma)$ for an isentropic plume. The functions are shown in Figure 2.2. X, Y and Z are the plume boundaries along the coordinate axes. With the solution (2.8) inserted into (2.7) the problem reduces to that of three coupled ordinary differential equations:

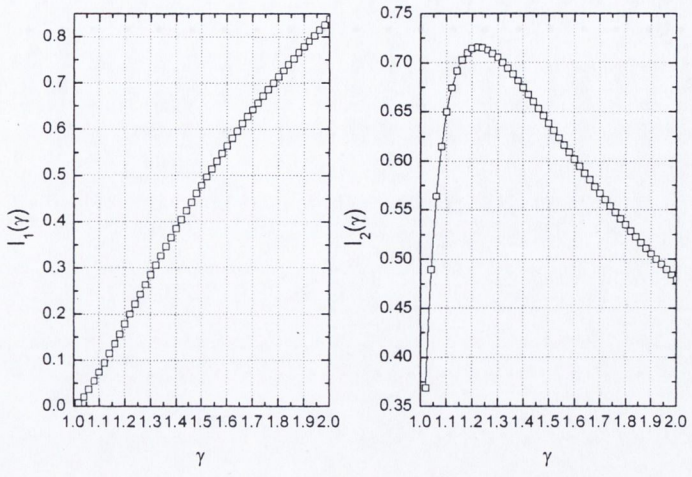

Figure 2.2: Plot of the functions $I_1(\gamma)$ and $I_2(\gamma)$.

$$\frac{X}{\beta}\frac{\partial^2 X}{\partial t^2} = \frac{Y}{\beta}\frac{\partial^2 Y}{\partial t^2} = \frac{Z}{\beta}\frac{\partial^2 Z}{\partial t^2} = \left[\frac{X_0 Y_0 Z_0}{XYZ}\right]^{\gamma-1}, \tag{2.9}$$

where $\beta = (5\gamma\text{-}3)E_0/M$ and M is the total mass of the initial cloud. Equation (2.9) is to be solved with the initial conditions $X(0) = X_0$, $Y(0) = Y_0$, $Z(0) = Z_0$ and $\dot{X}(0) = \dot{Y}(0) = \dot{Z}(0) = 0$, that is the initial kinetic energy is disregarded compared to the internal energy. It was tested that this is a good assumption by running the model with an initial velocity along the Z-axis of the order of the typical sound velocity present in the plume in the experiments. The asymptotic angular distribution is only marginally changed compared to the case with no initial velocity.

We have solved Equation (2.9) using a fourth order Runge-Kutta-Nyström method, the typical results of which are shown in Figure 2.3. Details of the program and the mathematical method used are given in Appendix A. If we focus the attention on measurements in say just the *y-z* plane of Figure 2.1 we can write the following expressions for:

(Particle flux) $$j(y,z,t) = \frac{N_0}{I_1 XYZ}\left[1-\left(\frac{y}{Y}\right)^2-\left(\frac{z}{Z}\right)^2\right]^{1/(\gamma-1)}\left(v_y^2+v_z^2\right)^{1/2} \quad (2.10)$$

(Temperature) $$k_B T = \varepsilon\frac{(5\gamma-3)(\gamma-1)}{2\gamma}\left[\frac{X_0 Y_0 Z_0}{XYZ}\right]^{\gamma-1}\left[1-\left(\frac{y}{Y}\right)^2-\left(\frac{z}{Z}\right)^2\right] \quad (2.11)$$

For future reference we note here, that when using (2.11) in a plasma, the left hand side is exchanged for $(\bar{Z}+1)k_B T$, with $\bar{Z}$ being the mean ion charge. For the number of particles arriving per unit area normal to the flow, $F = \int nvdt$, we obtain the normalised angular emission in the y-z plane (this function is shown in [Hansen *et al.* 1999] as well), here θ is the angle measured from the target normal, see Figure 2.1:

$$F(\theta)/F(0) = \cos^{-3}\theta\left[1+\left(\frac{Z_{\inf}}{Y_{\inf}}\right)^2\tan^2\theta\right]^{-3/2} \quad (2.12)$$

The constant Z_{inf}/Y_{inf} is the ratio of Z/Y as $t \rightarrow \infty$. The velocities in Equation (2.10) at any given point (x,y,z) follow from the affine transformation:

$$\begin{pmatrix} v_x \\ v_y \\ v_z \end{pmatrix} = \begin{pmatrix} X^{-1}\partial X/\partial t & 0 & 0 \\ 0 & Y^{-1}\partial Y/\partial t & 0 \\ 0 & 0 & Z^{-1}\partial Z/\partial t \end{pmatrix}\begin{pmatrix} x \\ y \\ z \end{pmatrix} \quad (2.13)$$

Figure 2.3 shows a typical output from modelling laser ablation of silver in vacuum [Hansen *et al.* 1999] carried out in collaboration with the group of Prof. J. Schou at Risø National Laboratory, Denmark. The dimensionless time $\tau = t\beta^{1/2}X_0$ is used on the abscissa. It is observed that at late times ($\tau > 10$ or >1 μs in this experiment) the expansion becomes inertial and the boundary coordinates increases linearly in time. Here β is defined by $\beta = (5\gamma\text{-}3)\varepsilon$, with ε again the specific energy.

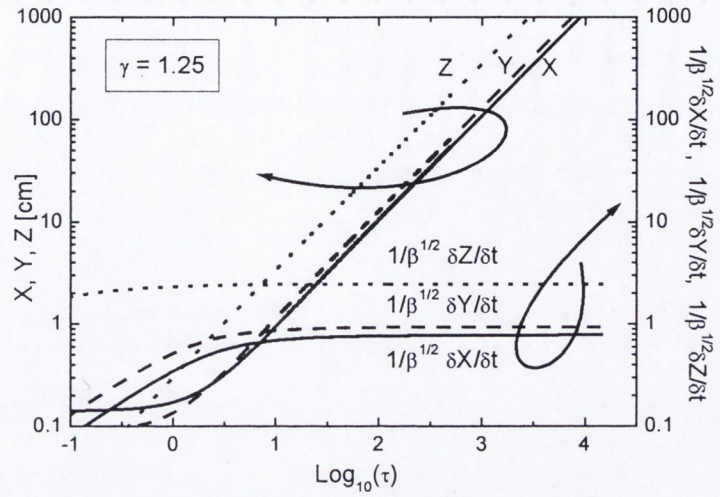

Figure 2.3: Gas plume boundaries as a function of dimensionless time calculated from the model of Anisimov for a laser ablation experiment of silver in vacuum. $X_0 = 1.4$ mm $Y_0 = 0.9$ mm $Z_0 = 0.016$ mm [Hansen *et al.* 1999].

The initial physical dimensions of the plume are the only input to the model. In a laser ablation experiment, the lateral dimensions X_0 and Y_0 can be measured from the laser spot on the target. The height over the target can be calculated indirectly from an estimate of the initial sound velocity, $c_{s,0}$, in the plume according to:

$$Z_0 = c_{s,0} \times \tau_{laser} \tag{2.14}$$

where τ_{laser} is the FWHM width of the laser pulse. The way to estimate the sound velocity from the front velocity, v_{front}, of the observed particle time-of-flight spectrum in the free flight region is discussed in the next section.

2.1.2 The asymptotic expansion velocity

The sound velocity in the initial plume, $c_{s,0}$, is formally given by:

$$c_{s,0} = \left(\gamma \frac{p_0}{\rho_0} \right)^{1/2} = \left(\gamma(\gamma - 1)\varepsilon_0 \right)^{1/2} \tag{2.15}$$

where $\varepsilon = E_0/M$ is again the specific energy as defined after Eq. (2.1-3). Zel'dovich and Raizer [Zel'dovich and Raizer 1967, pp 106] discussed the problem of a self-similar, isentropic solution to the sudden expansion of a spherical gas cloud into vacuum. In this case the velocity is a linear function, $u = \dot{R}r/R$ and $\rho = \rho_c\left(1 - r^2/R^2\right)^{1/(\gamma-1)}$ (compare with n in (2.8)). The density at the centre ρ_c, found from the integration $M = \int_0^R \rho 4\pi r^2 dr$, can be expressed as:

$$\rho_c = \frac{\Gamma\left(\gamma/(\gamma-1)+3/2\right)}{\Gamma\left(\gamma/(\gamma-1)\right)\Gamma(3/2)}\frac{M}{2\pi R^3} \tag{2.16}$$

where Γ is the gamma function. Calculating the integral $E = \int_0^R \frac{\rho u^2}{2} 4\pi r^2 dr$ and using Eq. (2.16), we arrive at a relationship between the sound velocity and the front velocity $v_{front} = \dot{R}$.

$$c_{s,0} = \left(\frac{3\gamma(\gamma-1)}{4}\frac{\Gamma\left(\gamma/(\gamma-1)+3/2\right)}{\Gamma\left(\gamma/(\gamma-1)+5/2\right)}\right)^{1/2} v_{front} \tag{2.17}.$$

From this expression it follows that $v_{front}/(2E/M)^{1/2} = 1.92$ at $\gamma = 4/3$ as stated as well by Zel'dovich and Raizer.

Using the model of Anisimov *et al.* presented in the last section, we can also establish the relationship between the asymptotic plume-front velocity and the initial sound velocity. At late times we see in Figure 2.3 that $\beta^{-1/2}\,\mathrm{d}Z/\mathrm{d}t$ approach a constant value, here named k_∞. Hence setting $v_{front} = \mathrm{d}Z/\mathrm{d}t$ we find that:

$$c_{s,0} = \frac{1}{k_\infty}\left(\frac{\gamma(\gamma-1)}{5\gamma-3}\right)^{1/2} v_{front} \tag{2.18}.$$

Here we have used the definition for β discussed after (2.13).

If we assume an initial symmetric plume $X_0=Y_0=Z_0$ the result of Eq. (2.18), when running Anisimov's model Eq. (2.9), corresponds to (2.17) for different values of gamma. This is shown if Figure 2.4. Shown as well in Figure 2.4 is the solution to the model of Anisimov, assuming an initial "plane" plume $X_0=Y_0=100\times Z_0$. For the "plane" expansion, we observe that the plume-front velocity (measured along the *z*-axis) is higher for a given initial sound velocity. This is an indication of the strong initial pressure gradient along the expansion direction.

Finally, we mention that for the case of hydrodynamic outflow of a gas from a container, the maximum escape velocity of the plume front is given by [Zeld'dovich and Raizer 1967] and [Kelly and Miotello 1993]:

$$c_{s,0} = \frac{\gamma - 1}{2} v_{front} \tag{2.19}$$

This ratio is calculated in Figure 2.4 as well. At a γ-value of ~1.25 which we use to describe the plasma the result of Eq's (2.19) and (2.18) is very close.

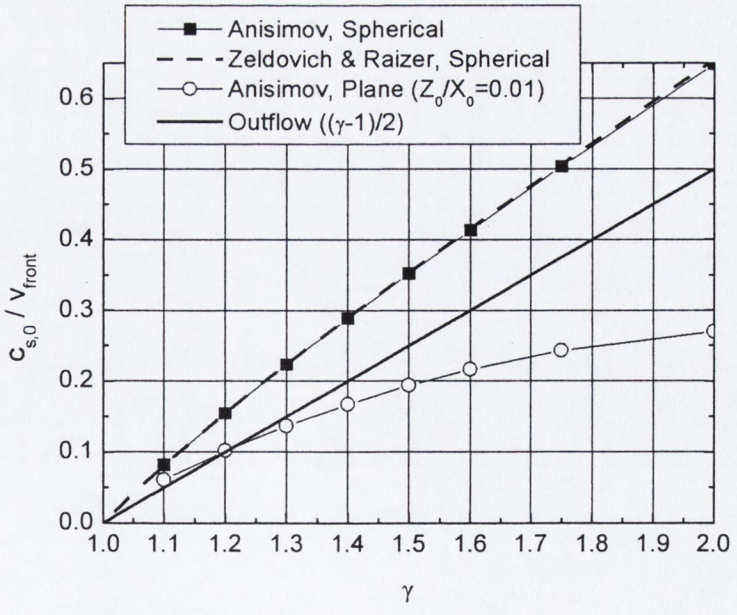

Figure 2.4: Proportionality factor for expansion of a gas cloud into vacuum according to models discussed in the text.

2.2: Processes in a plasma

2.2.1 Sound velocity and ionic charge state in a plasma

The theory presented in the previous section is based on a hydrodynamic description of the plume. It was shown, that the inertial expansion velocity of the plume is related to the initial sound velocity in the plasma. Hence, measurement in the late stage of expansion of the plume can be used to infer information about the initial plume properties. Equation (2.15) gave the formal definition of the sound velocity. In a plasma we should take into account, that both electrons and ions can contribute to the pressure hence $p_0 = (n_i k_B T_i + n_e k_B T_e)$. If we assume the plasma is macroscopically charge neutral ($n_e = \overline{Z}\, n_i$) and if we further assume the ion and electron temperatures are equal, we arrive at the expression for the adiabatic sound velocity [Phipps & Dreyfus 1993]:

$$c_{s,0} = \left(\frac{\gamma\left(\overline{Z}+1\right)k_B T_e}{m_{ion}} \right)^{1/2} \qquad (2.20).$$

The ion and electron temperatures are equal if there is sufficient time for equilibration to be established between the two particle distributions. In most plasmas $T_e >> T_i$ and the expression (2.20) is modified by excluding the +1 factor in the parenthesis.

A mean ionisation, $\overline{Z}$, is often attributed to the plasma. We shall in the following estimate the mean ionisation using two different approaches. One is the semi-analytical approach by [Zel'dovich & Raizer 1966, pp 201], the other using the plasma physics code "FLY" by Richard W. Lee [Lee 1995], see also section 2.2.3.

The approximation by Zel'dovich and Raizer starts with the Saha-equation relating the particle populations of the various ionisation stages in the plasma. The plasma is thus assumed to be in local thermodynamic equilibrium (LTE), see later. The Saha equation states that

$$\frac{n_e n_{m+1,g}}{n_{m,g}} = 2\frac{g_{m+1,g}}{g_{m,g}}\left(\frac{2\pi m_e k_B T_e}{h^2}\right)^{3/2} \exp\left(-\frac{I_{m+1}}{k_B T_e}\right) \qquad (2.21).$$

Here n_e and n_m are the electron density and ion density of the m ionised ion (a neutral atom has $m = 0$). The term $g_{m,g}$ is the statistical weight of an m-ion in its ground state and I_{m+1} is the ionisation potential of the m-ion in its ground state.

There are two steps in the argument of Zel'dovich and Raizer. *First* it is assumed that n_m and I_{m+1} are continuous functions of m. This is done by interpolating between the points in a graph of I_{m+1} and m and writing $n_{m+1} = n_m + (dn/dm)$ whereby equation (2.21) becomes

$$\left(1+\frac{d\ln n}{dm}\right)n_e = 6\times10^{21}\left(T_{e[eV]}\right)^{3/2} \exp\left(-\frac{I_{m+1[eV]}}{T_{e[eV]}}\right) \qquad (2.22).$$

Here the density is in cm^{-3} and it is assumed that the ratio of the statistical weights is ~1. The *second* step is to assume that the average value of the ionic charge, $\overline{Z}$, is equal to the value m_{max} where the function $n(m)$ has a maximum. The narrower and more sharp this peak is, the better the approximation. Finally Zel'dovich and Raizer argue that the average value of the ionisation potential should be referred to the point $m + ½$ on the graph of I_{m+1} *vs.* m. The end result of their analysis is the following transcendental equation, which can be used to predict the mean ionisation $\overline{Z}$:

$$I\left(Z+\tfrac{1}{2}\right) = T_{e[eV]} \ln\left(\frac{6\times10^{21}T_{e[eV]}^{3/2}}{Zn}\right) \qquad (2.23).$$

Starting with a value of m, the right hand side can be calculated ($Z = m$). Then using the interpolation curve of I_{m+1} *vs.* m a new value of m is found and this is continued until the value converges. This is then the average ionic charge $\overline{Z}$. Figure 2.5 illustrates the results of this procedure for a range of plasma parameters in a carbon plasma. Also shown is the result from running the FLY-code assuming LTE. In the code the various ion populations are calculated taking into account the detailed level structure for the H, He and Li-like ion stages while only including the ground state and ionisation potential for Be-like ions up to the neutral ion [Lee 1995]. The FLY code calculates in detail all the collisional and radiative rates and level populations. We note, that due to the large ionisation potential of the He-like ion $m = +4$, the mean ionic charge is +4 over wide range of densities and temperatures.

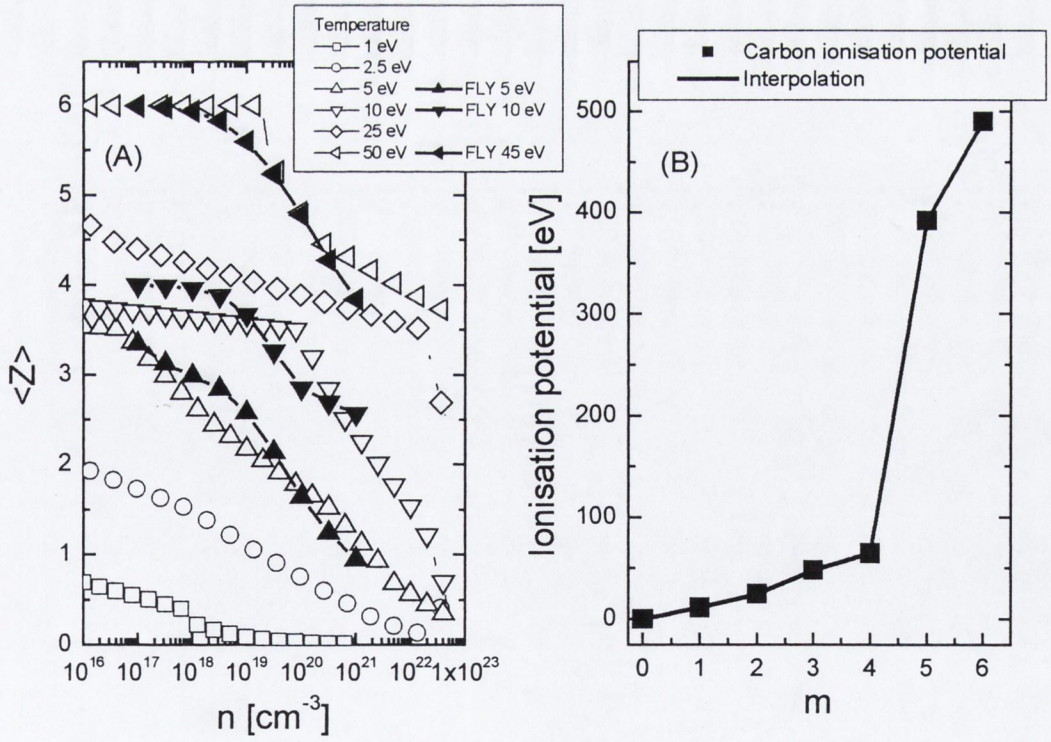

Figure 2.5: (A) Open symbols, average ionic charge calculated using (2.23), closed symbols, average ionic charge from the FLY code [Lee 1995]. (B) Interpolation curve to the ionisation potential used with (2.23) for the calculations in (A).

We conclude that the results of the simple transcendental equation (2.23) are close to that obtained from the more thorough treatment in the FLY-program. The average ionic charge drops at high densities for a given temperature. However, for very high particle density the mean ion charge would increase sharply because of "pressure ionisation" due to lowering of the binding energy of the outer bounded electrons [Anders 1997]. This reduction in the binding energy of the bound electron comes about due to Coulomb interactions with the surrounding charged particles but is not included in the two models presented above.

2.2.2 Plasma equilibrium

Various collisional and radiative processes take place in the plasma. The combined effect of these determines e.g. the emitted radiation that is recorded in spectroscopy. Following [Hutchinson 1987] the rate coefficients are written $<\sigma v>$ where σ is the cross section for the process and $<\sigma v>$ is averaged over the (Maxwellian-) velocity distribution.

The rate coefficients for radiative recombination, collisional ionisation, collisional excitation and dielectronic recombination are taken from [Hutchinson 1987]. As an approximation to the expression for the *total radiative recombination* rate to all levels we have:

$$\langle \sigma_r v \rangle \approx 5.2\times10^{-20}\,\frac{Z}{2}\left(\frac{Z^2 I_H}{k_B T_e}\right)^{1/2}\left(1-\exp\left\{\frac{-\chi_i}{k_B T_e}\left(1+\frac{1}{n_0}\left[\frac{\xi}{n_0^2}-1\right]\right)\right\}\right)\left(\left[\ln\frac{\chi_i}{k_B T_e}\right]^2+2\right)^{1/2}$$

[$m^3\ s^{-1}$] (2.24).

The term I_H is the hydrogen ionisation potential (13.6 eV), n_0 is the principal quantum number of the lowest incomplete shell of the ion, ξ is the number of holes available in the shell and χ_i the ionisation potential of the recombined ion.

The *collisional ionisation* rate coefficient per electron is written

$$\langle \sigma_i v \rangle \approx \bar{g}\left(1.74\times10^{-14}\right)\left(\frac{I_H}{\chi_i}\right)^2\left(\frac{k_B T_e}{I_H}\right)^{1/2}\left(1-\exp\left(-\frac{5\chi_i}{k_B T_e}\right)\right)\exp\left(\frac{-\chi_i}{k_B T_e}\right)$$

$[\mathrm{m^3\ s^{-1}}]$ (2.25),

where g is the Gaunt factor. Hutchinson suggests the semi-empirical relation for this factor $g = 1+(3^{1/2}/\pi)\ln(1+k_B T_e/\chi_i)$.

The expression adopted for the rate coefficient of *collisional excitation* is:

$$\langle \sigma_{ij} v \rangle \approx 3.15\times10^{-13}\,\bar{g} f_{ij}\,\frac{I_H}{E_{ij}}\left(\frac{I_H}{k_B T_e}\right)^{1/2}\exp\left(\frac{-E_{ij}}{k_B T_e}\right)\ [\mathrm{m^3\ s^{-1}}] \qquad (2.26).$$

Here f_{ij} is the oscillator strength of the transition while the Gaunt factor is again approximated with a simple expression $g = g_t+(3^{1/2}/\pi)\ln(1+k_B T_e/E_{ij})$. The value of g_t can be roughly taken as 0.2 when $E_{ij} \sim \chi_n$ and 1 when $E_{ij} << \chi_n$.

Finally, the rate coefficient for *dielectronic recombination,* in which an m-ion resonantly captures an electron to form a doubly excited state in the (m-1)-ion which then performs a radiative decay to stabilise, is given as:

$$\langle \sigma_d v \rangle \approx 8.8\times10^{-18}\, f_{ij} Z^{2/3}\,\frac{E_{ij}}{I_H}\left(\frac{I_H}{k_B T_e}\right)^{3/2}\exp\left(\frac{-E_{ij}}{k_B T_e}\right)\ [\mathrm{m^3\ s^{-1}}] \qquad (2.27).$$

All of the mentioned rate coefficients have an inverse process connected with them i.e. the collisional ionisation is competing with 3-body recombination (also called collisional recombination). Different plasma equilibrium models assume different relative strength of these various processes.

The first plasma equilibrium model to be mentioned here is that of *local thermodynamic equilibrium* (LTE). It assumes that transitions between states are dominated by collisional as opposed to radiative processes. In LTE the Saha equation given in (2.23) relates the ground state populations of different ionisation stages while the Boltzmann equation gives the relative population of the different bound levels in the ion, see [McWhirter 1965]:

$$\frac{n_i}{n_j} = \frac{g_i}{g_j} \exp\left(\frac{-E_{ij}}{k_B T_e}\right) \qquad (2.28).$$

A necessary but not sufficient condition for a transition to be in LTE, formulated by [McWhirter 1965], is that the collisional rates must be at least a factor 10 times the radiative rates, which can be formulated as

$$n_e n_i \left\langle \sigma_{ji} v \right\rangle \geq 10 n_i A_{ij} \qquad (2.29)$$

where A_{ij} is the bound-bound radiative rate coefficient (the "Einstein A coefficient") for spontaneous decay from level j to i. The rate coefficient A_{ij} can be expressed using the oscillator strength f_{ij} [Hutchinson 1987]. The collisional de-excitation is found from (2.26) and $\langle\sigma_{ji}v\rangle = (g_i/g_j)\langle\sigma_{ij}v\rangle\exp(E_{ij}/k_BT_e)$. This allows us to derive the following inequality from (2.29) [Hutchinson 1987]:

$$n_e \geq 1.4 \times 10^{19} \left(k_B T_e\right)^{1/2} E_{ij}^3 \quad [\mathrm{m}^{-3}] \qquad (2.30).$$

The temperature, k_BT_e, and energy level difference, E_{ij}, should be inserted in eV. The critical electron density from (2.30) is shown in Figure 2.6 for a range of energies appropriate for this thesis. High lying levels will come into LTE with each other and the free electrons before coming into equilibrium with lower lying levels since the energy difference decreases with increasing principal number. At this stage one then

talks of *partial local thermodynamic equilibrium* (PLTE). For H-like ions the criteria for a level with principal quantum number p to be in PLTE, with higher lying levels and the free electrons, is [Griem 1997]:

$$n_e \geq 2\times10^{24}\,\frac{\zeta^6\left(k_B T_e\right)^{1/2}}{p^{17/2}}\ \ [\mathrm{m}^{-3}] \qquad (2.31),$$

where again $k_B T_e$ is in eV. The symbol ζ defines the atomic number of the ion (e.g. 6 for carbon). As an example, the critical electron density for level p=3 in Li-like Carbon, is 3.7×10^{19} cm^{-3} at 20 eV, which is shown in chapter 4.

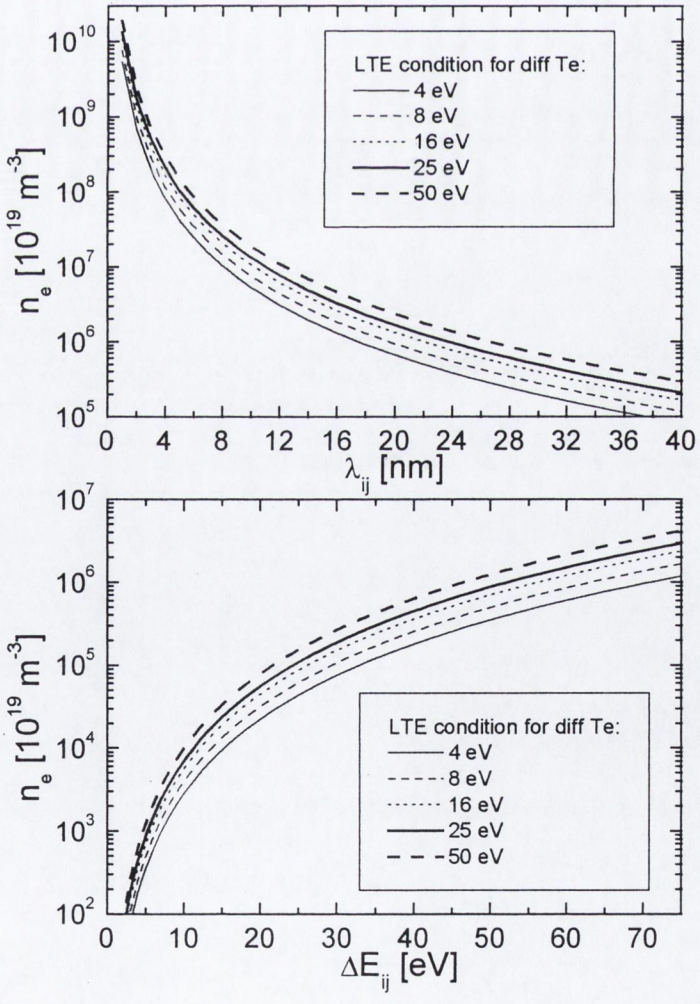

Figure 2.6: Critical electron density (2.30) for LTE *vs.* transition wavelength and energy separation.

Moving away from the LTE equilibrium the other equilibrium model often discussed in the literature is the *corona equilibrium model* or CE [McWhirter 1965]. Here the upward processes of collisional ionisation and excitation is balanced by the downward radiative recombination and spontaneous decay:

$$\begin{aligned} n_e n_i(m,g)\langle\sigma_i v\rangle &= n_e n_i(m+1,g)\langle\sigma_r v\rangle \\ n_e n_i(m,g)\langle\sigma_{gj} v\rangle &= n_i(m,j)\sum_{i<j} A_{ij} \end{aligned} \qquad (2.32).$$

In this formula $n_i(m,g)$ is the density of m-ions in the ground level. From this it is possible to calculate the fractional ionisation stages. Figure 2.7 below shows an example, from [Hutchinson 1987], of a calculation for Oxygen assuming an electron density of $n_e = 10^{21}$ cm^{-3}.

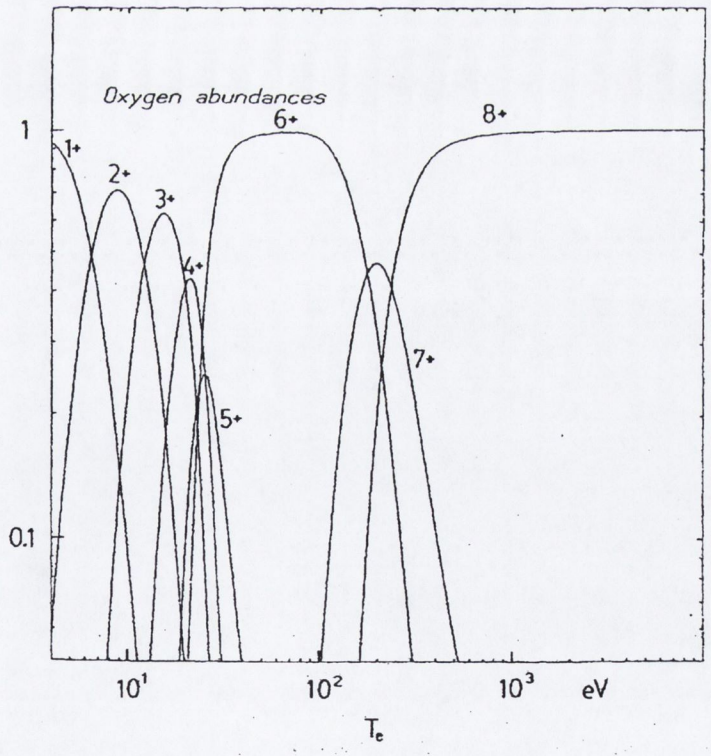

Figure 2.7: Relative charge stages of oxygen in coronal equilibrium [Hutchinson 1987].

Finally, we will mentioned the "enhanced" coronal equilibrium model termed *collisional-radiative equilibrium* model or CRE [McWhirter 1965]. The major difference from the CE-model, is that collisional free-bound transitions are included (3-body recombination) into any level. An example of the fractional ion charge stages using this calculation is given in Figure 2.8 for carbon.

Figure's 2.7 and 2.8 were adopted from the literature, but the same type of plots can be generated using the FLY code presented in the next section. In fact this is what was done to calculate the mean ion charge in Figure 2.5 for carbon. We recognise as well in Figure 2.8 the dominant presence of CV.

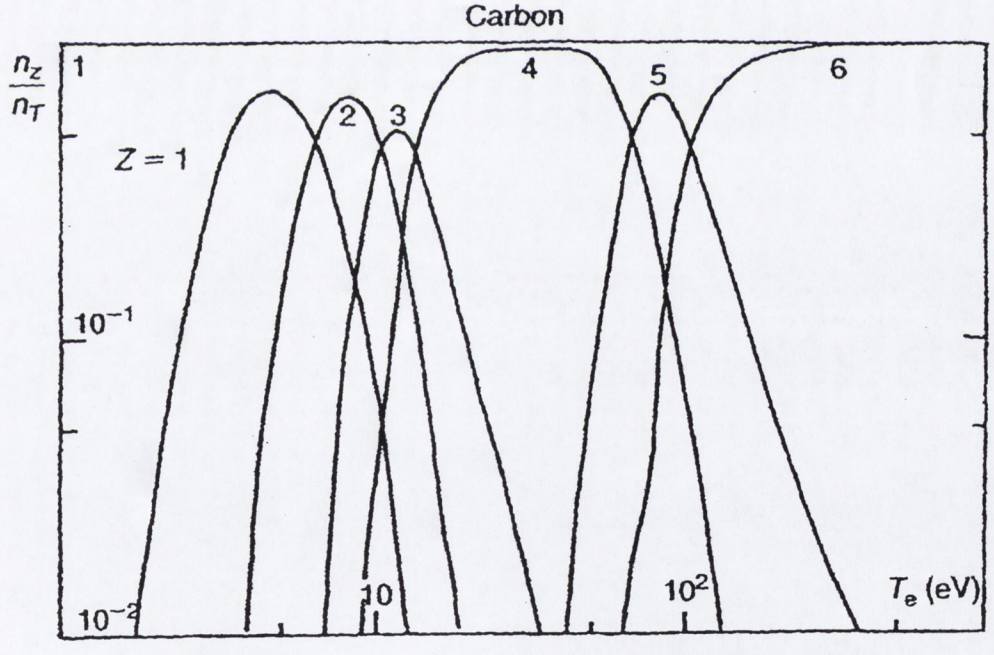

Figure 2.8: Relative charge stages of carbon [Turcu & Dance 1999].

In transient plasmas it is not just a question of reaching the right temperature and density to obtain equilibrium, the characteristic exchange time should also be short compared to the evolution of the plasma. If we just consider the collisions involving

free electrons the characteristic exchange times can be written [Goldston & Rutherford 1995]:

$$\tau_{ee} = \nu_{ee}^{-1} = \lambda_{ee} v_{th}^{-1} = \frac{12\pi^{3/2}\varepsilon_0^2}{2^{1/2} e^4 \ln\Lambda} \frac{m_e^{1/2}(k_B T_e)^{3/2}}{n_e} \quad [\text{s}] \qquad (2.33).$$

$$\tau_{ee} : \tau_{ei} : \tau_{ii} = 1 : \frac{2}{Z^2} : \frac{1}{Z^2}\left(\frac{m_{ion}}{m_e}\right)^{1/2} \frac{n_e}{n_i}\left(\frac{k_B T_i}{k_B T_e}\right)^{3/2}$$

Here τ_{ee}, τ_{ei} and τ_{ii} are the electron-electron, electron-ion and ion-ion collision times respectively. The factor, $\ln\Lambda$, is the Coulomb logarithm, that we will take to be $\ln\Lambda \sim 7$ [Phipps & Dreyfus 1993]. Figure 2.9 shows the scaling of τ_{ee} and τ_{ei} with the electron density for a few electron temperatures. Note, that the energy equilibration time between electrons and ions is $\tau_{eiE} \sim 2(m_{ion}/m_e)\tau_{ei}$

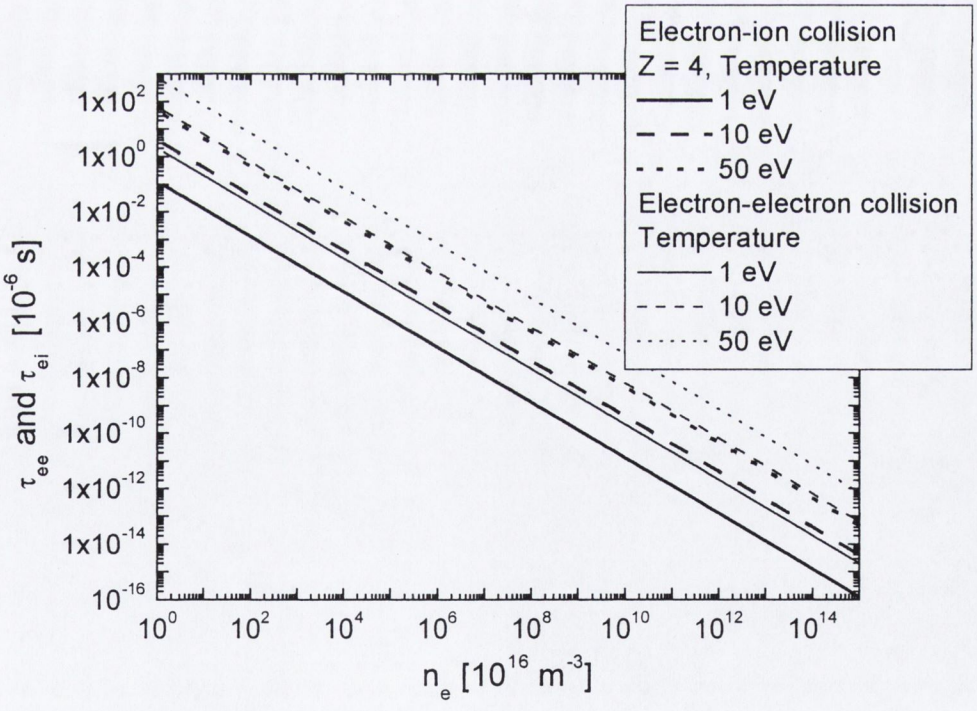

Figure 2.9: Collision times in a fully ionised plasma with Maxwellian electron distribution.

At a density of 10^{23} m^{-3} we find that the characteristic collision times are less than the typical times (10^{-9} s) in the plasma studied in this thesis.

2.2.3 FLY code

During the work undertaken in the FACADIX project the author has been introduced to the spectroscopy computer program called FLY [Lee 1995]. The FLY suite can generate detailed information on lithium-like, helium-like and hydrogen-like species for elements from helium to iron in the periodic system. It allows for both time-dependent and steady state calculations of the level populations to be undertaken. In the steady-state case the population distributions can be calculated assuming either LTE or steady state. The code is a collisional-radiative model.

The problem to be solved is represented by:

$$\frac{d\tilde{\mathbf{n}}}{dt} = \overline{\mathbf{R}} \bullet \tilde{\mathbf{n}} \tag{2.34}$$

Where the vector $\tilde{\mathbf{n}}$ contains the level populations and the matrix $\overline{\mathbf{R}}$ the rate coefficients R_{ij} from state i to j. The rate matrix contains the expressions for the bound-free transitions of: collisional ionisation and recombination, spontaneous radiative recombination and photo-ionisation as well as stimulated recombination. For bound-bound transitions it includes the Einstein coefficients for spontaneous emission, stimulated emission and photo excitation as well as electron collisional excitation (de-excitation) and auto-ionisation (inverse auto-ionisation).

We have already used the results generated from FLY in Figure 2.5 to predict the mean ion charge state. In chapter 4 the synthetic spectra generated from FLY is compared to experimental spectra obtained in a laser ablation experiment. Specifically the FLYSPEC part of the FLY-suite allows the calculation of line broadening in bound-bound transitions taking into account Doppler broadening as well as Stark broadening through detailed microfield simulation. Spectral line -

broadening is a large field of plasma physics that we will not treat in detail here, references can be found in [Griem 1997]. Suffice it to say, that Doppler broadening produces a Gaussian line shape (due to the motion of the emitting ions), with the full width half maximum given by:

$$\frac{\Delta\lambda}{\lambda} = 7.7\times10^{-5}\left(\frac{k_B T_i}{m_{ion}}\right)^{1/2} \qquad (2.35).$$

Here $k_B T_i$ is in eV and m_{ion} is in atomic mass units. The right hand side is typically less than $\sim10^{-3}$ for the plasma treated in this thesis. Stark broadening is produced due to the electric micro-fields that the emitting ion is submerged in. There is a quasistatic contribution from the ions and a collisional contribution from the fast moving electrons. The resultant line profile becomes that of a Lorentzian profile. The Debye length gives the characteristic length over which an electric field is felt in a plasma:

$$\lambda_D = \left(\frac{\varepsilon_0 k_B T_e}{e^2 n_e}\right)^{1/2} \qquad (2.36).$$

Here ε_0 is the permittivity in vacuum. To calculate the Stark broadening all the fields from the ions in a sphere of radius λ_D around the emitting ion should be included.

References

[chap 2] Anders A. (1997). "*Ion charge state distribution of vacuum arc plasmas: The origin of species*". Phys. Rev. E **55**(1), pp 969.

[chap 2] Anisimov S.I. Bäuerle D. and Luk'yanchuk B.S. (1993) "*Gas dynamics and film profiles in pulsed-laser deposition of materials*". Phys. Rev. B **48**(16) pp 12076.

[chap 2] Anisimov S.I. Luk'yanchuk B.S. and Luches A. (1996) "*An analytical model for three-dimensional laser plume expansion into vacuum in hydrodynamic regime*". Appl. Surf. Sci. **96-98** pp 24.

[chap 2] Chetry N. and Mond M. (2001). *Private communications.*

[chap 2] Dyson F.J. (1968) "*Dynamics of a Spinning Gas Cloud*". J. Math. Mech. **18**(1) pp 91.

[chap 2] Gaffet B. (1996) "*Expanding gas clouds of ellipsoidal shape: new exact solution*". J. Fluid. Mech. **325** pp 113.

[chap 2] Goldston R.J. and Rutherford P.M. (1995) "*Introduction to plasma physics*". (IoP Publishing, London).

[chap 2] Griem H.R. (1997). "*Principles of Plasma Spectroscopy*". (Cambridge University Press)

[chap 2] Hansen T.N. Toftmann B. Schou J. and Lunney J.G. (1999b) "*Lanmuir probe study of plasma expansion in pulsed laser ablation*". Appl. Phys. A **69**(Suppl.) pp S601.

[chap 2] Hutchinson I.H. (1987). "*Principles of plasma diagnostics*". (Cambridge University Press).

[chap 2] Kelly R. and Miotello A. (1994). "*Mechanisms of pulsed laser sputtering*". In "*Pulsed laser deposition of thin films*", Eds D.B. Chrisey and G.K. Hubler. (John Wiley & sons).

[chap 2] Lee R.W. (1995). "*The How To for FLY*". (Manual for the FLY program). Fly code commercial available from Cascade Applied Sciences, Inc. P.O. Box 4477 Boulder, CO 80306. See also, Lee R.W., Whitten B.L. and Strout R.E. (1984). "*Spectra-a model for K-shell spectroscopy*", JQRST **32**(1) pp 91.

[chap 2] McWhirter R.W.P. (1965). "*Spectral Intensities*". In "*Plasma diagnostics techniques*". Eds. R.H. Huddlestone and S.L. Leonard. (Academic Press, London).

[chap 2] Phipps C.R. and Dreyfus R.W. (1993) "*The high laser irradiance regime*". In "*Laser Ionization Mass Analysis*". Eds. A. Vertes, R. Gijbels and F. Adams. Chemical Analysis Series vol **124**, pp 369. (John Wiley & Sons).

[chap 2] Torcu I.C.E. and Dance J.B. (1999) "*X-ray from laser plasmas: generation and applications*". John Wiley & Sons, England.

[chap 2] Zel'dovich Y.B. and Raizer Y.P. (1966) "*Physics of Shock Waves and High-Temperature Hydrodynamic Phenomena*". Vol I. Eds W.D. Hayes and R.F. Probstein. Academic Press, New York and London.

CHAPTER 3

Micro capillary discharge experiment

3.1: Micro capillary discharge setup

3.1.1 Overview

The work reported here forms part of the contribution to the EU training and mobility network FACADIX that Trinity undertook as a partner. Most of the experimental results presented here were obtained in collaboration with the partners at Laboratoire de Physique et Technologie des Plasmas (LPTP) in Ecole Polytechnique, Palaiseau, France.

The micro capillary plasma discharge is a pulsed source of both energetic ions (velocities $>10^5$ m/s) and incoherent EUV-radiation ("extreme ultra-violet" wave-length in the range ~10 – 40 nm). These types of emissions will be discussed in this chapter and the following. The hot plasma is formed in a dielectric capillary that has been shrunk to dimensions of roughly 50 – 100 μm in diameter and 80 μm in length. The plasma is created by an electrical discharge of about 10 kV breaking down through a pre-formed hole (the capillary) in the dielectric separating two electrodes. This provides a localized region of high energy density plasma ($\sim 0.25\times10^6$ J cm^{-3}) comparable to that achievable by much larger pulsed power systems used in Z-pinch experiments [Ryutov *et al.* 2000] despite using only ~0.1 J of stored energy on the local capacitor. At the same time, since the discharge is formed directly in the energy storing dielectric, the circuit inductance is of the order

of a few times 10^{-10} H, whereby peak currents of more than 10 kA with a rate of change of 10^{13} A s^{-1} are achieved. Hence the microcapillary setup can be an interesting "test bench / student exercise" for some of the pulsed power generated plasma physics that is otherwise out of reach for most laboratories.

At the same time the micro capillary can be thought of as an academic case of a capillary discharge where the inductance has been shortened to the minimum (due to the short dimensions). The capillary discharge source is the subject of other partners in the FACADIX network. Typical dimensions of these types of ceramic capillaries are a few cm in length with an inner diameter of about a mm. In operation a gas, such as Ar at a pressure of ~60 Pa, can be made to flow through the capillary between the electrodes. The gas column is excited with current pulses reaching about ~30 kA peak amplitude. Under favourable conditions lasing has been observed in an Ar gas at 46.9 nm as explained by [Rocca 1999] and references therein. Alternatively, if no gas is injected, material from wall ablation can produce the plasma column in the capillary. This is the basis of the experiment, highlighted in chapter 1, and carried out by Dr. Samir Ellwi and co-workers in Prof. H-J. Kunze's laboratory. Here lasing at 18.2 nm in ionised carbon was demonstrated.

Finally we can mention, that not only coherent radiation sources are being pursued. There is a rapidly increasing interest in light sources of shorter and shorter wavelength for use in various applications, e.g. next generation lithography in the semiconductor industry [Attwood 1999] and [ITRS 1999]. Figure 3.1 is an example of the technology nodes for the lithography exposure technique identified by ITRS and their possible solutions; EUV is one of the candidates for the future. Of course any radiation source, which is planned for this type of application, faces additional

requirements such as high repetition rate and long life time; non of which the micro capillary source investigated in this thesis has.

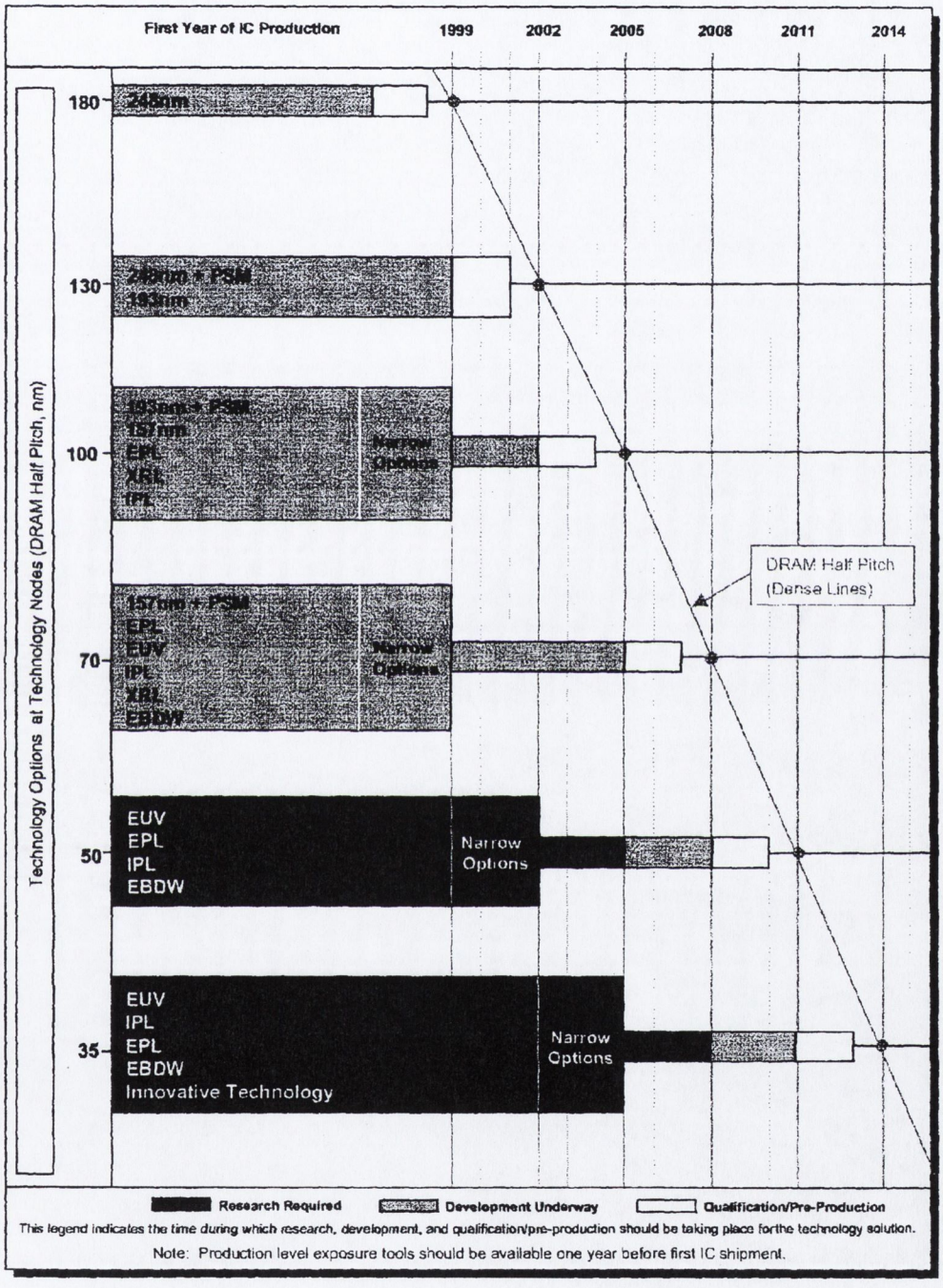

Figure 3.1: Lithography exposure tool potential solution [ITRS 1999].

3.1.2 The discharge cell

A sketch of the discharge cell is shown in Figure 3.2. The microcapillary is at the axis of symmetry of a pair of circular electrodes. The capillary is a hole of initial diameter $\phi_c \sim 50$ μm in a dielectric sheet of thickness $a \sim 80$ μm separating two circular plane electrodes of diameter $\phi_e = 90$ mm. The two electrodes form the anode and cathode as well as making up a parallel plate capacitor. An optional Al back-plate was inserted in between the back-electrode and the dielectric sheet. This was done to protect the back electrode from the ablation that takes place at that surface during the discharge. After each experiment (which corresponds to roughly 20 shots) the Al insert was discarded. Always the "back" electrode is the hot electrode; being pulsed charged either positive or negative with respect to the grounded front electrode that is connected to the vacuum chamber where the diagnostics equipment is attached. Figure 3.3 shows the details of the parts making up a cell. The insert depicted in Figure 3.2 limits the free angular view from the microcapillary to an angle Atan(0.3) ~ 17° from the normal.

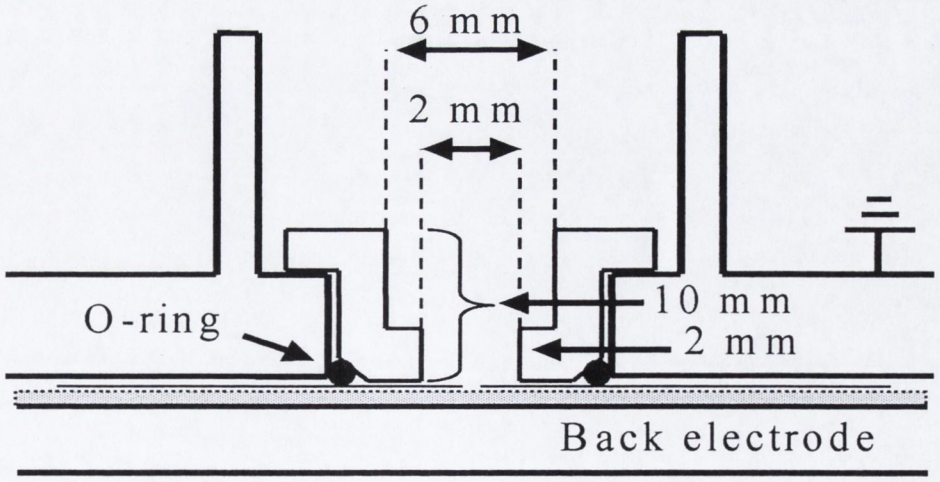

Figure 3.2: Enlarged view of a micro capillary discharge cell. The dielectric sheet with the micro capillary hole is shown as the thin full line on top of the grey thick line representing the Al-insert.

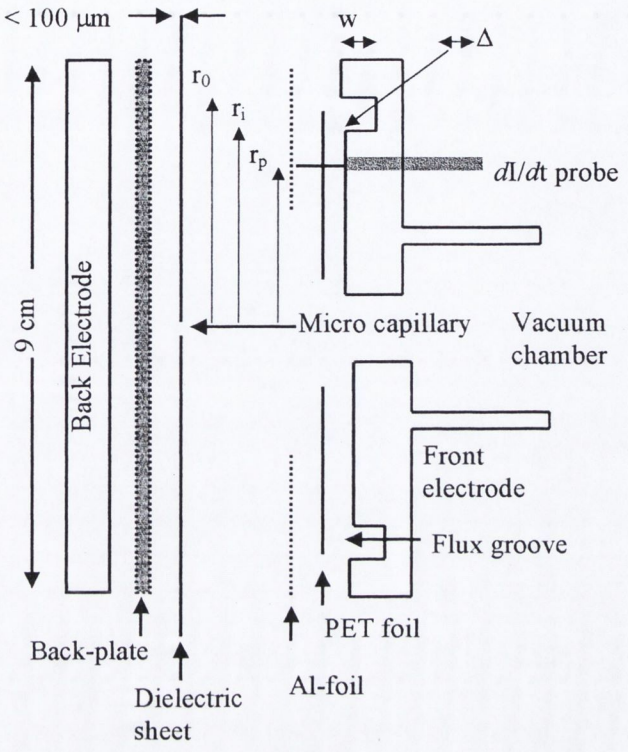

Figure 3.3: Exploded sketch of the micro capillary discharge cell. r_0 = 41 mm, r_i = 36 mm, r_p = 31 mm, w = 4 mm and Δ = 100 μm, the depth of a machined recess in the electrode corresponding to the thickness of the PET foil.

As for the dielectric sheet we worked with either Mylar or PVDF though most of the results given in this thesis were obtained with the Mylar sheet. Table 3.1 summarises some of the physical properties of these materials. The sheets have a thickness of 80 μm and 85 μm respectively for Mylar and PVDF. The micro capillary is formed by punching a hole in the dielectric sheet with a needle thereby creating a channel of roughly 50 μm in diameter as inspected with a magnifier.

	Density [g cm^{-3}]	Chemical formula	Dielectric constant ε_r @ 1 MHz	Dielectric strength [kV/mm]
Mylar (polyethylene terephthalate)	1.3 – 1.4	$C_{10}H_8O_4$	3.0	236*
PVDF (polyvinyldienefluoride)	1.76	$C_2H_2F_2$	8.4	63#

Table 3.1: Table of physical properties of the dielectric materials that have been used [Goodfellow-1999], *DuPont Teijiin Films, #Atofina Chemicals Inc.

In early tests, laser drilling was used but hand punching was preferred because it is simple, cheap and provides reproducible shapes. The higher dielectric constant of the PVDF sheet allows for a larger stored energy content on the discharge cell capacitance without changing dimensions, so keeping the inductance constant.

We can write the capacitance of the discharge cell as

$$C = \frac{\varepsilon_r \varepsilon_0}{a} A \tag{3.1}.$$

Here A is the area of the circular electrodes ($= \pi \times r_e^2$, with $r_e = \phi_e/2 = 45$ mm) and a is the electrode separation that can be taken as the thickness of the dielectric sheet as a first approximation. The capacitance is uniformly distributed between the two electrodes and, when it discharges through the capillary channel with a current I, the magnetic energy is:

$$E_M = LI^2 / 2 \tag{3.2}$$

L is the inductance. The energy can also be written as the integral of the magnetic energy density $B^2/2\mu_0$. With the help of the Biot-Savart law we derive the equation:

$$E_M = \int \frac{B^2}{2\mu_0} dV = \frac{a}{2\mu_0} \int_{r_c}^{r_e} \left(\frac{\mu_0 I}{2\pi r} \right)^2 2\pi r dr = \frac{a\mu_0 I^2}{4\pi} \ln \frac{r_e}{r_c} \tag{3.3}.$$

The self-inductance is then given by combining (3.2) and (3.3) to the equation:

$$L = \frac{\mu_0 a}{2\pi} \ln \left(\frac{\phi_e}{\phi_c} \right) \tag{3.4}.$$

The diameters of the electrode and the capillary are ϕ_e and ϕ_c respectively. Figure 3.4 shows the expected variations of the capacitance and inductance of the discharge cell with the electrode separation a. Also shown is the variation of L with the capillary

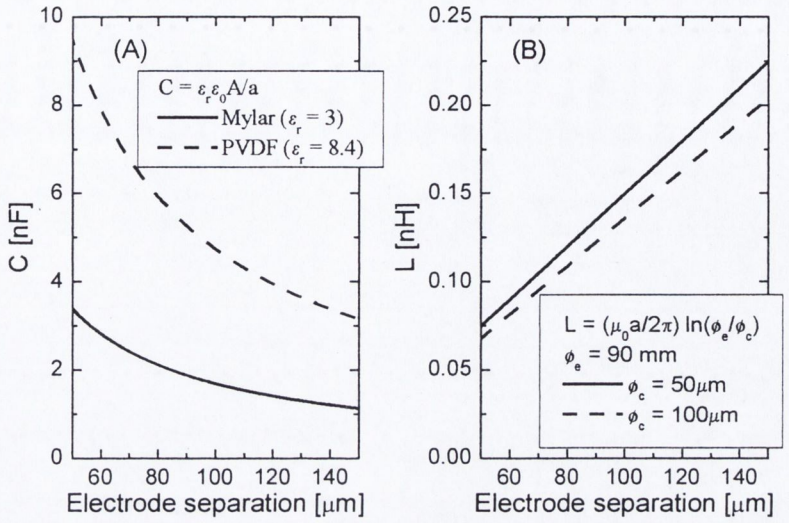

Figure 3.4: Graphs of (A): capacitance and (B): inductance of the discharge cell, as a function of electrode separation a.

diameter. Even a doubling of diameter is only going to change the inductance by a small fraction due to the logarithmic factor in equation (3.4).

3.1.3 Electrical schematics

The discharge cell of Figure 3.2 is pulsed charged by a transmission line of coaxial cables from a self-breaking spark gap in line with a primary capacitor bank. The primary capacitor bank of 6 nF is DC charged by a high voltage power supply to typically 15 - 20 kV. The pulsed charging scheme allows for a high hold-on-voltage of the discharge cell e.g. we will see that the discharge cell is routinely pulsed charged up to ~10 kV.

An equivalent electrical circuit diagram of the experimental setup, as used in the PSpice simulation package [MicroSim 1997], is shown in Figure 3.5. A discharge

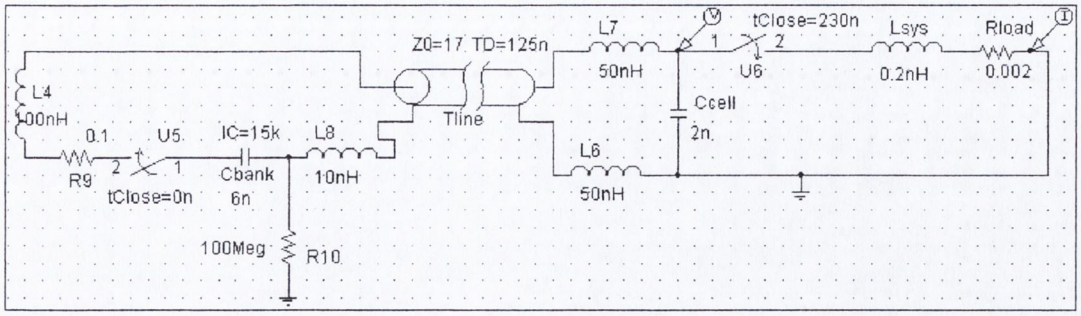

Figure 3.5: Equivalent electrical circuit diagram of the microcapillary discharge setup. C_{bank} is a capacitor bank of 6 nF charged to 15kV. The closing switch *U5* symbolises the sparkgap. T_{line} is the transmission line made of three parallel 50Ω coaxial cables of 25 m length. C_{cell} is the discharge cell and L_{sys} and R_{load} are the discharge inductance and load (plasma) resistance, respectively; the closing switch U6 represents the capillary breakdown at a time corresponding to first voltage maximum.

cell capacitance of C_{cell} = 2 nF was assumed along with an inductance of 0.2 nH and a (constant!) load resistance of 2 mΩ. The transmission line, T_{line}, corresponds to that used in most experiments of 3× 25 m coaxial cable (Z_0 = 50 Ω) in parallel. In the real experimental setup it was necessary to install relatively long delay cables (~ 125 ns) in order to have sufficient time for gating the diagnostics equipment on the chamber like e.g. the microchannel plate used for the spectral recordings.

Figure 3.6 shows the simulated voltage and current waveforms with the circuit of Figure 3.5. For a voltage pulse similar to that reported in chapter 3.2 below we see that the voltage rises in T/4 ~ 40 ns to a peak of 17 kV before the switch U6 closes and the current in the load starts flowing. The under-damped oscillations of the current pulse take place with a characteristic period of ~4 ns. The electrical components in Figure 3.5 were chosen so as to match the waveforms to that experimentally detected; these measurements are the subject of the next section.

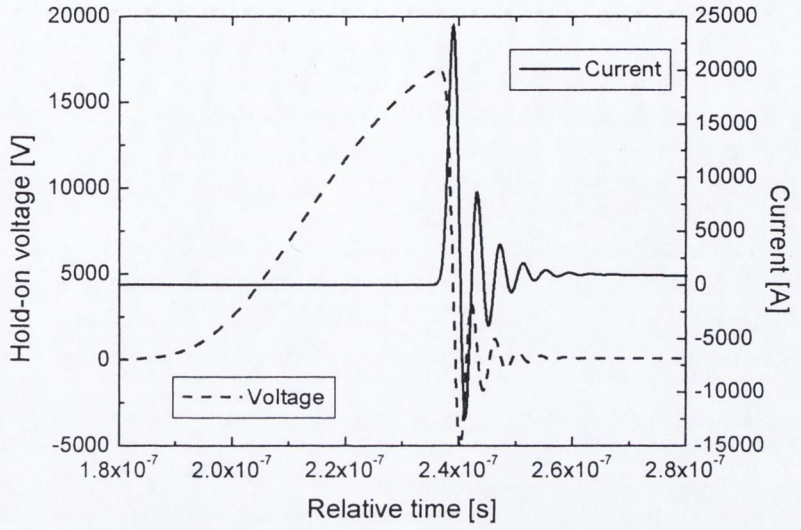

Figure 3.6: Voltage and current pulse in the Pspice model of Figure 3.5. Charging voltage 15kV.

3.2 Electrical measurements

Electrical measurements of the current and the hold-on-voltage are used to characterise the performance of the discharge. The sensing structures are placed close to the discharge cell but the signals are brought via screened coaxial cables to the oscilloscope placed in a Faraday cage, at a safe distance from any induced pick-up noise from the rapidly varying fields in the discharge. The oscilloscope has a bandwidth of 500 MHz and a sampling rate of up to 2 Gb/s.

3.2.1 Current recording

The groove in the grounded front electrode of the discharge cell (Figure 3.3) forms a single turn Rogowskii coil [Leonard 1965] for detection of the rapid change of current dI/dt in the discharge. The specific design of this type of inductive pick-up coil was described by [Ekdahl 1980] and used by [Choi and Favre 1998] on a hollow cathode capillary discharge device with a similar discharge cell. The machined -

groove in the grounded front-electrode, together with the Al-foil, form a loop for the return current that is completed by the signal lead of the sensor (the co-axial cable coming through the flange in Figure 3.3). Following Ekdahl, the voltage induced at the insulated pick-up point is:

$$V = -\left[\frac{\mu_0(w+\Delta)}{2\pi}\ln\frac{r_0}{r_i} + \frac{\mu_0\Delta}{2\pi}\ln\frac{r_i}{r_p}\right]\frac{dI}{dt}. \qquad (3.5).$$

Since the gap $\Delta \sim 100$ μm while $w = 4$ mm the second term in the above equation can be disregarded. With $r_0 = 41$ mm and $r_i = 36$ mm we find $V \sim -10^{-10} \times dI/dt$ – note that for a current rate of change of 10^{13} A/s the induced voltage amplitude is 1 kV.

We observe that there is a source of systematic error in this type of sensor due to the diffusion of the magnetic field into the walls on a spatial dimension around the skin depth δ. The error is given in [DiCapua 1986] as:

$$\Delta\% = \frac{4\sqrt{2}}{\pi}\frac{\delta}{w}, \quad \delta = \sqrt{\frac{2\eta}{\mu\omega}} \qquad (3.6).$$

Here ω is a characteristic frequency and η is the resistivity of the flange material. However for the fast pulses in this experiment e.g. $\omega = 2\pi/(4\text{ ns})$ (see Figure 3.9) and using the resistivity of brass $\eta = 3.9\times10^{-8}$ Ω m the error from this effect is minimal < 1%.

For the dI/dt-sensor a subsequent analogue integration is performed at the oscilloscope using a RC-circuit as depicted in Figure 3.7(A). Only signals with frequencies larger than f_1 are integrated, see Figure 3.7(B). The capacitor is a ceramic lead-through type capacitor (Tusonix 2499 Series) with a tolerance of 20%.

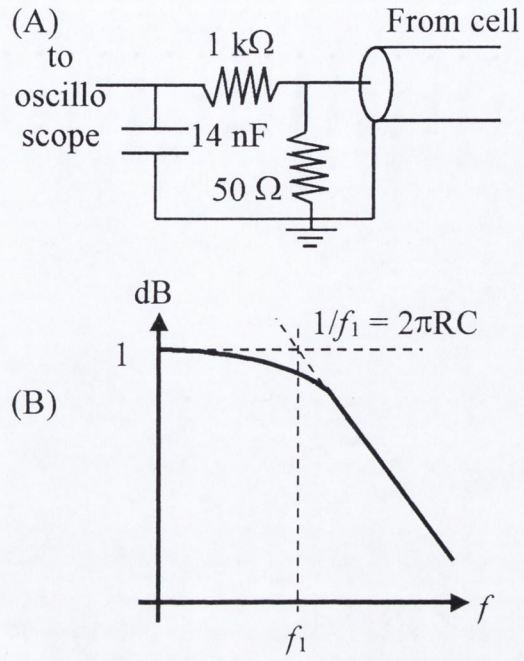

Figure 3.7: (A) Analogue integrator used at the scope to integrate the dI/dt signal from the cell. The 50Ω load resistance is made from 3×150Ω in parallel. (B) Frequency response of an integrating circuit. The circuit is integrating when $f > f_1$. For R = 1 kΩ and C = 14 nF we have $f_1 \sim 11$ kHz.

Using (3.5), the voltage recorded by the oscilloscope is related to the current in the discharge cell by:

$$V_s(t) = \frac{1}{RC}\int V dt \sim \frac{10^{-10}}{RC}\int (dI/dt)dt \sim (7.4 \pm 3.0)\times 10^{-6} I(t) \qquad (3.7).$$

Here we took R = 1 kΩ and C = 14 nF. An error in the values of R and C of ±20% is included as well. The overall response in the current measurement is then ~ (135 ± 55) kA/V where the signal on the oscilloscope is in volts.

3.2.2 Voltage recording

The hold-on voltage is measured at the back electrode of the discharge cell using a high voltage resistive divider [Pfeiffer 1986]. A diagram of the resistive divider can be found in Figure 3.8. The resistance R_1 is made from a shielded Silicone cable; the

type used as spark cable in a car. The division ratio V/V' is found from the following formulae:

$$\begin{aligned} V &= R_1 I_1 + R_2 I_2 && \text{(a)} \\ V' &= R_2 I_2 + R_3 I_3 = -R_c I_3 && \text{(b)} \\ I_2 &= I_1 + I_3 && \text{(c)} \end{aligned} \qquad (3.8).$$

By inserting (c) in (a) we obtain $V = (R_1 + R_2)I_1 + R_2 I_3$ and by inserting (c) in (b) we have that $I_1 = -(R_2 + R_3 + R_c)I_3 / R_2$. Combining the last two expressions and using again (b) to isolate $I_3 = -V'/R_3$ it follows that:

$$V = \left\{ (R_3 + R_c)\frac{R_1}{R_2} + R_1 + R_3 + R_c \right\} \frac{V'}{R_c} \qquad (3.9).$$

For $R_1 = 2.4\ \text{k}\Omega$, $R_2 = 10\ \Omega$, $R_3 = 40\ \Omega$ and $R_c = 50\ \Omega$ we obtain the ratio $V/V' = 482 \pm 95$ including an assumed uncertainty on all the resistances of 20%.

It should be noted that residual capacitances in the resistors could change the response of the resistance divider at high frequencies [DiCapua 1986b].

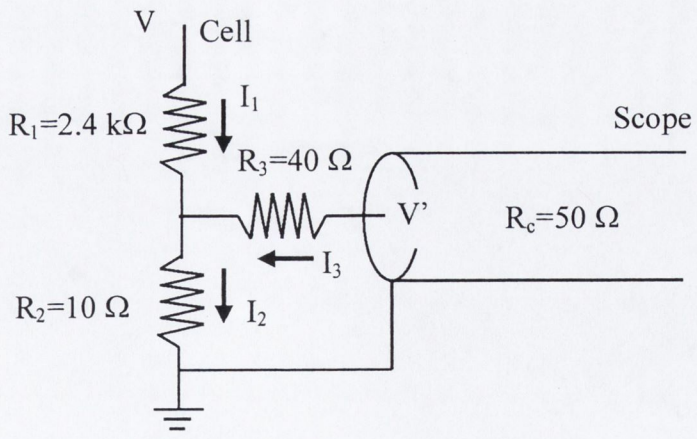

Figure 3.8: Resistance divider used in the micro capillary experiment. From (3.9) $V/V' = (482 \pm 95)$.

3.2.3 Electrical characterisation

As explained in the beginning of chapter 3.2 the oscilloscope was placed at a long distance from the discharge cell (and for experiments at LPTP in a Faraday cage). The transit times of the individual transmission lines running to the experimental setup was measured by applying a short pulse (of the same time scale as the signals recorded) to one end of the cable and recording the reflected signal. From this it is estimated that the relative time difference between different channels is determined to within an error of 2 ns.

Typical recorded signals of the hold-on voltage and current are shown in Figure 3.9. The voltage rises to its maximum value in ~50 ns and breaks down in less than 5 ns. In the following description, the time of the peak voltage V_p will always be taken as time zero. The energy stored in the capacitance of the cell at the time of breakdown is calculated to be ~0.1 J, while the capacitor bank (6 nF) is initially charged to ~15-20 kV corresponding to 0.7-1.2 J. The corresponding current signal is seen to reach a peak current of (60 ± 24) kA with a rise time of $\tau_{rise} = 1$ ns hence with a $dI/dt > 10^{13}$ A/s. The initial smaller negative dip in the current is evidence of an electron beam being present in the discharge. This structure in the current waveform is seen when the back-electrode is charged positive; in which case an effective hollow cathode is formed within the cell [Choi *et al.* 1999]. It should be noted that the measured rise time is close to the limit of what the oscilloscope is specified for. According to the manual of the oscilloscope the fastest rise time is given by $Rise\_time = 0.35 / Bandwidth$ which for a bandwidth of 500 MHz corresponds to a rise time of 700 ps.

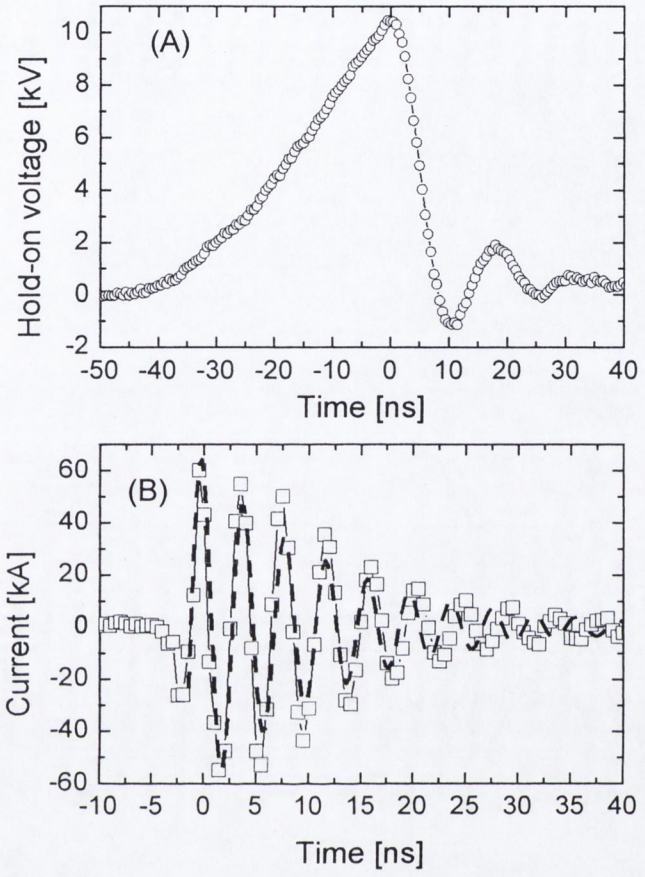

Figure 3.9: Shot no 8 with a cell of Mylar dielectric a = 80 μm. (A) Hold-on voltage. (B) Discharge current. A fit with Equation (3.15) for the under-damped current in a simple RLC circuit assuming V_p = 10.5 kV is shown as well for the current: *broken line*. From the fit we deduce the parameters $R = (0.015 \pm 0.002)\ \Omega$, $L = (1 \pm 0.1)10^{-10}$ H and $C = (4.2 \pm 0.4)10^{-9}$ F

The capacitance of the cell is measured with a multi-meter for comparison. Typically the value is less than that given by Figure 3.4(A) for a given dielectric thickness. The difference is attributed to the uncertainty in the thickness a for the capacitance. We can estimate the energy released in the discharge as $0.5 \times CU^2$ - equal to 0.07 J in the above case. The total stored charge ($Q = CU$) is of the order of $1.2 \times 10.5 \times 10^{-6} \sim 13$ μC. If we integrate the current over the first quarter period we obtain ~25 μC – in qualitative agreement.

We note the approximation, that for an oscillating discharge, the max current can be written [Früngel 1965]:

$$I_p = \sqrt{\frac{CU^2}{L}} \qquad (3.10).$$

For a self-inductance of $L = 10^{-10}$ H, a voltage U=10.5 kV and a capacitance C = 1.2 nF we get an I_{peak} = 36 kA. Given the errors in the current and voltage measurements this is in reasonable agreement with the recordings. Due to the statistical process of the breakdown process, and because of the ablation that takes place on the capillary walls and the back-plate, there is a shot to shot variation of the discharge characteristics even under otherwise identical conditions which makes reproducible investigations difficult. In Figure 3.10 we show the relationship between the current and the hold-on voltage for different shots.

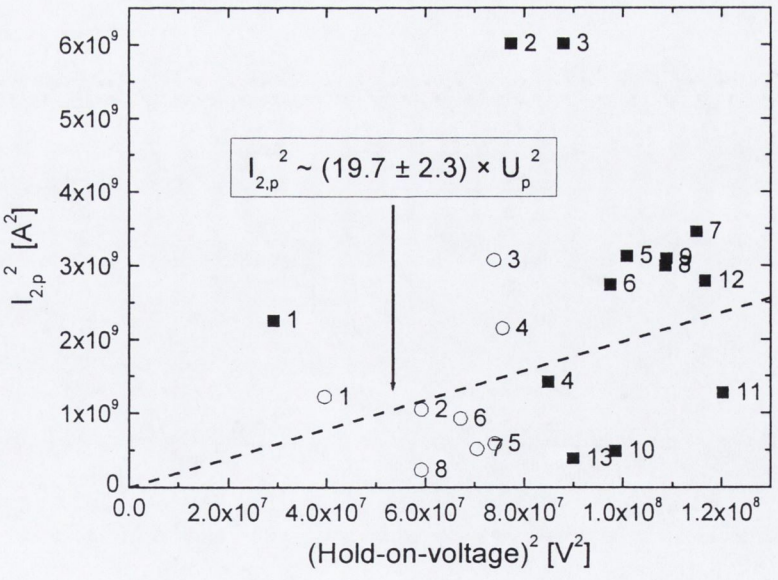

Figure 3.10: The squared current of the second peak *vs* hold-on-voltage squared for two different cells with a Mylar dielectric sheet and positive charging. The number next to each point indicates the shot number with that cell. The broken line is a linear fit through zero to the points with shot numbers larger than 3, with the error as that given by the fit procedure.

Since the first peak in the current is not always as well developed as in the example in Figure 3.9, we have used the second peak, $I_{2,p}$, in the first period as a marker. Figure 3.10 points to the limitation of Eq. (3.10). For a given voltage, the highest current peaks are usually produced in the first ~ 3 – 5 shots with a new cell. This can be explained by the fact that during the first ~5 shots the capillary diameter typically increases from ~50 μm to about 125 μm. This gives rise to a lower current flowing in the discharge, due to a change in plasma resistance as outlined below. Results presented in this chapter are obtained for shot numbers larger than 3 unless otherwise stated.

Theoretically the voltage and current in the discharge are related through the relation [Leonard 1965]

$$\begin{aligned} V &= \frac{d}{dt}(LI) + IR \\ &= L\frac{dI}{dt} + I\left(\frac{dL}{dt} + R\right) \end{aligned} \qquad (3.11).$$

To further investigate the constraints on the use of Equation (3.11) we will estimate the importance of the terms dL/dt and R in the parenthesis. The resistance per unit length of the plasma, R_l, can be written as $R_l = \eta/S$, where η is the plasma resistivity and S is the cross section of the plasma where the current flows [Choi 1983]. In a cylindrically shaped plasma column where the current is assumed to be confined to a shell of thickness of the skin depth we get that $S = \pi\delta^2(2r/\delta - 1)$, where r is the radius of the column and δ is the skin depth, see Equation (3.6). This allows us to write

$$R_l = \frac{\mu_0\omega}{2\pi\left(\frac{2r}{\delta} - 1\right)} \ \Omega\,\mathrm{m}^{-1} \qquad (3.12).$$

This analysis is **only true if** $\delta < r$ and as we will see this is in general not true during the evolution. The plasma resistivity is often adopted from that given by Spitzer for a fully ionised plasma [Spitzer 1962]:

$$\eta = 1.03 \times 10^{-4} \frac{Z \ln\Lambda}{T_e^{3/2}} \quad \Omega\,\mathrm{m} \tag{3.13}$$

Z is the mean ion charge, T_e is the electron temperature in eV and $\ln\Lambda$ is the Coulomb logarithm which we will take as equal to 6. Figure (3.11) shows the variation of R_l and δ with the electron temperature assuming $Z = 4$. The contribution to the voltage drop from the change in the linear-inductance is estimated using the formula:

$$\frac{dL_l}{dt} = -\frac{\mu_0}{2\pi r_c}\frac{dr_c}{dt} \sim -\frac{\mu_0}{2\pi r_c} c_{s,0} \quad \Omega\,\mathrm{m}^{-1} \tag{3.14}$$

$c_{s,0}$ is the sound velocity that can be taken from the expression in chapter 2.2. For $\gamma = 1.26$, $Z = 4$ and $M = 12$ u the resistance due to the change in inductance is shown as well in Figure (3.11). The resistance diverges as the assumption of the skin depth being less than the radius is violated. The condition on the skin depth is fulfilled only for high temperatures. If the resistance is evaluated as the Spitzer resistivity divided by the area of the column $\sim \pi r_c^2$, the resistance per length is given as in Figure 3.12. At a plasma temperature of 20 eV we find that $R_l \sim 10000\ \Omega\mathrm{m}^{-1}$ corresponding to a resistance of 0.8 Ω, if the length is taken as the thickness of a Mylar foil =80 μm.

From the Figures 3.11-12 we can expect that the contribution from the resistive term in the parenthesis in (3.11) is larger than the dL/dt term for the temperature range of interest in the microcapillary experiment (10 – 50 eV). Note however that $R_l \sim r_c^{-2}$ while $dL/dt \sim r_c$ so the two terms can evolve into becoming comparable.

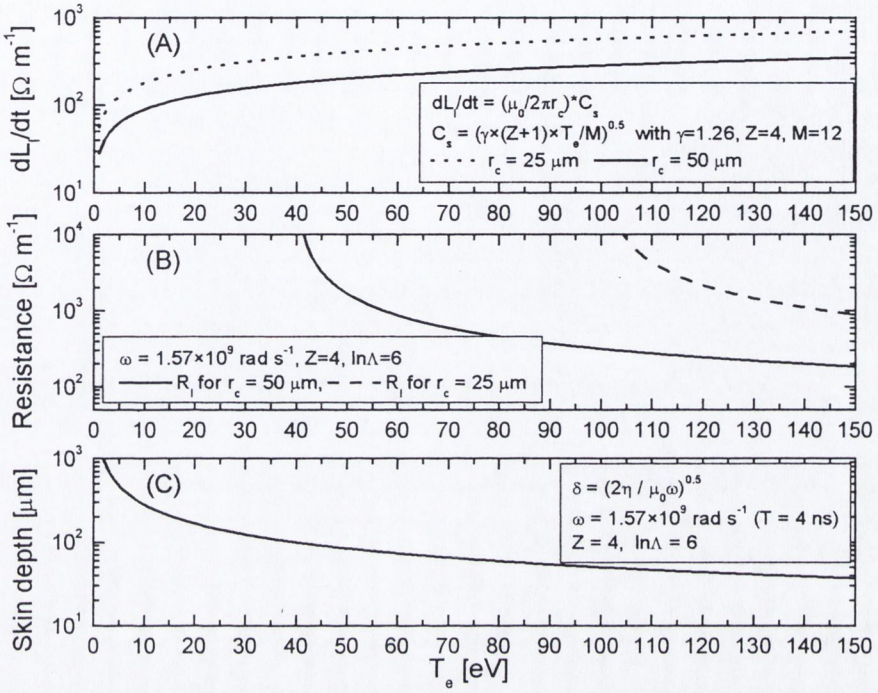

Figure 3.11: Contribution to the voltage drop as a function of temperature from (A): Change in inductance (3.14) and (B): Resistance (3.12) per unit length of the plasma column. (C) Shows the skin depth.

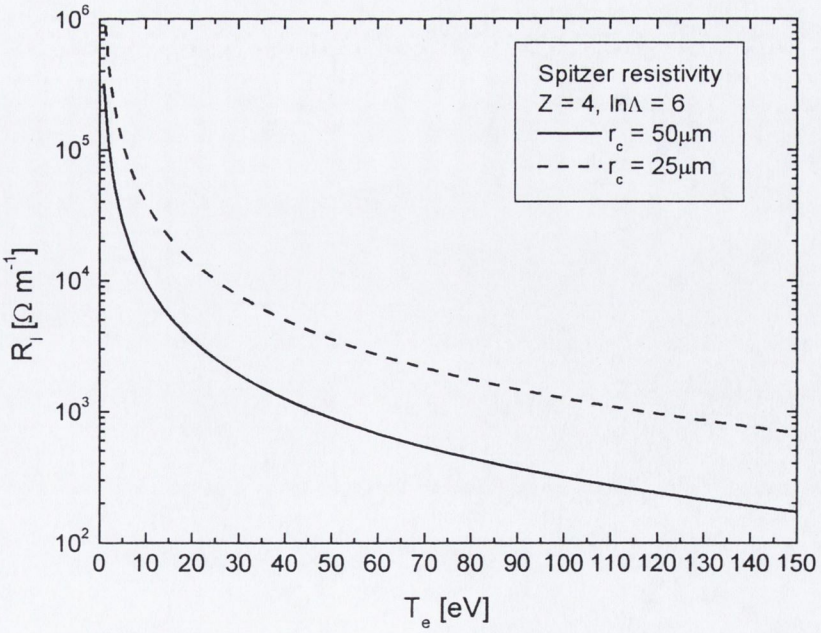

Figure 3.12: Resistance per unit length assuming the Spitzer resistivity η and $R_l = \eta/S$ where $S = \pi r_c^2$.

If we ignore the dL/dt term and the time dependence of the resistance the solution to (3.11) is that of a simple RCL circuit as presented in most undergraduate books on electromagnetism. The solution for the *under-damped* case (i.e. $R^2 < 4L/C$) is:

$$I = \frac{V_p}{\omega L} e^{-\frac{Rt}{2L}} \sin(\omega t) \ , \ \omega = \sqrt{\frac{1}{LC} - \frac{R^2}{4L^2}} \tag{3.15}$$

A *single fit* to the current in Figure 3.9(B) with this solution is seen to reproduce the waveform initially while at later times (>20 ns) the solution oscillates too fast indicating the changing parameters of the discharge. The errors on L, R and C given in the text to Figure 3.9(B) are those arising from the fitting procedure. If the current is varied within the limits of that determined by (3.7), the values of R, L and C may change by a factor of ~2 - 2.5.

In trying to take into account the time dependence of the resistance we proceed as in [Hong *et al.* 2000] who investigated a gas capillary discharge of length of a few centimetres and diameter of 1 mm. In this reference a piecewise fit to the current over a single oscillation of the waveform was performed using (3.15). In Figure 3.13 the resistance obtained from fitting the current waveform over 3/2 of a period is shown. The initial resistance is very uncertain (given by the fit) and not too much importance should be put on it. At later time the resistance increases as expected for a plasma undergoing cooling. Actually in an adiabatic expansion we have that $T_e \sim t^{-3(\gamma-1)}$ and from Spitzer's formula it follows that the resistance $R \sim T_e^{-3/2}$ hence $R \sim t^{9(\gamma-1)/2} \sim t^{9/8}$ if $\gamma = 1.25$ is assumed. This scaling is depicted in Figure 3.13 as well and shows a qualitative agreement with the measured evolution. Combining Figures 3.12 – 13 it is seen that a 100 μm long plasma cylinder with radius $r_c = 50$ μm having a resistance of ~0.1 Ω will have a temperature of 40 eV.

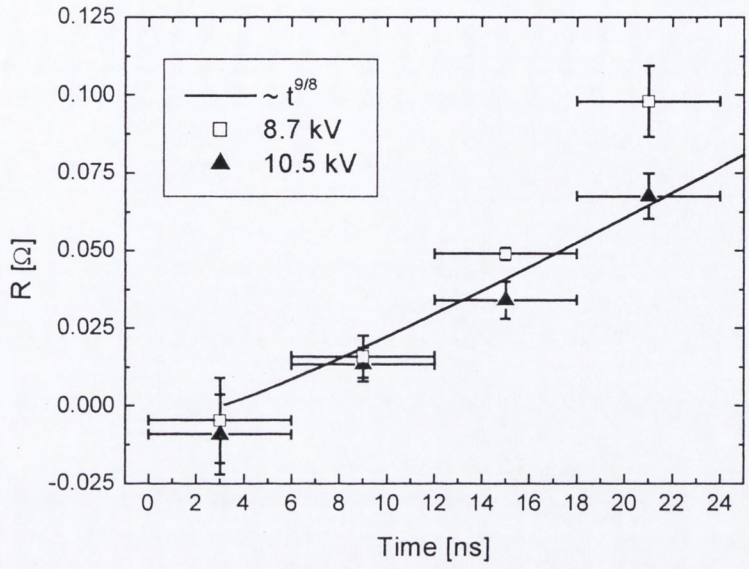

Figure 3.13: Mean resistance *vs.* time for two different charging voltages as obtained by piece wise fitting of (3.15) to the current waveform. Solid curve is $R \sim t^{9/8}$ as expected for $\gamma = 1.25$, see text.

3.2.4 Conclusion on electrical characteristics

The microcapillary is a fast discharge unit with a stored primary energy of less than 1 J. The fast pulses means that a current of at least 10 kA and with a current rate of change of more that 10^{13} A/s can be generated in the sub millimetre discharge.

The shot to shot variation is appreciable as seen from Figure 3.10. Also from this figure a plasma resistance of $(1/19.7)^{½} \sim 0.2\ \Omega$ can be deduced; using Figure 3.12 we calculate a temperature of ~25 eV assuming $r_c = 50\ \mu m$ and a length 80 μm.

The time evolution of the resistance and hence the temperature was measured from the current probe oscillation approximated using (3.15). The analysis relies on neglecting the *dL/dt* term in (3.11), which can only be partly verified. If the temperature is inferred from Figure 3.12 and 3.13 it is concluded that initially the plasma acquires a temperature of >50 eV for these experiments.

3.3: Ion outflow from the micro capillary as measured with electrostatic probes

The use of electrostatic probes in quiescent plasmas is an established technique to obtain localised information of plasma parameters. Reviews can be found in [Chen 1965] and [Chung *et al.* 1975]. In its simplest form an electrical probe consists of a small metallic electrode inserted into the plasma and connected to a power supply that allows it to be biased positively or negatively with respect to the plasma. The term *electrostatic probe* is often used interchangeable with the term *Langmuir probe* after Irving Langmuir who was the first to use this method for investigations of plasmas [Mott-Smith and Langmuir 1926].

3.3.1 The electrostatic probe

As commented on by [Chen 1965], though the experimental realisation of an electrostatic probe is very simple, the theory for describing the probe response is rather complicated and often not analytically solvable. The reason is that the probe is a boundary to the plasma and therefore when immersed in the plasma the probe becomes surrounded in what is termed the plasma sheath. In the sheath, the equation of motion changes from that of the bulk and quasi-neutrality ceases to be fulfilled complicating its description [Riemann 1991]. Investigations with probes in flowing plasmas include laser-generated plasmas but also geophysical experiments of charged particle measurements at high altitude using rockets or satellites, see references in [Chung *et al.* 1975].

The plasma generated in the microcapillary is not only fast flowing but is also transient and in that sense it resembles a laser produced plasma. Our group has previously used negatively biased probes for collecting positive charged ions from plasma plumes in laser ablation of metal targets in vacuum i.e. [Lunney et al. 1993], [Jordan and Lunney 1998] and [Hansen *et al.* 1998]. A generic electrical circuit of the type that is used in the experiments in this thesis is shown in Figure 3.14. The probe is connected to the circuit placed at the oscilloscope through a screened coaxial cable. As in the case with the current and hold-on-voltage measurements of the previous chapter the oscilloscope was placed away from the microcapillary to avoid electrical noise.

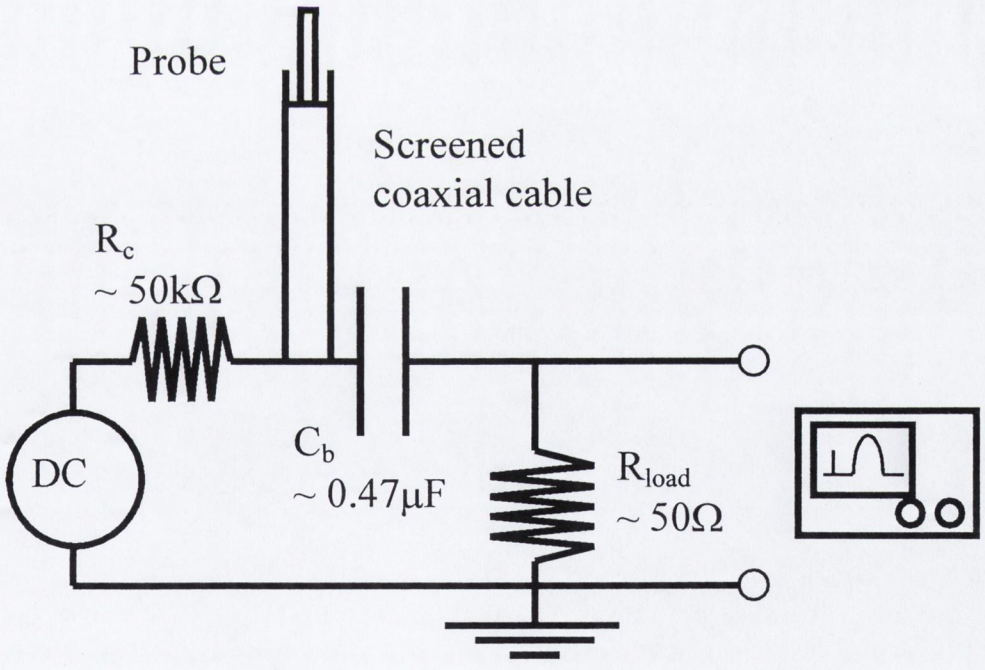

Figure 3.14: Electrical circuit for an electrostatic probe. R_c, R_{load} and C_b are the charging- the load resistor and the blocking capacitor respectively. The probe signal is sent to the circuit by a screened cable.

A few rules of thumb should be adhered to when choosing the component values for the circuit.

(A) The total collected integrated charge in a pulse must be much less than that stored on the blocking capacitor i.e. $Q = C_b V$, where V is the bias voltage.

(B) The signal voltage measured over the load resistor should be much less than the bias voltage applied to the probe at all times, hence $V_{peak} < V_B$.

(C) The full width at half maximum pulse length should be shorter than the characteristic time constant of the circuit, to avoid unwanted charging and discharging during the period of the pulse, hence FWHM $< 2\pi R_{load} C_b$.

A very short introduction to the theory of ion collection by Langmuir probes will be presented here. The discussion follows that of [Koopman 1971] and [Segall & Koopman 1973] who made detailed investigations of the use of electrostatic probes in flowing plasmas produced by laser ablation. If we assume that the velocities of the ions are equal in magnitude and parallel in direction, the ion current to a cylindrical probe biased negatively with respect to the plasma potential is:

$$I_i = (1+\varepsilon) A e \left(\sum n_k Z_k\right) u \times \left\{1 + \left[2e\left(V - V_p\right)/ m_i u^2\right]\right\}^{1/2} \qquad (3.16).$$

Here V the probe potential is of such a value with respect to the plasma potential V_p that the ions are attracted. The factor A is the collection area of the probe, m_i the mass of the ion, n_k the density of ions with charge Z_k and u is the flow velocity. To take into account the effect of emission of secondary electrons from the probe surface, the electron emission coefficient ε is introduced. An electron leaving the probe surface will be accelerated away and, because of charge balance, this will appear as if a positive ion had hit the probe. Eq. (3.16) is deduced under the assumption that:

$$u >> \sqrt{\frac{2k_B T_i}{m_i}} \qquad (3.17),$$

k_B is Boltzmann constant and T_i is the ion temperature. This is equivalent to saying that the velocities are nearly parallel in direction as mentioned above. Further, if the range of probe potentials applied are limited so that $|e(V\text{-}V_p)| << ½m_i u^2$, the expression for (3.16) simplifies and we have instead:

$$I_i = (1+\varepsilon)Ae\left(\sum n_k Z_k\right)u \qquad (3.18).$$

If we rewrite (3.17), substituting $T_e \rightarrow T_i$, the inequality may be recognised as the expression for the Bohm criterion [Riemann 1991] on the stable sheath formation around a probe. The Bohm criterion is a necessary condition in the limit $\lambda_D/L \rightarrow 0$, where λ_D is the Debye-length and L a characteristic dimension of the plasma. When it is fulfilled a positive sheath that decays fast (~ on a scale of the Debye-length) into the plasma can form around the negatively biased probe and thereby screen the bulk plasma from the disturbance of the probe potential.

To show that these considerations apply to the experiment here, it is useful to evaluate some of the relevant plasma parameters. Even for a relative low density $n \sim 10^{10}$ cm^{-3} and high temperature $T_e \sim 10$ eV the Debye-length is small compared to the probe: $\lambda_{D,[m]} \sim 7.43(T_{e,[eV]}/n_{[cm\text{-}3]})^{½} \sim 235$ μm. Further the condition (3.17) is easily fulfilled in the plasmas discussed here. For a carbon ion with a velocity of 5×10^4 m s^{-1} the condition is $k_B T_i << 150$ eV. Since the initial electron temperature during the breakdown of the micro capillary discharge is not even so high, as inferred from independent measurements reported in the other chapters, it is safe to conclude that at the position of the probe (usually some cm away from the source) the

condition is easily met. Hence we note that the Bohm criterion is over-satisfied in the plasma outflow from the micro capillary and that we are in the limit $\lambda_D/L \rightarrow 0$. The conditions are then fulfilled for the probe to have only a local influence on the outflow, and (3.18) can be used to interpret the current with A the projected area of the probe normal to the flow. We remark as well that the condition on the probe potential: $|e(V-V_p)| << \frac{1}{2}m_i u^2$ used to deduce (3.18), will in general be weaker than that mentioned. This is because the original expression (3.16) was calculated for a beam of charges of one numerical sign (i.e. positive). In the plasma the influence of the probe potential will only be transmitted over a distance of the Debye-length and as seen in the calculation above this is very short. Formula (3.18) is therefore assumed throughout this thesis.

The conducting tip of the probe was usually made from copper or silvered copper. As we will see, the ions typically have kinetic energies above 1 keV. At these energies secondary electron emission from the probe can be expected. The study by Cano [Cano 1973] shows that for C^{2+} ions impinging on a gold target $\varepsilon \sim 2.5$ while for Al^{2+} it is ~1.5, the value scales roughly with the power $m_{ion}^{-0.4}$ of the incident ion mass. The emission coefficient is higher for higher charged ions e.g. around 8 for C^{5+}. It will be assumed that these values are not much different for a copper or silver surface. Not including the secondary electron emission contribution to the probe current in calculations will lead to an overestimation of the ion density.

3.3.2. Result and discussion of probe measurements

The probe was inserted downstream from the discharge cell in a vacuum chamber evacuated to a pressure $<10^{-3}$ mbar. Typically the chamber with the discharge cell (Figure 3.2) could only be evacuated to a minimum pressure of $\sim 10^{-4}$ mbar despite the use of a turbo-molecular pump. This relatively high background pressure is a consequence of the design of the discharge cell where we rely on pressing the two electrodes tight on to the dielectric to form the vacuum seal. In the experiments on the micro capillary the probe was held at a potential of –130 V to collect ions.

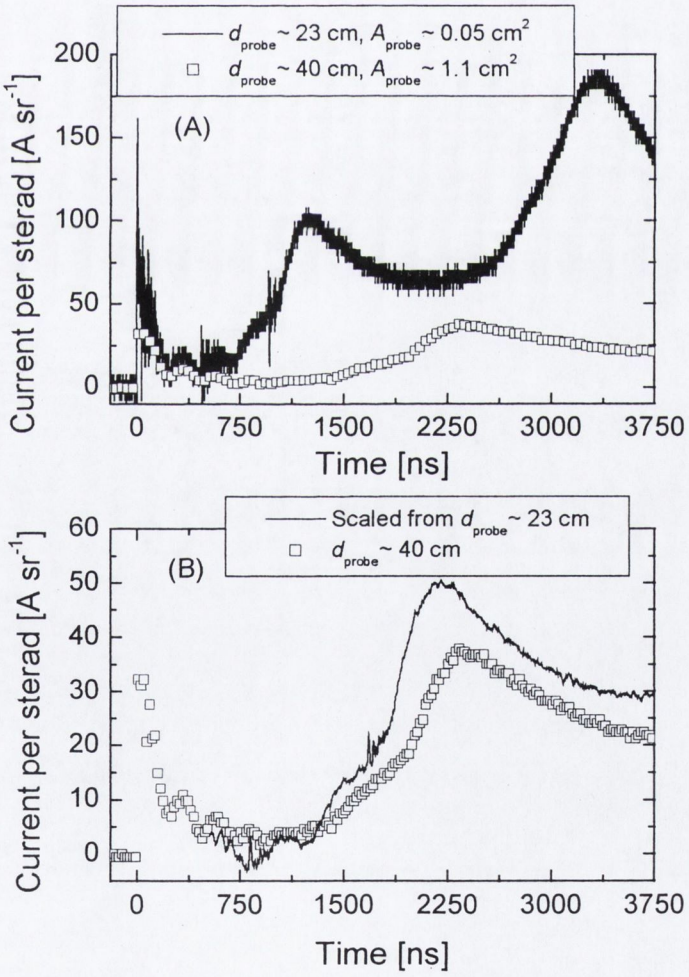

Figure 3.15: (A) Current per sr from a Mylar micro capillary discharge with $V_p \sim 8.5$ kV recorded by two electrostatic probes at different positions. (B) Same as in (A), but the current at the first probe has been scaled to the position of the second probe. The peak at time 0 is caused by photoelectric emission of electrons from the probe.

In Figure 3.15 we show examples of the recorded time-of-flight (TOF) current recorded by Langmuir probes in a double probe experiment in which two probes were inserted downstream of the discharge cell at different distances. We have seen in chapter 2 that after an initial acceleration the plume expansion becomes inertial and the expansion velocity into vacuum constant. In order to conserve particle number it is then necessary that $N \sim r^{-3}$ with N the density and r the expansion radius [Rumsby & Paul 1974]. It follows easily that the current per steradian at probe 2, $i_2(t_2) \equiv I_2(t_2)d_2^2/A_2$, should be related to that measured at the position of probe 1 by $i_2(t_2) = i_1(t_1)\times(d_1/d_2)$ with $t_2 = t_1\times(d_2/d_1)$. Here d_1 and d_2 are the distances of probes 1 and 2 ($d_2 > d_1$) respectively and $A_\#$ the probe area and $I_\#$ the current intercepted by that probe. Figure 3.15(B) illustrates this scaling applied to the current recorded by the first probe. The measured current amplitude at $d_2 = 40$ cm is about 30% less than the scaled current which suggests that scattering of particles takes place during the flight between the two probes. The expansion velocity of the peak flux in between the two probes is calculated to be ~17/930 cm/ns ~1.8×10^5 m/s. With this flow velocity, using Eq. (3.18), the peak-flux charge density at the first probe becomes $N \sim 10^{16}$ m^{-3} assuming an effective mean charge at this late time of $\overline{Z} = 2$ and $\varepsilon = 2.5$. The recorded expansion velocity is confirmed when we combine the results from several separate experiments with various probe distances as shown in Figure 3.16. The first flux peak expands at a constant velocity $v = 1.7\times10^5$ m/s up to the maximum distance of 88 cm. The scatter in the TOF of the second peak flux makes it difficult to make assumptions about its origin. In figure 3.16 we show a fitting curve of the data following the scaling $d = \text{const} \times t^{2/5}$.

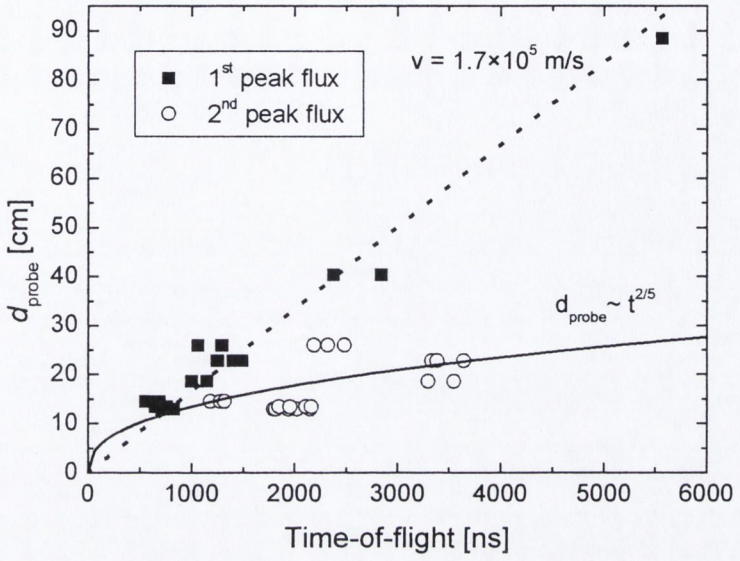

Figure 3.16: Probe distance *vs.* time of flight of peak flux for the 1st and 2nd peak. The hold-on-voltage is roughly constant ~9 kV on a Mylar dielectric discharge cell.

This expansion is what is expected from a hydrodynamic treatment of a strong explosion with counter pressure [Zel'dovich & Raizer 1966, pp 93]. This phenomenon has been much investigated in pulsed laser deposition of thin films where the laser produced plume expands through a background gas. It is in general assumed that the plume splitting occurs when the expansion distance becomes comparable to the collision mean free path for collisions between the plume and background gas. [Wood *et al.* 1997]. We have observed that effect using ion probes for the expansion of laser ablated silver ions into an oxygen background [Hansen *et al.* 1999]. As was mentioned at the beginning, the background pressure was typically $P = 10^{-4}$ - 10^{-3} mbar. With a collision cross-section of about $\sigma_c = 5\times10^{-15}$ cm^2 for collisions of ions with neutrals [NRL 2000] the mean-free-path is $\lambda_c \equiv 1/n_g\sigma_c = k_BT/P\sigma_c$ and we get that $\lambda_c = 80$ - 8 cm. Hence plume splitting due to scattering of part of the plume particles may be the cause of the second peak but

more detailed investigations, especially at large probe distances, will have to be done to clarify this.

From the discussion of the hydrodynamic expansion into vacuum in Chapter 2.1, we note that the *front velocity* depends on the energy content E and total mass M of the initial plume as ((2.15) and (2.19)):

$$v_{front} = \left(4\gamma/\gamma - 1\right)^{1/2} (E/M)^{1/2} \tag{3.19}.$$

In Figure 3.17 the front velocity is shown as a function of charging energy on the local capacitor. The highest hold-on-voltage, V_p, is achieved with a negative charging of the back plate and is roughly –14 kV. The plasma front velocity is seen to reach up to ~3×10^5 m/s which, if we assume a particle of the mass of a carbon ion, corresponds to a kinetic energy of 5.5 keV.

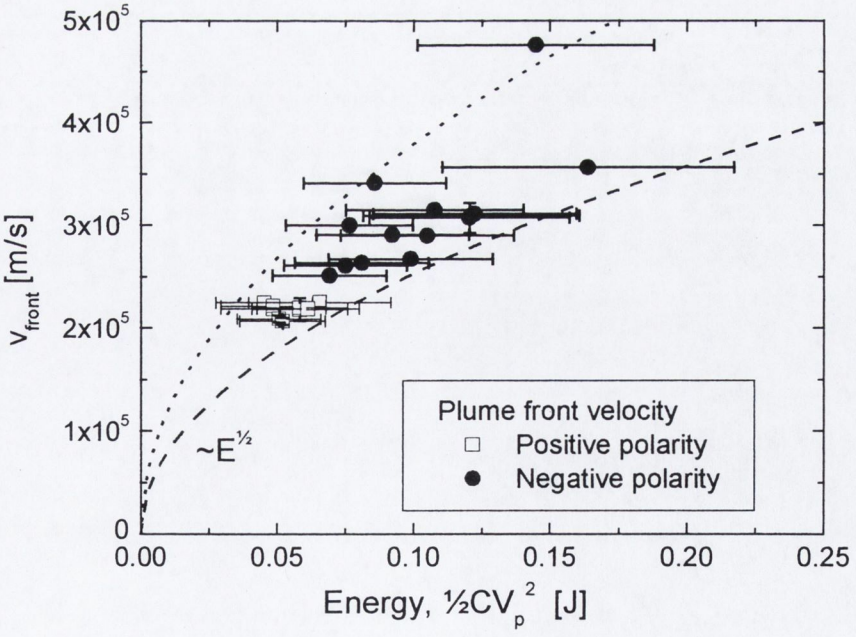

Figure 3.17: Expansion velocity *vs.* discharge energy for both positive and negative polarity on the back plate. A Mylar dielectric was used on the cell. The errors shown include the uncertainty on the measured hold-on-voltage. The broken lines show that the front velocity scales as ~$(8 - 12)\times10^5\times E^{1/2}$ corresponding to an initial mass M~20 ng.

This scaling is observed from the broken lines in Figure 3.17. It follows that the average initial mass of the plume per discharge for $\gamma = 1.26$ is given by $19.4/10^{12} \sim (2 \pm 0.8) \times 10^{-11}$ kg. This result is supported by an independent measurement of the eroded area per shot of the dielectric foil. If we measure the radius of the micro capillary in the dielectric before being inserted in the cell and after several shots with it, the ablated volume is determined as $dV = \pi \times \Delta \times (r_{end}^2 - r_{ini}^2)$ where Δ is the thickness of the dielectric. Figure 3.18 shows the deduced averaged mass ablated per shot. Also shown is the average number of atoms per shot calculated from the formula:

$$N = \alpha dV \frac{\rho}{M_m} 6.022 \times 10^{23} \qquad (3.20).$$

Here α is 22 for Mylar ($C_{10}H_8O_4$) and 6 for PVDF ($C_2H_2F_2$) and ρ is the density while M_m is the molar mass of 192 and 64 respectively (Table 3.1). The uncertainty in the measurement of the radius is rather large but it is concluded that the value of the initial mass is around 50 – 100 ng per shot in reasonable agreement with that deduced from Figure 3.17.

Continuing the hydrodynamic description of the expansion, we proceed to apply the theory for expansion of a plume into vacuum by Anisimov presented in Chapter 2.1. It is noted that this model strictly speaking holds only for the expansion of a plume from a plane surface. We remember that the model does not include any information about how the plume was initially formed, only a description of how it expands. In order to justify the use of a hydrodynamic interpretation of the expansion we will first evaluate the collision mean free path of the ions in the initial plume.

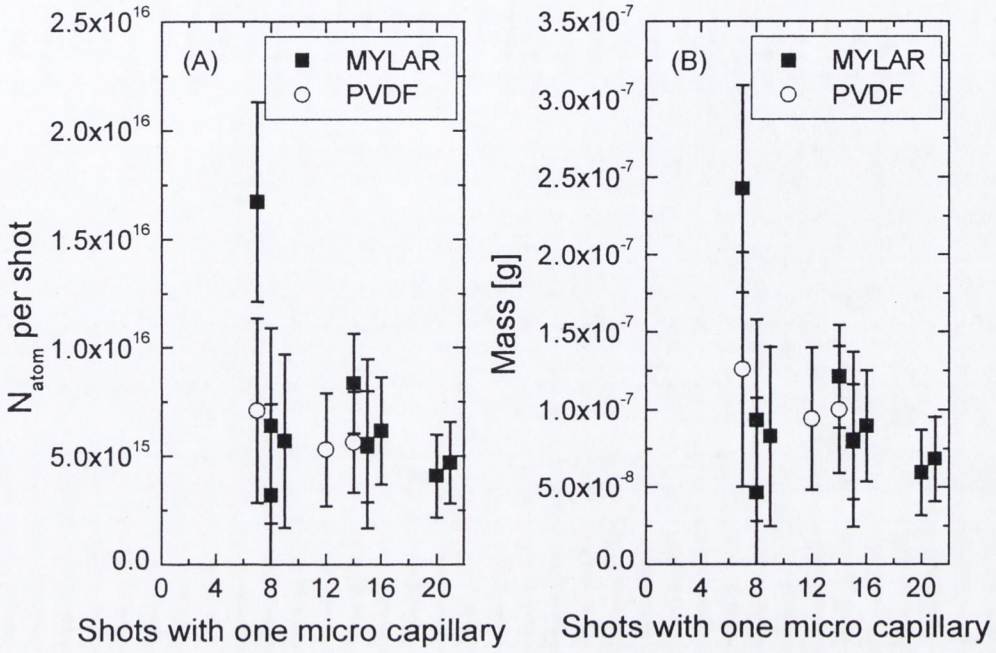

Figure 3.18: (A) Ablated number of particles per shot and (B) corresponding mass.

If we assume a mean ionisation $Z = 4$ and an ion mass $m_{ion} = 16u$ the mean free path can be calculated using Eq. (2.33); $\lambda_{ii} = \tau_{ii} \times v_{th} = a \times c_{s,0} \times (m_{ion} \times (k_B T_i)^3)^{1/2} / (Z^2 n_i) \sim a \times m_{ion}^2 \times c_{s,0}^4 / (Z^2 n_i)$, where $a = 6(2\pi^3)^{1/2} \varepsilon_0^2 / e^4 \ln\Lambda$ and $c_{s,0}$ is the ion sound velocity. We can estimate the density from Figure 3.18(A) by dividing with the volume of the micro capillary, $\sim \pi \times 80 \times 50^2$ μm^3, to yield $n_{ion} \sim 10^{27}$ m^{-3}. As the velocity, we assume the sound velocity $c_s \sim 14$ km s^{-1} (see Eq. (2.15)). The ratio of E/M is obtained from Figure 3.18(B) as 0.05/80 J/ng. With these values, we find that $\lambda_{ii} \sim 1.5$ nm – hence much smaller that the scale of the plasma plume itself. This confirms that the initial stage of the plasma plume evolution is highly collisional and a hydrodynamic description can therefore be appropriate.

The initial input to the program is the dimension of the plume, X_0, Y_0 and Z_0. We will assume that after half an oscillation of the current in the discharge i.e. after 2 ns (see

Figure 3.9) a plume is formed on top of the micro capillary exit with lateral dimensions equal to the micro capillary i.e. $X_0 = Y_0 \sim 50$ μm. The thickness $Z_0 \sim 30$ μm of this plume is estimated from (2.14) using $\tau_{laser} \rightarrow 2$ ns and taking for the sound velocity $c_{s,0} \sim 14$ km/s as explained above. The result of the calculation for the flux of particles (see Eq. (2.10)) at a distance of 40 cm is shown if Figure 3.19, along with that of the current recorded by a probe at this position. The model shows a broad resemblance to the experiment. The peak flux in the model ($K_M \sim 4.5\times10^{-9}$) can be related to the real current per sr by $d_{probe}^2 \times K_M \times \beta^{1/2} \times N_{atom}/(I_1(\gamma)X_0)$ (Eq. (2.10)), which gives a value of ~75 A sr^{-1}, for $N_{atom} = 5\times10^{15}$, $\beta^{1/2} = 1.5\times10^5$, $I_1(\gamma) = 0.22$ and $X_0 = 0.005$ cm. Given the uncertainty in the parameters this is a reasonable value.

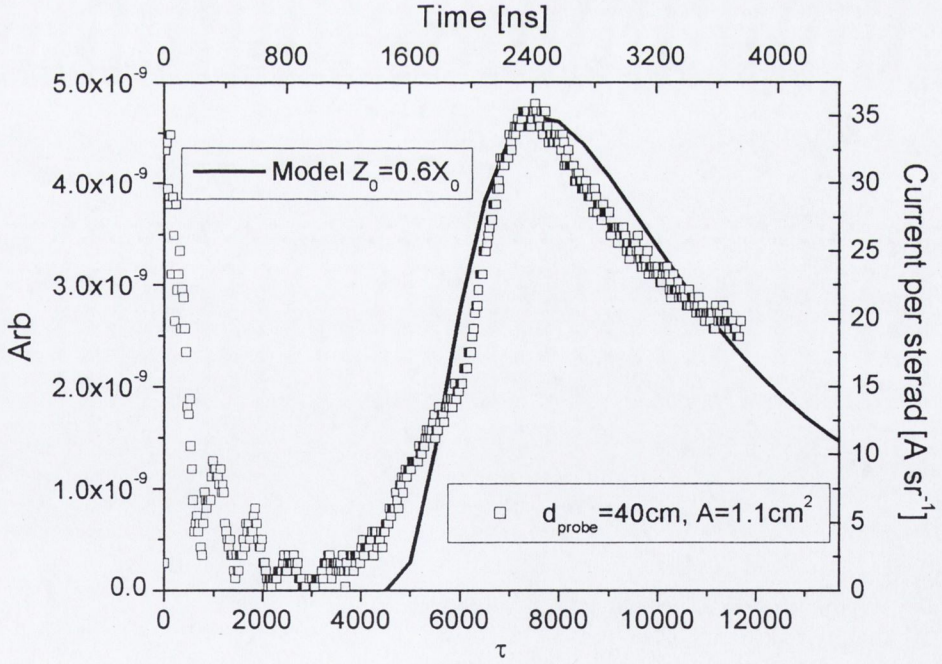

Figure 3.19: Comparison of the flux calculated with the model of Anisimov and that recorded by a Langmuir probe. At the peak flux we find that $\tau = 1$ corresponds to ~0.32 ns. Experiment with $V_p \sim 8.5$ kV.

We will show in Chapter 5 and Appendix B how the relative change of the probe signal at increasing angles can be used to show the good prediction by the model of a laser ablation experiment. However, as remarked in Chapter 3.1, due to the design of the insert in the discharge cell there is a limited free expansion angle of only ~17° to the normal which prevents us from making these experiments in the case with the micro capillary source.

3.3.3 Concluding remarks

The asymptotic free expansion of the fast ions from a novel micro capillary discharge source is investigated using electrostatic probes. From the measurements of the expansion velocity we can assume a typical initial sound velocity of >14 km s^{-1} corresponding to ion energies of several keV, Eq. (2.19).

Since the sound velocity, $c_{s,0}$, is at least larger than ~1.4×10^4 m s^{-1}, it follows from its definition in Eq. (2.20) that the initial electron temperature should be at least larger than $k_bT_e > 5$ eV for a carbon ion mass (12u) with $Z = 4$. It should be noted that this estimate depends quadratically on the measured front velocity of the plume and the value used in this estimate is very much a lower limit. At the higher front velocity of ~3.5×10^5 m s^{-1} measured with a negative charging the temperature could be as high as ~50 eV.

Even higher hold-on-voltage and hence expansion velocities etc. may be obtained by shortening the transmission lines used from the capacitor bank to the discharge cell. In the experiment reported here a cable length of 25 m was used (see Chapter 3.1) in order to obtain sufficient time delay to trigger various diagnostic equipment on the vacuum chamber.

As was mentioned in the overview section at the beginning of Chapter 3 the micro capillary experimental setup represents an interesting new "mini" pulsed power system. A phenomenon well known in larger discharge experiments is that of pinching or focusing (i.e. the name *Z*-pinch of some experiments) of the plasma when high current rates are applied. The basis of describing when the pinch reaches a stationary equilibrium is given by the *Bennett*-relation [Bennett 1934]. Recently the pinch dynamics of different experiments have been reviewed in papers by [Pereira & Davis 1988] and [Koshelev & Pereira 1991]. In the *Bennett*-pinch the radial plasma pressure equals the Lorentz force:

$$\left(\nabla p + \mathbf{j} \times \mathbf{B}\right)_r = 0 \qquad (3.21).$$

Taking $B = \mu_0 I/2\pi r$ and $j = I/\pi r^2$ and $p = (n_i+n_e)k_bT$ where n_i and n_e are the electron and ion densities and the plasma temperature T is assumed equal for electron and ions - we find from integration that:

$$\frac{\mu_0 I^2}{4\pi} = N_i\left(1+Z\right)k_bT_e \qquad (3.22).$$

Here N_i is the number of ions per unit length and Z the effective ionisation. We can evaluate the maximum temperature for the pinching assuming $N_i \sim (5\times10^{15}/80)\times10^6$ (see Figure 3.17), $Z \sim 4$ and $I = 50$ kA (see Figure 3.9). The results is $k_bT_e \sim 5$ eV. From the estimate above, of the electron temperature deduced using the probe signals, it therefore seems that the plasma pressure is too high for the *Bennett*-relation to be fulfilled. That is, the Lorentz-force is not big enough to overcome the plasma pressure and it is concluded that pinching is not obtained in these experiments. However while $T_e^{1/2} \sim c_{s,0} \sim v_{\text{front}} \sim V_p$ (Figure 3.17 and (3.21)) we have that $I \sim V_p$ (Figure 3.10) hence for a higher hold-on-voltage the plasma temperature

should only increase with the square-root but the *Bennett*-temperature from (3.21) would increase with the square of the higher hold-on-voltage i.e. the scaling favours pinching to occur.

3.4 Ion outflow from the micro capillary as measured with a Thomson parabola analyser

3.4.1 Introduction to the Thomson parabola analyser

The Thomson parabola analyser [Thomson 1913] allows determining the velocity and charge to mass ratio of ions by measuring the deflection of the particles acted upon by simultaneous parallel magnetic and electric fields. The Thomson parabola analyser (TPA) reported in the following was designed, fabricated and implemented during the time of the project. The measurements presented differ from many other experiments, where the TPA has been used, in that it was combined with a temporal detection resolution of the ion dynamics. This is achieved by utilising a microchannel plate (MCP) as an amplifying, position-sensitive detector for the ions. The MCP is working as a high-speed shutter to the ions by gating the voltage on it. This allows us to obtain a 15 ns framing of the ion temporal dynamics. A similar arrangement was reported by [Matsuzawa *et al.* 1985] for investigations on a pulsed ion-beam generator. A time-resolvable Thomson analyser was also reported by [Rhee *et al.* 1987], though here the temporal information is deduced by varying the electric deflection field of the TPA. For other uses of Thomson parabola analysers see e.g. [Rhee 1984] and [Herold *et al.* 1981] and references in there.

Using the Thomson parabola analyser the charge and mass of the species in the expanding plume can be determined. Of course like with the electrostatic probe only the ionised component of the plume is subject to the investigation and the experiment hence provides no information about the neutral part of the plume.

3.4.2 Experiment

Figure 3.20 shows the layout of the experiments conducted at LPTP in France where all the data presented in this section is obtained. Part (A) depicts the general setup.

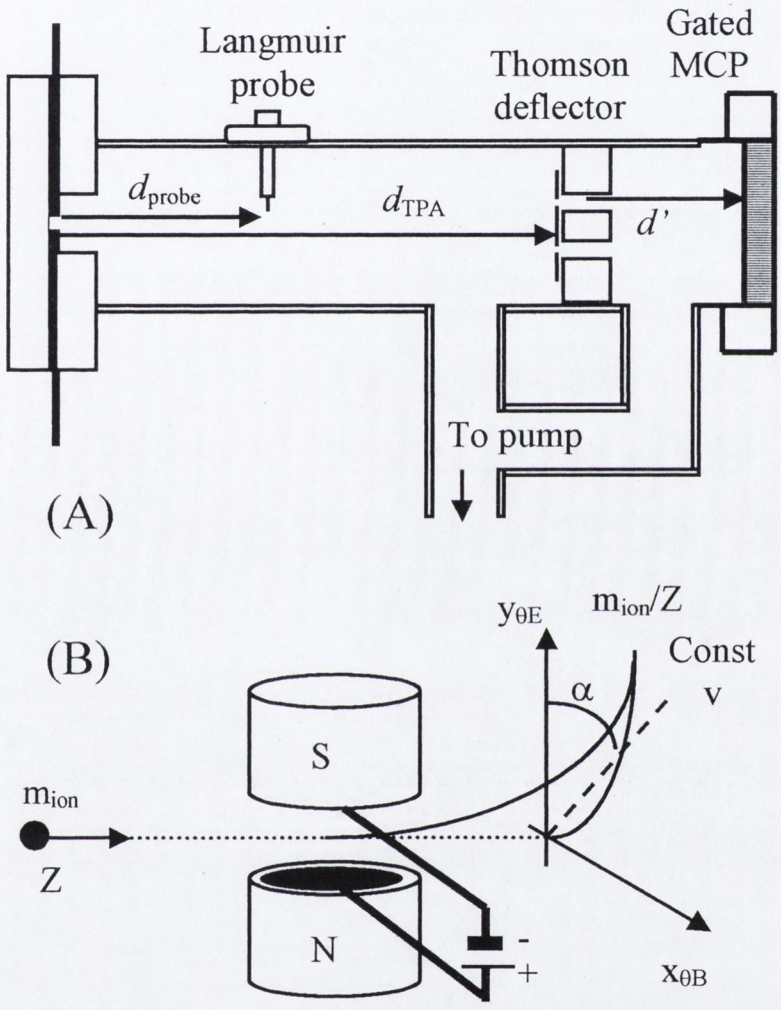

Figure 3.20: (A) Sketch of the micro-capillary setup with a Thomson parabola analyser (d_{probe}=13 cm, d_{TPA}=39 cm). Deflector to MCP distance is 60 mm. (B) Principle of the Thomson parabola analyser.

The TPA is situated $d_{TPA} = 39$ cm from the micro capillary discharge and with a distance $d' = 60$ mm between the deflector unit and the microchannel-plate (MCP). The pressure on both sides of the TPA is as usual in the experiments with the micro capillary $<10^{-3}$ mbar (0.1 Pa). Also present in the vacuum chamber is an electrostatic

probe connected to a fast digital oscilloscope (500 MHz, 2Gb s^{-1}) that allows us to monitor the ion outflow on a shot-to-shot basis.

Part (B) in Figure 3.20 shows the principle of the deflection in the TPA. Parallel magnetic and electric fields applied perpendicular to the ion trajectory disperse the ions. In the simplest analysis it is assumed that the fields are uniform over length L the diameter of the magnets, see below, and zero outside. The deflection in the plane at right angles to the initial path can be written [Rhee 1984]:

$$\tan\theta_B = \frac{Ze}{m_{ion}}\frac{BL}{v} \quad \text{(A)} \qquad \tan\theta_E = \frac{Ze}{m_{ion}}\frac{EL}{v^2} \quad \text{(B)} \qquad (3.23).$$

Here θ_B and θ_E are the magnetic- and electric deflection angles for the applied magnetic, B, and electric, E, fields and Z is the charge of the ion with mass m_{ion} and speed v. It follows from (3.23) that

$$v = \frac{EL}{BL}\frac{\tan\theta_B}{\tan\theta_E} \quad \text{(A)} \qquad \tan\theta_E = \frac{m_{ion}}{Ze}\frac{EL}{(BL)^2}\tan^2\theta_B \quad \text{(B)} \quad (3.24).$$

Hence ions with different charge-to-mass ratio but the same speed will fall on a straight line through the origin. If the angle between the constant velocity line v and the electric deflection direction is defined as α we have that:

$$\tan\alpha \equiv \frac{BL}{EL}v \qquad (3.25).$$

And ions with the same charge-to-mass ratio but different v fall on the parabola defined by Eq. (3.24)(B).

3.4.3. Thomson parabola analyser design

In the design investigated, four separate Thomson analyser deflection centres were build into one compact unit, Figure 3.21 depicts the outline. The four analysers were

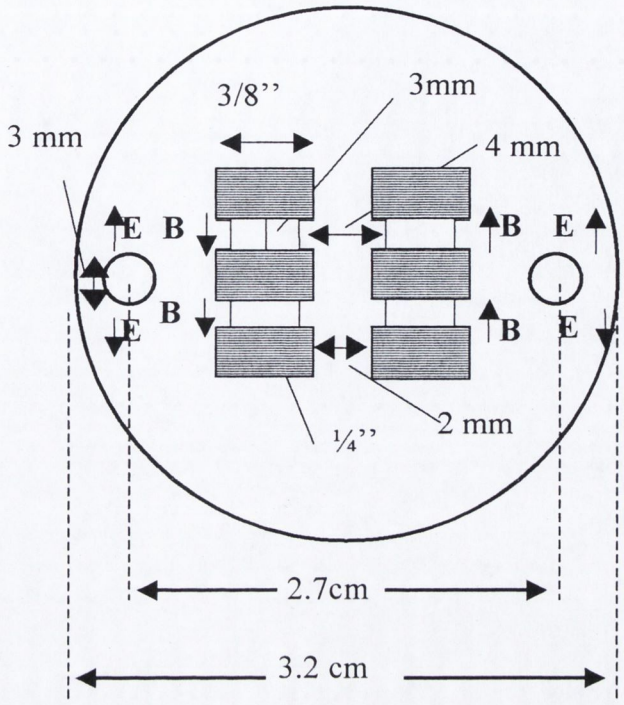

Figure 3.21: Deflector consisting of 4 separate Thomson parabola analyser centres formed by six magnets (line-pattern). The deflection fields shown correspond to in the experiment for ions travelling into the paper.

placed around the central axis of the setup; one in each quadrant and as close to the centre as physically possible. Six slots were milled in a nylon base to support the permanent magnets. The disc shaped magnets (Alnico, from Edmund Scientific) had a diameter of L = 1 cm and they formed 4 through passages of δ = 0.3 cm height. The narrow slits were made to ensure good homogeneity of the field in the gap. On top of the magnet surfaces a thin sheet of copper deposited Kapton™ foil [Goodfellow Catalogue 2000] is placed. It is connected to a voltage supply providing the potential drop for the electrical deflection. Typically the potential drop was 40 V, corresponding to an EL-product of $EL = 40L/\delta \sim 140$ V. The magnetic flux is measured with a small Hall-probe of 3 mm diameter (Hirst - Gaussmeter). The measurements of the B-field in the four slits are shown in Figure 3.22 below - the average integrated value is seen to be $BL = (1.1 \pm 0.1)\ 10^{-3}$ Tm. The value drops

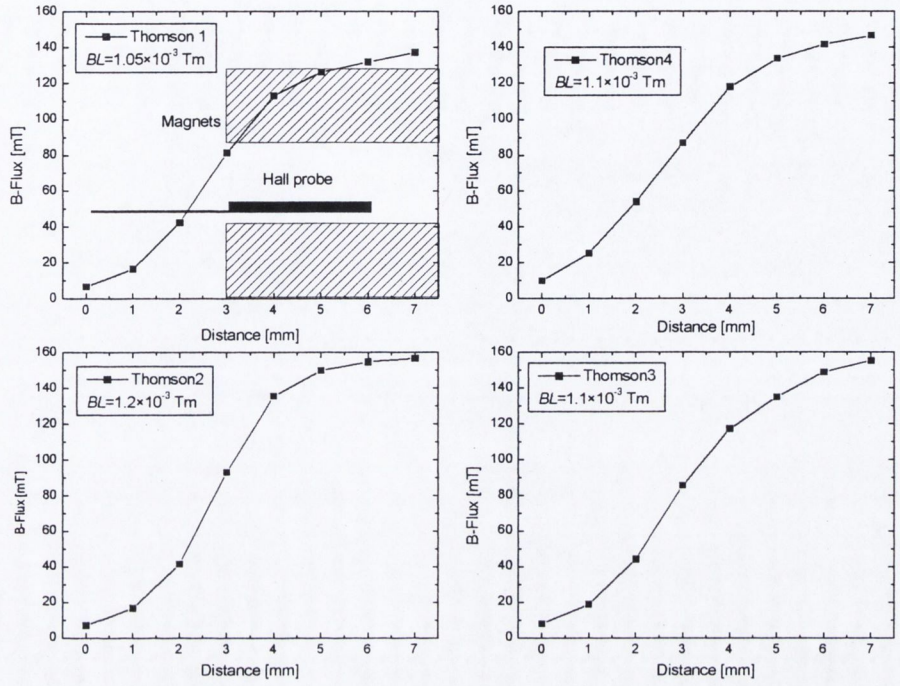

Figure 3.22: Measurement of the position resolved *B*-field in the four slits of the compact multi-TPA used in the experiment. The drawing in the top left depicts the definition of the distance scale.

rapidly as the detecting surface of the Hall probe is outside of the slit i.e. after ~2 mm confirming that the flux is confined to the gap between the magnets.

To secure a well-defined beam in the gap a circular aperture is used in front of the entrance of each of the gaps. The aperture has a radius $r_a = 0.3$ mm. We shall see later the *maximum* ion current that enters the gap is ~30 μA hence J~100 A m^{-2}. If this beam of plasma is stripped of its electrons the electric field on the surface of the ion column can be calculated from $2\pi r_a E = J\pi r_a^2/\varepsilon_0 v$ where the velocity v~2×10^5 ms^{-1}. Using the numbers above we find $E = (100\times0.3\times10^{-3})/(2\varepsilon_0\times2\times10^5) = 9$ V mm^{-1}. This is of the same order of magnitude of the applied deflection field (40/3 =13 V mm^{-1}) and hence can introduce a spread in the beam in the electrical deflection direction.

3.4.4. The microchannel plate as ion detector

To obtain the temporal information of the ion analysis we use a microchannel plate as ion detector. A microchannel plate is an array of miniature electron multipliers. When an electron is released from the walls of one of the channels due to a particle impact (photons, electrons or ions) it is accelerated down the tube creating more secondary electrons by collisions with the wall. At the output a phosphor converts the electrons into light. Often a fiber-bundle is used as an optic output window to a photographic film or a charge-coupled device (CCD) [Wiza 1979] [Siegmund 2000]. The typical spatial resolution is ~15 μm.

The MCP, used in these investigations, is a 4-quadrant unit with the gating electrode deposited over the output phosphor [Dumitrescu-Zoita 1996] and [Sopkin *et al.* 1991]. The gating voltage is applied over the stack of the microchannel plate and phosphor simultaneously. Each quadrant can be separately gated from a HV-gating supply with a pulse that is typically ~6 kV and with a width of 15 ns. A pickup-coil at the primary capacitor bank is used to trigger a delay generator that controls the HV-gating supply.

Microchannel plates are most often used to detect photons or electrons and there is not much information available on the detection efficiency for ions. In [Gao *et al.* 1984] the absolute efficiency for O^+ particles, with beam energy from 1 – 5 keV, is reported to be almost constant 50%. There is no change for lighter ions (He^+, H^+). This study is supported by a recent study with heavier noble gas ions [Oberheide *et al.* 1997] where similar efficiencies were found for the same energy range. The data by Gao *et al.* is reproduced in Figure 3.23 below.

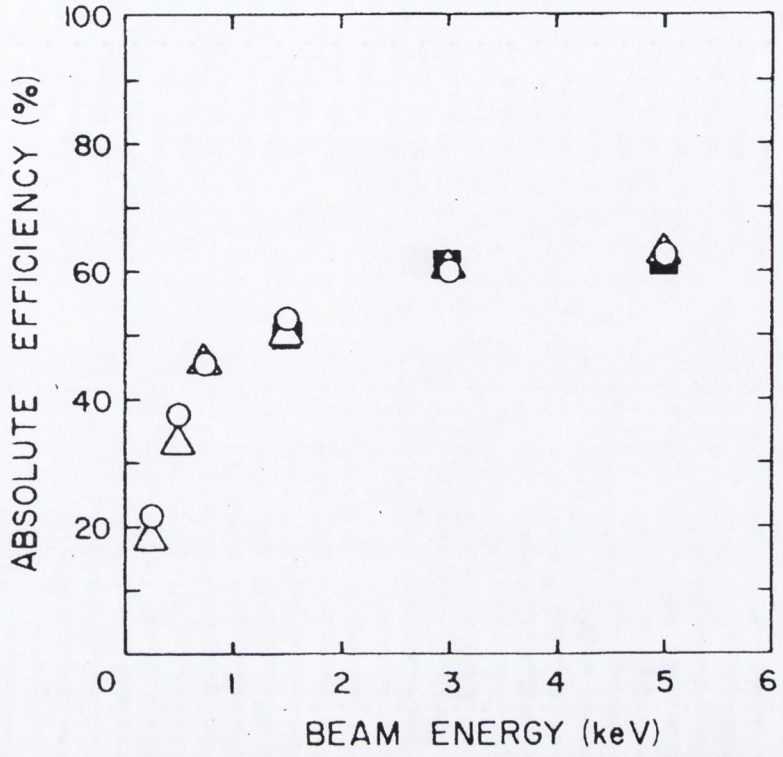

Figure 3.23: MCP ion detection efficiency. H^+ (O), He^+ (Δ) and O^+ (■) [Gao *et al.* 1984].

To record the image of the MCP output we use a 35mm photographic film (HP5 Plus 400, black and white). The film is developed in Kodak TMax P3200 developer and fixer. The development time is standard 10 min followed by 4 min in the fixer. HP5 film is also used for the spectroscopy work reported elsewhere in this thesis. After the film has been developed it is scanned for subsequent analysis using a commercial scanner with 2400 ppi and 16-bit. The transmission of the film is thus represented on a scale from 0-65535 where 0 correspond to the darkest reading.

3.4.5 Results

Below we show an example of a picture recorded of the output of the MCP in an experiment with the compact 4-quadrant TPA dispersing the ions from a Mylar microcapillary discharge plasma. First we observe that the origin for the deflection is clearly visible as the intense spots closest to the centre of the frames. This spot is generated by neutral atoms and photons emitted by the plasma and not affected by the fields in the Thomson analyser. This was checked with recordings where the MCP is gated on at an early time after the breakdown where the ions have not yet expanded to the distance of the MCP. Here this spot is visible as well, the cause of it being the detection of photons emitted by the plasma.

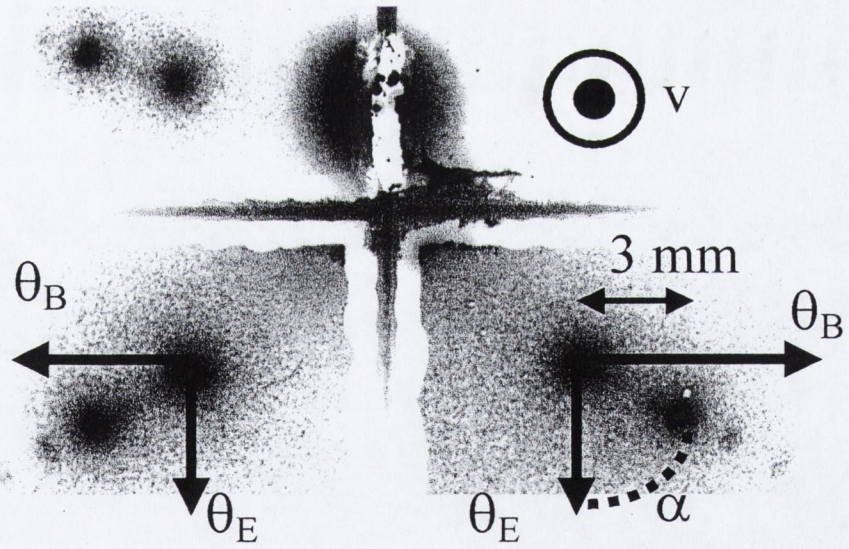

Figure 3.24: Picture of the output from a Thomson parabola analyser as recorded by a 4-quadrant MCP. The ions are dispersed by the magnetic and electric fields along the axes shown on two of the frames. The MCP is activated for 15 ns at t_{MCP} = 1.901, 1.846 and 1.851 μs counter-clockwise around the picture starting from the top left. The pulse on the last frame was sent to the oscilloscope to record the timing. Breakdown of a Mylar micro-capillary (-11.7 kV).

Also, a measurement on the film of the relative distance between the spots shows that it corresponds to the linear projection of the apertures in front of the slits in the TPA onto the MCP.

We note that the different deflected spots corresponding to ions of different charge-to-mass ratios all fall on a straight line through the origin. As we deduced in formula (3.25) this corresponds to ions travelling at the same velocity. When the gating of the MCP is changed to another time after breakdown the angle α between the spots and the electric deflection axis changes as well. In Figure 3.25 we show a record, for a micro capillary discharge experiment, of a series of shots with different delay times, t_{MCP}, from the breakdown. For each of the shots α is measured on the film and $\tan\alpha$ is calculated. From (3.25) we calculate the velocity assuming the measured values of the *EL*- and *BL*-products in section 3.4.3. Also shown is the value of the velocity calculated assuming an inertial expansion of the plume $v = d_{MCP}/t_{MCP}$ - it is seen that *the two velocity measurements are in agreement.* Though the plume experiences an initial acceleration before the velocity becomes constant (see the model of Anisimov) this phase is limited to a very early stage after the breakdown, and for most of the distance from the discharge cell to the MCP the plume expands without acceleration. This inertial expansion, at long distances from the discharge cell, was also evident from the double probe experiments presented in the previous chapter. The uncertainty in the angle arises due to the finite size of the spots and from the uncertainty in determining the base axes.

For the series of shots in Figure 3.25 the averaged probe signal is shown in Figure 3.26. The figure gives as well the current scaled to the position of the MCP and corrected with the area of the aperture of the TPA. As shown in section 3.3 the

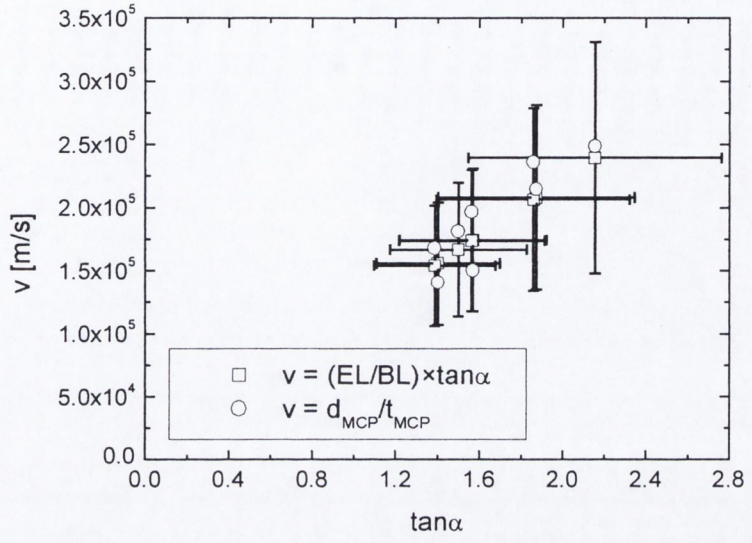

Figure 3.25: (□) Velocity deduced from the measured deflection angle in a TPA for a Mylar micro-capillary discharge with charging voltages in between -11.7 and -13.6 kV. (○) Constant velocity assumption. The uncertainties shown are those of measuring the angle α - taken to be $\pm 5^{\circ}$.

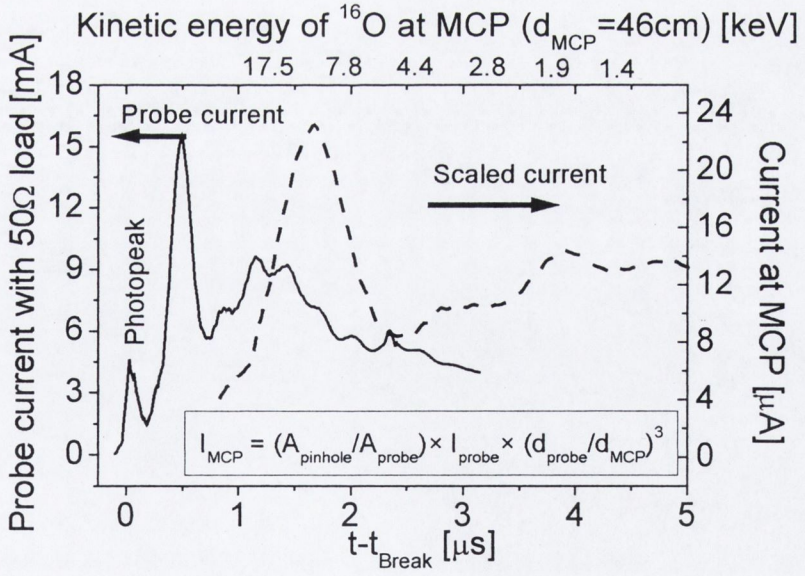

Figure 3.26: Left axis: Langmuir probe current at d_{probe} = 13 cm. Right axis: The scaled current at the MCP. The free-flight kinetic energy of an O-particle is calculated on the top. (Mylar microcapillary discharge with V_p = -11.7 to -13.6 kV).

current at one position can be used to predict the current at another position to a good accuracy. When the MCP is gated on at different times during the ion pulse a series of snapshot of the charge distribution is obtained as a function of time - a few examples of which are shown in Figure 3.27 as open circles. In this figure, the *deflection*, along the magnetic and electric deflection axes ($x_{\theta B}$ and $y_{\theta E}$), is *calculated by projecting* the spots onto the respectively axes using the measured angle α and the distance along the constant velocity line. The "theoretical" points (solid box) are the positions expected for the respective ions, calculated using (3.23) and assuming the constant velocity depicted in Figure 3.25. Similar plots of experimental and theoretical deflections are shown in Figure 3.28 but for a positive hold-on-voltage.

The measurements stretch over the time of the first peak in the probe. At later times i.e. after ~3.5 μs no more ions are detected which is ascribed to the decrease of sensitivity of the MCP at lower energies. The charge and mass of the ions in the second peak, detected by the probe, have therefore only been partly resolved. Measurements have to be done late enough to detect some of the peak, yet still so early that the energy of the ions is high enough, that they can be detected by the MCP. In the experiments we register the *highest charged ions* at the *early gating* times. Comparing the deflections from the measurements with the theoretical points in Figures 3.27 - 28 implies that C and O ions are the dominant ions detected. Charges up to +3e to +4e are present in the first peak. Due to the similar m_{ion}/Z ratio of carbon +3 and oxygen +4 the two ions will not be distinguishable. As the MCP is gated on later during the decrease in the signal between the two peaks only one ion species is detected. This seems to be O^{2+}. This is observed for both positive and negative pulse charging of the discharge cell. As the

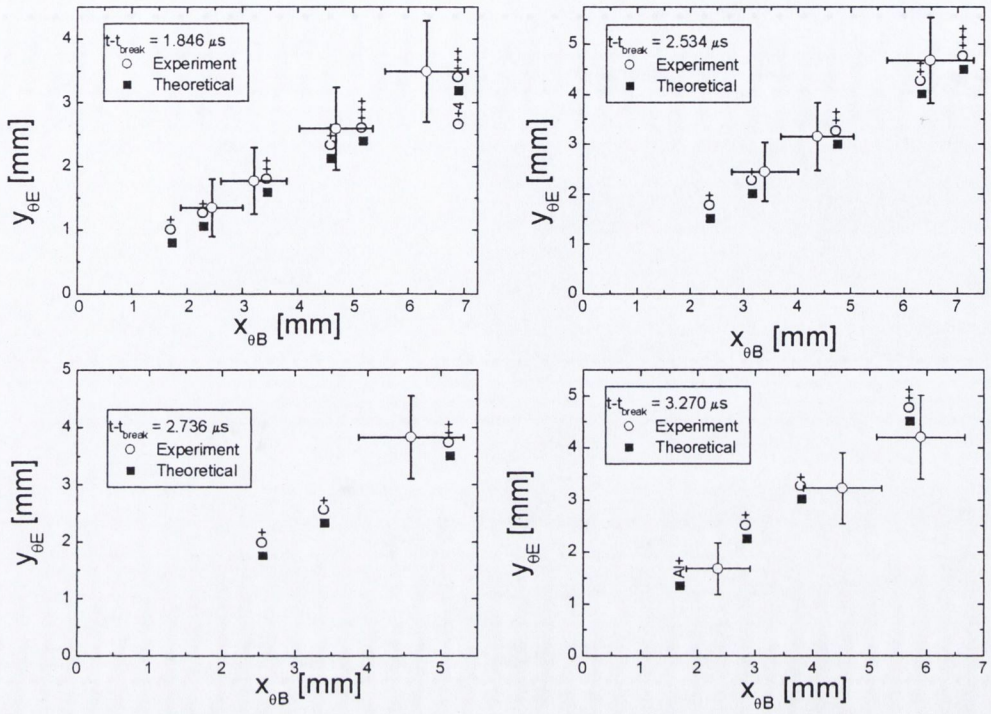

Figure 3.27: Experimental (o) and theoretical (■) deflections of ions at different times from breakdown. Mylar microcapillary, V_p = -11.7 to - 13.6 kV.

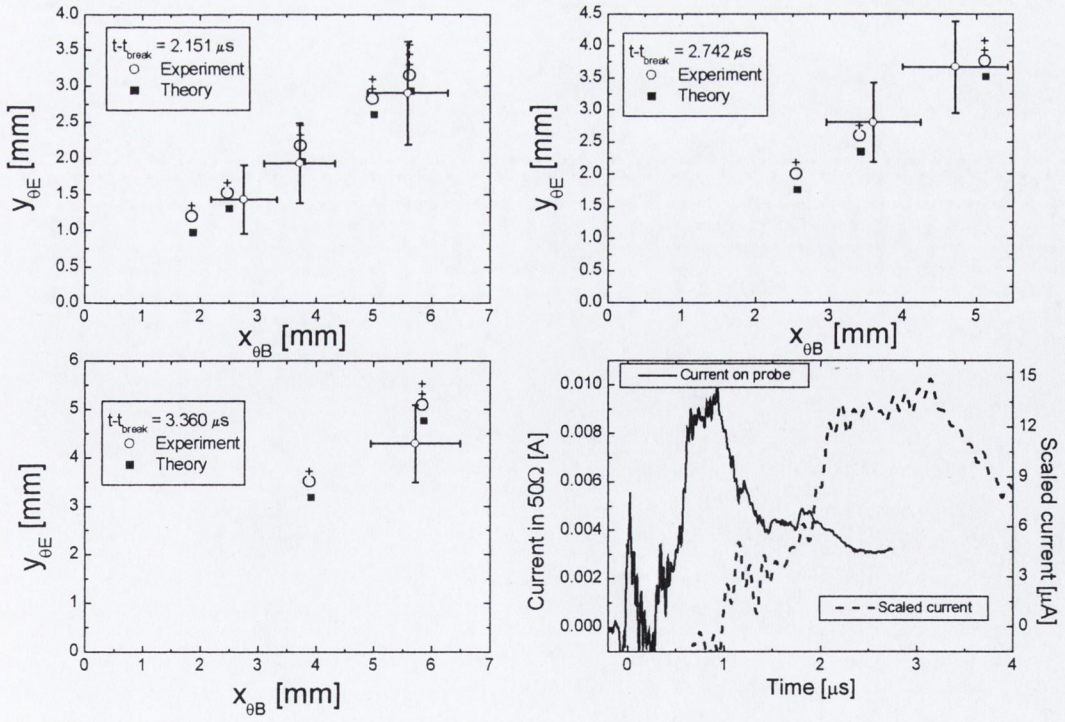

Figure 3.28: Experimental (o) and theoretical (■) deflections of ions at different times from breakdown. Mylar microcapillary discharge with V_p = 8.3 to 9.7 kV. Also shown, the average Langmuir probe current and the scaled current at the MCP as in Figure 3.26.

time is further increased a wider variety of ions is again observed. We note that at the later gating times the more highly charged species cannot be detected as they are outside the field of observation. Also H^+, with its low mass, is deflected outside the field of observation, for the configuration employed here. The largest possible deflection along any axis that can still be recorded is about 1 cm limited by the size of the MCP. Table 3.2 gives a short list of the gating time at which a carbon ion will still be visible on the active area of the MCP, if it is deflected along the magnetic deflection axis in the setup discussed in Figure 3.20.

	A_{ion}/Z	$t_{10\,mm}$ (μs)
C^{+2}	6	4
C^{+3}	4	2.7
C^{+4}	3	2

Table 3.2: Table of maximum detection time of different carbon ions.

Hence a C^{+2} ion can be followed up to 4 μs after the breakdown of the micro capillary with the present setup. However we remember that the MCP detection efficiency decreases rapidly for particle energies less than ~2 keV which will in practise then set the limit.

3.4.6 Discussion of TPA results

As already commented the plasma in the micro capillary resembles that from a pulsed laser produced plasma in that they are both expanding fast and of a transient nature. The macroscopic expansion of the microcapillary plasma, as investigated with probes in the previous chapter, could also be treated very similar to that in laser

ablation experiments, see chapter 5. It was found that a simple hydrodynamic expansion model could be applied satisfactorily to measurements of the macroscopic charge expansion. With the Thomson parabola analyser results we have however a more detailed picture of the temporal evolution of the ion distribution. We will discuss the results in the frame of a detailed model, taking into account recombination effects during the expansion into vacuum of a transient plasma. [Voronov and Chernyshev 1974] [Goforth and Hammerling 1976] and [Payne *et al.* 1978]. The model was originally applied to laser produced plasmas but the underlying physics should be the same in the case of the micro capillary.

From the recorded film of the MCP output we can evaluate the exposure of the film knowing the film characteristic. We note that the exposure is related to the film density by $E = E_0 \times 10^{D/\gamma}$. Using the information from the experiment in Figure 3.27 allows us to deduce the ion distribution for the case of negative pulse charging, see Figure 3.29. The relative film exposure E/E_0 on the abscissa in this figure is calculated from the expression:

$$E = (1/T)^{1/\gamma} = (65535/i)^{1/0.65} \tag{3.27}$$

Here T is the transmission and i the greyscale intensity measured on the scanned film ($0 - 65535 = 2^{16}$). The top graph in Figure 3.29 gives the various resolved ion charge distributions. Since, the C^{+3} and O^{+4} ions cannot be distinguished by the TPA due to the same mass-to-charge ratio, that plot is labelled with both ions. Also, from Figure 3.27 and 3.28 it is seen that the theoretical positions of the C^{+2} and O^{+3} peaks are too close to be resolved within the uncertainty in the present experiment and therefore the spot recorded here has a double labelling as well. It was found in [Payne et al. 1978] that with a channeltron electron multiplier array (a MCP!) the charge per area

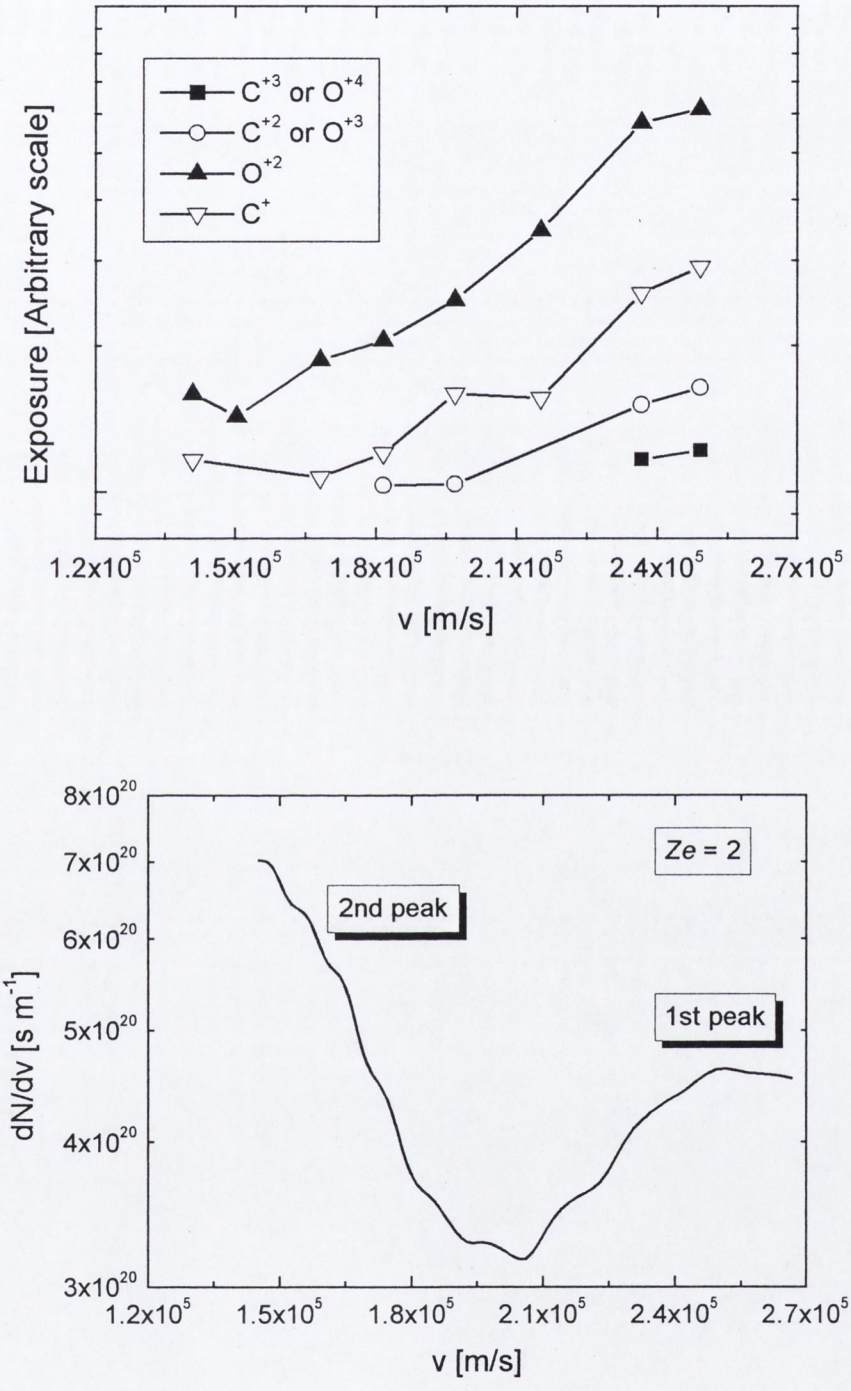

Figure 3.29: (TOP) Relative ion distribution as deduced from TPA measurements (Figure 3.27). Mylar microcapillary discharge with V_p = -11.7 to - 13.6 kV. (BOTTOM) Ion distribution expected for the scaled current at d_{MCP} = 46 cm (see Figure 3.26).

(S) times the ion charge (Z) scales with the recorded film density (D) as $ZS = Ae^{bD}$, where A and b are constants. Hence we can assume that the top graph in Figure 3.29 represents the ion charge state distributions (number of ions with the given charge as a function of ion velocity). The bottom graph in Figure 3.29 shows the ion distribution calculated from the probe signal in Figure 3.26. To calculate the ion distribution in the bottom graph we assumed that all the particles had a charge of $+2e$. The expression for the number of ions with velocity from v to $v+dv$ is:

$$\frac{dN}{dv} = \frac{t^2 I_{MCP}(t)}{Zed_{MCP}} \qquad (3.28).$$

To deduce this expression it is assumed that the velocity is given by $v = d_{MCP}/t$. The qualitative shape, in the given velocity range of the two graphs, differs substantially at low velocity. However, as we found in Figure 3.16, the second peak in the ion-signal is slowing down so the expression (3.28) cannot be applied to that region. Besides, the detection efficiency of the MCP is falling fast as the kinetic energy decreases, see Figure 3.23. Unfortunately in these experiments, we did not succeed to obtain pictures at earlier times (higher velocity) that could have shown the distributions over the whole of the first peak in the detected probe signal. The measured ion distribution of the O^{+2} ion appears to have reached its maximum, though that is really only speculation.

Payne *et al.* [Payne *et al.* 1978] used a TPA to analyse the ions in a Be laser plasma generated using power densities of a few times 10^{14} W cm^{-2} (infrared wavelength, 200 ps). We reproduce their measured ion distribution below as inspiration, Figure 3.30. In the figure it is seen that the highest charged ions arrive at the earliest times (highest velocities) while lower charged ions arrive later with a lower velocity. Payne

et al. obtained good agreement between their results and the model they proposed. In their model they solve the three hydrodynamic equations in Chapter 2.1 in a spherical geometry *including* collisional-radiative recombination and ionisation and taking into account the thermal conductivity of the plasma plume. Similar approaches have been taken by [Goforth and Hammerling 1976] [Voronov and Chernyshev 1974] and [Stevefelt and Collins 1991], with much the same conclusions. As the plasma plume expands the temperature drops, and collisional 3-body recombination (3BR) should quickly proceed leaving no ions to be detected since one has that the rate coefficient for 3BR scales as $\sim n_e T_e^{-4.5}$ [Hutchinson (1987)].

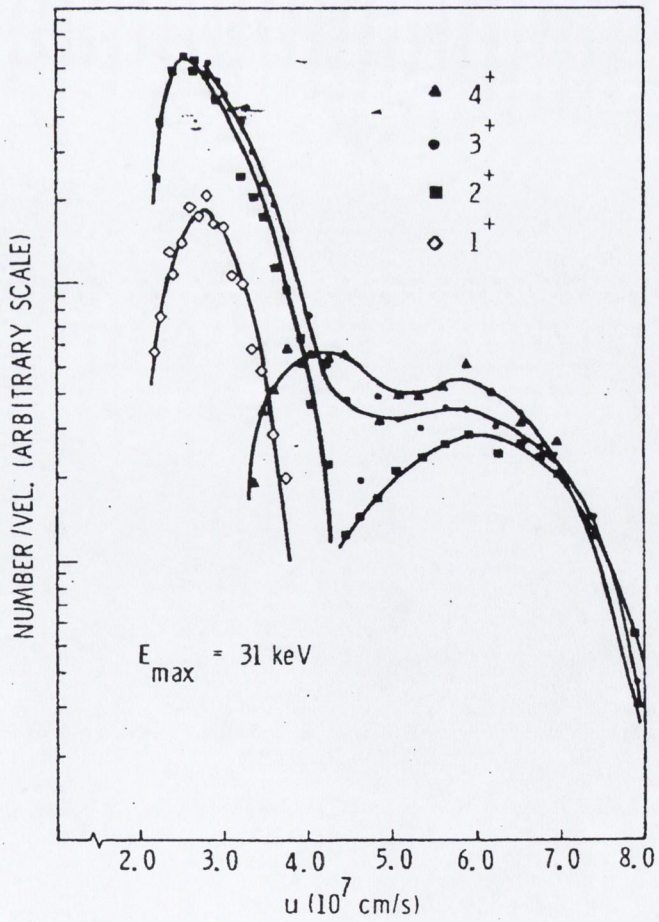

Figure 3.30: Ion distribution measured at 15 cm for a laser produced plasma [Payne et al. 1978]

However from the calculations in the models, it follows that when recombination is taken into account the energy returned to the free electrons in the plasma modifies the temperature scaling of the expanding plasma and thereby slows the 3BR process (- the cooling of the plasma is slowed). As the expansion proceeds there becomes insufficient collisions and the end result is that the ionisation can become constant or "*frozen-in*" as it is termed. As the 3BR rate-coefficient is also proportional to the density, the freezing in of the charge state happens earlier for low densities, which is why the highest charged ions are found at the front of the expanding plasma plume where the initial density is the lowest.

The *freezing-in*, and hence the final mean ionisation, depends on the initial plasma parameters. So the measurements of the ion charge distribution can be used as a diagnostics tools for the initial plasma. Payne *et al.* found that the mean ionisation in their expanding Be plasma is ~1 for an initial electron temperature of 10 eV increasing to ~2 for a 50 eV temperature. These results are in good correspondence with the measurements reported here and the plasma parameters deduced in the previous sections.

3.4.7 Conclusions

The ion charge distribution measurements, using the Thomson parabola analyser, show that the plume consists mainly of oxygen +2 and carbon +1 charges and with some smaller quantities of higher charge states as well. The presence of ions, at these late times, is explained by the model of [Payne et al. 1978] [Goforth and Hammerling 1976] and [Voronov and Chernyshev 1974]. The model explains the *freezing-in* of the ionisation in a fast expanding and recombining plasma plume. The

measurements of the ion charge distributions was limited by the geometry and the response of the MCP which only allowed a small range of gating times (and hence velocities) to be measured. Some of these problems can be overcome by varying the distance from the TPA to the MCP allowing highly charged ions to be captured over longer times.

References

[chap 3] Attwood D.T. (1999). "*Soft X-rays and Extreme Ultraviolet radiation: Principles and Applications*". (Cambridge University Press).

[chap 3] Bennett W.H. (1934). "*Magnetically Self-focusing Streams*". Phys. Rev. **45**, pp 890.

[chap 3] Ekdahl C.A. (1980). "*Voltage and current sensors for a high-density z-pinch experiment*". Rev. Sci. Intrum. **51**(12) pp 1645.

[chap 3] Cano G.L. (1973). "*Secondary electron emission from Au, Mo and CuBe by high-charge-number laser produced metal ions*". J. Appl. Phys. **44**(12), pp 5293.

[chap 3] Chen F.F. (1965). "*Electrical Probes*". In "*Plasma Diagnostic Techniques*". Eds. R.H. Huddlestone and S.L.Leonard (Academic Press, London).

[chap 3] Choi P (1983). "*Experiments on the formation of a very fast Z-pich*". Ph.D. thesis from University of London. Plasma Physics Group, Blackett Laboratory, Imperial College.

[chap 3] Choi P. and Favre M. (1998). "*Fast pulsed hollow cathode capillary discharge device*". Rev. Sci. Instrum. **69**(9) pp 3118.

[chap 3] Choi P. Lunney J.G. Engel A. Dumitrescu C. Hansen T.N. Krisch I. Larour J. Rous J. (1999). "*A 10^{13} A/s High Energy Density Micro Discharge Radiation Source*". 12th IEEE Int. Pulsed Power Conference Vol 1, Monterey 1999. Eds C. Stallings and H. Kirbie. (IEEE, Piscataway, NJ) pp 287.

[chap 3] Chung P.M. Talbot L. and Touryan K.J. (1975). "*Electrical Probes in Stationary and Flowing Plasmas*". (Springer Verlag, New York).

[chap 3] DiCapua (1986). "*High speed magnetic field and current measurements*". In "*Fast Electrical and Optical Measurements, Vol 1*". Eds. J.E. Thompson and L.H. Luessen (Nato ASI Series E **108**, Martinus Nijhoff Publisher), pp 223.

[chap 3] DiCapua (1986b). "*High speed electric field and voltage measurements*". In "*Fast Electrical and Optical Measurements, Vol 1*". Eds. J.E. Thompson and L.H. Luessen (Nato ASI Series E **108**, Martinus Nijhoff Publisher), pp 175.

[chap 3] Dumitrescu-Zoita C. (1996). "*X-ray emission from hot, dense, magnetized plasmas*". Le Grade de Doctor en Sciences. Universite de Paris-Sud U.F.R. Scientific D'Orsay.

[chap 3] Früngel F.B.A. (1965). "*High Speed Pulse Technology*". Vol 1, (Academic Press, New York, London).

[chap 3] Gao R.S. Gibner P.S. Newmark J.H. Smith K.A. Stebbings R.F. (1984). "*Absolute and angular efficiencies of a microchannel-plate position-sensitive detector*". Rev. Sci. Instrum. **55**(11), pp 1756.

[chap 3] Goforth R.R. and Hammerling P. (1976). "*Recombination in an expanding laser-produced plasma*". J. Appl. Phys. **47**(9), pp 3918.

[chap 3] Goodfellow Catalogue (2000).

[chap 3] Hansen T.N. Schou J. and Lunney J.G. (1998). "*Angle-resolved energy distribution of laser ablated silver ions in vacuum*". Appl. Phys. Lett. **72**(15), pp 1829.

[chap 3] Hansen T.N. Schou J. and Lunney J.G. (1999). "*Ion time-of-flight study of laser ablation of silver in low pressure gases*". Appl. Surf. Sci. **138-139**, pp 184.

[chap 3] Herold H. Mozer A. Sadowski M. and Schmidt H. (1981). "*Design and calibration of a Thomson ion analyser for plasma focus studies*". Rev. Sci. Instrum. **52**(1), pp 24.

[chap 3] Hong D. Dussart R. Cachoncinlle C. Rosenfeld W. Gotze S. Pons J. Viladrosa R. Fleurier C. and Pouvesle J.-M. (2000). "*Study of a fast ablative capillary discharge dedicated to soft x-ray production*". Rev. Sci. Instrum. **71**(1), pp 15.

[chap 3] Hutchinson I.H. (1987). "*Principles of plasma diagnostics*". Cambridge University Press.

[chap 3] ITRS (1999). "*International Technology Roadmap for Semiconductors*". http://public.itrs.net/files/1999_SIA_Roadmap/Home.htm.

[chap 3] Jordan R. and Lunney J.G. (1998). "*Investigations of excimer laser ablation of iron*". Appl. Surf. Sci. **127-129**, pp 968.

[chap 3] Koopman D.W. (1971). "*Langmuir Probe and Microwave Measurements of the Properties of Streaming Plasmas Generated by Focused Laser Pulses*". Phys. Fluids **14**(8), pp 1707.

[chap 3] Koshelev K.N. and Pereira N.R. (1991). "*Plasma points and radiative collapse in vacuum sparks*". **69**(10), pp R21.

[chap 3] Leonard S.L. (1965). "*Basic Macroscopic Measurements*". In "*Plasma Diagnostic Techniques*". Eds R.H. Huddlestone and S.L. Leonard. (Academic Press, New York, London).

[chap 3] Lunney J.G. Lawler J.F. and Aratari R. (1993). "Ion emission studies of pulsed laser evaporation of Yba2Cu3O7". J. Appl. Phys. **74**(6) pp 4277.

[chap 3] Matsuzawa T. Takahashi A. Masugata K. Ito M. Matsui M and Yatsui K. (1985). "*Time-resolvable measurements of energy and species of an intense pulsed ion beam*". Rev. Sci. Instrum. **56**(12), pp 2279.

[chap 3] Mott-Smith H.M. and Langmuir I. (1926). "*The Theory of Collectors in Gaseous Discharges*". Phys. Rev. **28**, pp 727.

[chap 3] MicroSim Corporation (1997). MicroSim Schematics Evaluation Version 8.0. See e.g. http://pcb.cadence.com/Product/Simulation/Pspice/eval.asp.

[chap 3] NRL (2000). "*NRL Plasma Formulary*". *Ed.* J.D. Huba. (The Office of Naval Research, USA).

[chap 3] Oberheide J. Wilhelms P. and Zimmer M. (1997). "*New results on the absolute ion detection efficiencies of a microchannel plate*". Meas. Sci. Tehnol. **8**, pp 351.

[chap 3] Payne G.L. Perez J.D. Sharp T.E. and Watson B.A. (1978). "*Recombination effects in an expanding laser-produced plasma*". J. Appl. Phys. **49**(9), pp 4688.

[chap 3] Pereira N.R. and Davis J. (1988). "*X-rays from z-pinches on relativistic electron-beam generators*". J. Appl. Phys. **64**(3), pp R1.

[chap 3] Pfeiffer W. (1986). "*Ultrafast electrical voltage and current monitors*". In "*Fast Electrical and Optical Measurements, Vol 1*". Eds. J.E. Thompson and L.H. Luessen (Nato ASI Series E **108**, Martinus Nijhoff Publisher), pp 145.

[chap 3] Rhee M.J. (1984). "*Compact Thomson spectrometer*". Rev. Sci. Instrum. **55**(8), pp1229.

[chap 3] Rhee M.J. Schneider R.F. and Weidman D.J. (1987). "*Simple time-resolving Thomson spectrometer*". Rev. Sci. Instrum. **58**(2), pp 240.

[chap 3] Riemann K-U. (1991). "*The Bohm criterion and sheath formation*". J. Phys. D: Appl. Phys. **24**, pp 493.

[chap 3] Rocca J.J. Shlyaptsev V. Tomasel F.G. Cortazar O.D. Hartshorn D. Chilla J.L.A. (1994). "*Demonstration of a Discharge Pumped Table-Top Soft-X-Ray Laser*". Phys. Rev. Lett. **73**(16), pp 2192.

[chap 3] Rumsby P.T. and Paul J.W.M. (1974). "*Temperature and density of an expanding laser produced plasma*". Plasma Physics **16**, pp 247.

[chap 3] Ryutov D.D. Derzon M.S. and Matzen M.K. (2000). "*The physics of fast Z pinches*". Rev. Mod. Phys. **72**(1) pp 167.

[chap 3] Segall S.B. and Koopman D.W. (1973). "*Applications of cylindrical Langmuir probes to streaming plasma diagnostics*". Phys. Fluids **16**(7), pp 1149.

[chap 3] Siegmund O.H.W. (2000). "*Amplifying and position sensitive detectors*". In "*Vacuum Ultraviolet Spectroscopy*". Eds. J.A.R. Samson and D.L. Ederer. (Academic Press, San Diego, London).

[chap 3] Sopkin Y.V. Dorokhin L.A. Koshelev K.N. and Sidelnikov Y.V. (1991). "*Dynamics of sausage instabilities of a gas-puff Z-pinch*". Phys. Lett. A **152**(3,4), pp 215.

[chap 3] Spitzer L. (1962). "*Physics of fully ionised gases*". (Wiley Interscience, New York).

[chap 3] Stevefelt J. & Collins C.B. (1991). "*Modelling of a laser plasma source of amorphic diamond*". J. Phys. D: Appl. Phys. **24**, pp 2149.

[chap 3] Thomson J.J. (1913). "*Rays of positive electricity*". Proc. Royal Soc. **A89**, pp 1.

[chap 3] Voronov G.S. and Chernyshev L.E. (1974). "*Ion composition of an expanding multiply charged laser plasma*". Sov. Phys. Tech. Phys. **18**(7), pp 940.

[chap 3] Wiza J.L. (1979). "*Microchannel plate detectors*". Nucl. Instrum. and Meth. **162**, pp 587.

[chap 3] Wood R.F. Chen K.R. Leboeuf J.N. Puretzky A.A. and Geohegan D.B. (1997). "*Dynamics of Plume Propagation and Splitting during Pulsed Laser Ablation*". Phys. Rev. Lett. **79**(8), pp 1571.

[chap 3] Zel'dovich Y.B. & Raizer Y.P. (1966). "*Physics of Shock Waves and High-Temperature Hydrodynamic Phenomena*". Eds. W.D. Hayes and R.F. Probstein. (Academic Press, London).

CHAPTER 4

Soft X-ray investigations of pulsed transient plasma sources

4.1 Soft X-ray spectroscopy experiment

In Elton [Elton 1990] the soft X-ray region, or sometimes the extreme ultraviolet (EUV), is defined as covering the wavelength region from 0.2 – 30 nm. This part of the spectrum has received much interest over the past few years as explained also in the introduction to Chapter 3. The source of much of this interest comes from the semiconductor industry, where there is a wish to produce ever smaller gate sizes in computer processors. Here the short wavelengths of the soft X-rays for a lithography process is one of the solutions suggested for the future - provided several other technical hurdles can be overcome. Both of the books [Attwood 1999] and [Turcu & Dance1999] provide thorough reviews of this topic.

Spectroscopy in the soft X-ray region poses some extra difficulties when compared to that of visible spectroscopy. First of all, there is the need to have the spectrometer evacuated as the short wavelengths are readily absorbed in the atmosphere. Also for dispersing the radiation it is necessary to employ gratings at grazing incidence since no material is available for use as a prism at these short wavelengths. With the use of gratings comes the possible complication of having overlapping orders in the same region of the spectrum. And at grazing incidence there can be severe astigmatism problems to be corrected for [Elton 1990].

4.1.1 The GISVUV-spectrometer

The spectroscopic measurements of the microcapillary plasma source was undertaken at the *Laboratoire de Physique et Technologie des Plasmas* (LPTP), Ecole Polytechnique, Palaiseau in France. The spectrometer there is manufactured at the *Institute of Spectroscopy*, Troitsk, Russia. It is a highly compact, 1-m grazing incident, off-Rowland circle spectrometer, in short GISVUV. According to the specifications the grazing angle is 4°. Figure 4.1 depicts the layout of the spectrometer.

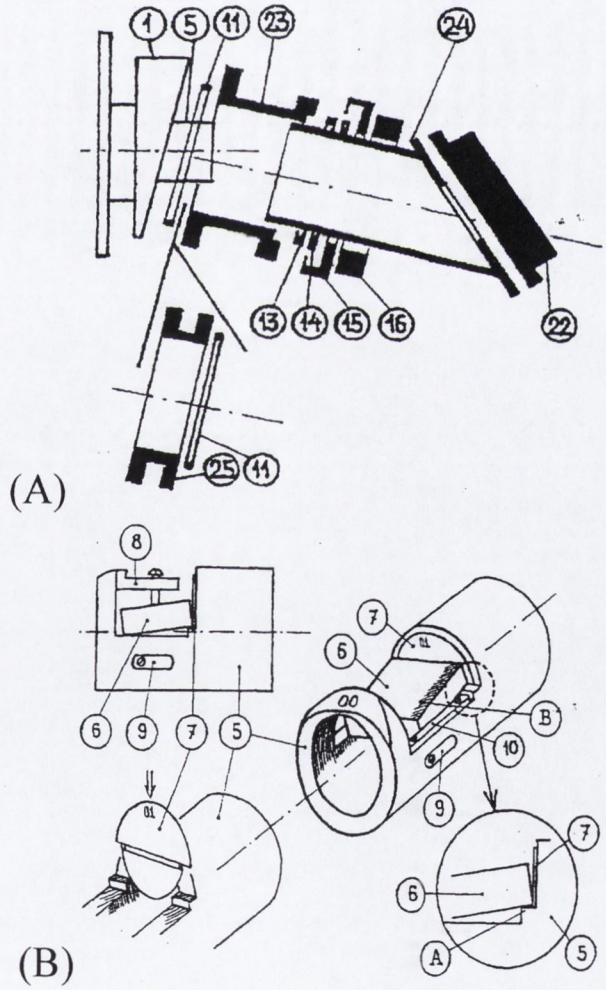

Figure 4.1: (A) Spectrograph. (B) Grating holder. 1: Spectrometer main body. 5: Grating holder. 6: Grating. 7: Diaphragm. 8: Angle unit with nylon screw. 9: Locking unit. 10: Guide plate. 11: O-ring. 13: Vacuum gasket. 14: Brass ring. 15: Lock nut. 16: Clamp. 22:Gated intensified microchannel plate - detector. 24: Extension tube. 25: Auxiliary body. (Copied from the spectrometer manual).

The theory of grating based spectrometers and monochromators is well described and the basic formulas are deduced in [Thorne *et al.* 1999] and [Padmore *et al.* 2000]. In the *Rowland* configuration the concave grating (radius of curvature R) and the entrance slit both lie on a circle of diameter R, as shown in Figure 4.2. In this geometry the spectrum lines are in focus on the circle, and the formula for the dispersion is:

$$d(\sin\alpha + \sin\beta) = m\lambda \qquad (4.1).$$

Here d is the distance between rulings, m an integer, α and β the incident and diffracted angles respectively and λ the wavelength. The GISVUV spectrometer used in this thesis is used in an off-Rowland configuration, meaning the detector plane is cutting the Rowland circle. This makes it slightly more complicated to determine the linear dispersion

$$\frac{dx}{d\lambda} \quad \text{mm nm}^{-1} \qquad (4.2)$$

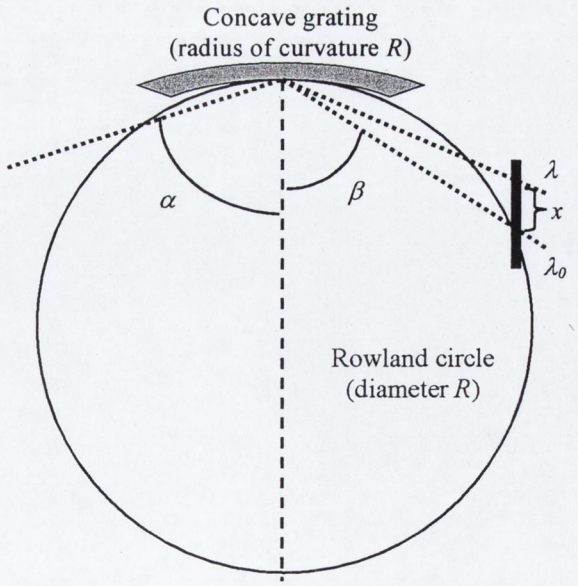

Figure 4.2: Schematic representation of the Rowland circle. The detector plane of the GISVUV spectrometer is off the Rowland circle (indicated by the fat black line) hence only one wavelength is in focus for a given arm distance.

The slit width of the spectrometer is about $w = 75$ μm [Krisch 2000]. The slit limited resolving power, R_{slit} ($= \lambda/\Delta\lambda$), is degraded compared to the diffraction limited resolving power, R_d, by the ratio of the diffraction width w_0 to the slit width [Thorne *et al.* 1999 pp 284].

$$R_{slit} = \frac{w_0}{w} R_d \tag{4.3}$$

For a concave grating $R_d = Wm/d$ where W is the grating width. The diffraction width for the concave grating can be written $w_0 = R\lambda/(W\cos\beta)$. We note that $\cos\beta$ is close to 1 hence we have as a lower estimate that $R_{slit} \sim R\lambda m/(wd)$. For a 600 line/mm ruled grating with a 1 m radius of curvature R the resolving power from this expression is ~ 80 for a wavelength of 10 nm and in first order $m = 1$.

The GISVUV spectrometer is equipped with a gold-coated grating the efficiency of which has not been measured. According to [Thorne *et al.* 1999] the reflectivity of Au-coated gratings below 100 nm is less than about 20%.

The gated intensified microchannel plate (MCP) detector employed on the spectrometer (22 on Figure 4.1) can be used for time resolved spectroscopy. The layout of the gating electrodes is different from the device described in section 3.4.4. The basic properties of the MCP for detecting radiation is found in [Wiza 1979] and [Siegmund 2000]. The quantum efficiency of MCPs to radiation in the soft X ray region is usually above 20% and depends on if they are coated or not, Figure 4.3 shows an example. The MCP used with the GISVUV in the experiments reported here was used in several X-ray detecting measurements before [Dumitrescu-Zoita 1996]. A special multi-frame design is employed for this detector. It has 4 lines of gold of approximately 1 cm width deposited as thin strips on the microchannel plate.

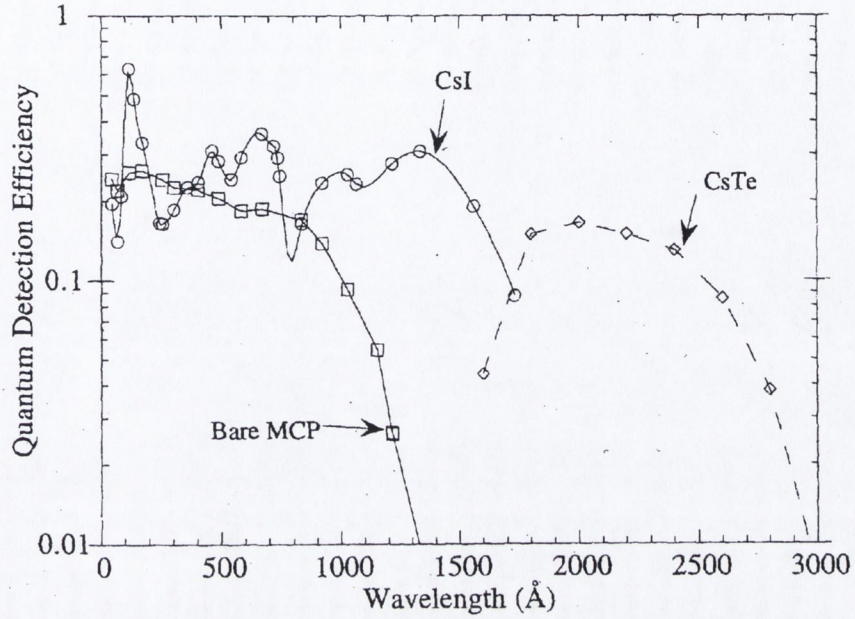

Figure 4.3: Quantum detection efficiency of a bare and coated microchannel plates [Siegmund 2000].

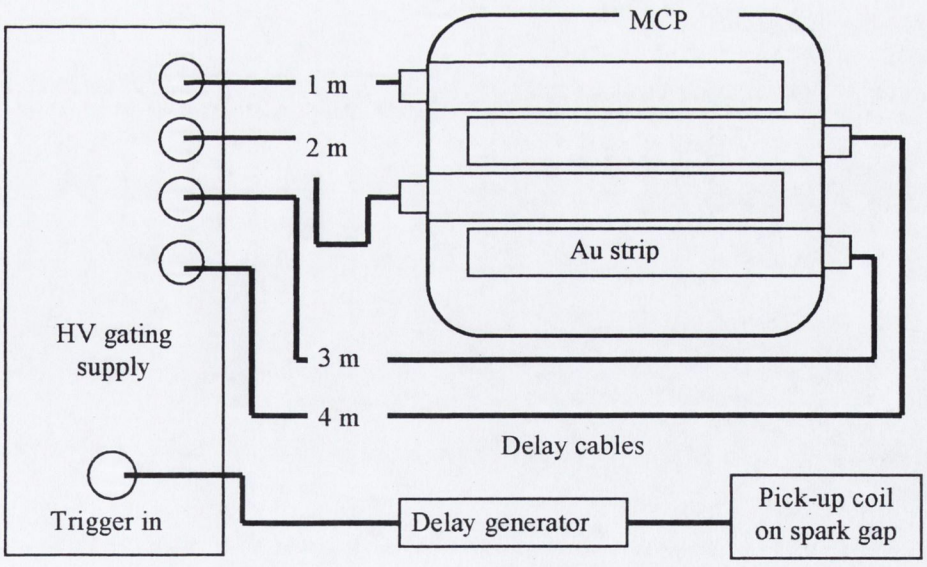

Figure 4.4: Multi-frame MCP setup for time resolved spectroscopy.

These strips define the active detection region while at the same time act as transmission lines. This last point allows short high voltage pulses to be applied when gating the detector and hence gives the high temporal resolution in the experiment, see also [Kilkenny *et al.* 1988]. In the experiments reported in this chapter the temporal resolution is ~5 ns as measured from the full width half maximum (FWHM) of the gating pulse. All the gold strips are gated from the same high-voltage (HV) gating pulse-generator (also used for the Thomson parabola analyser), but can be delayed with respect to each other by using various lengths of transmission cable. A pick-up coil under the spark gap is used to trigger a delay generator that in turn triggers the HV gating supply that activates the MCP, see Figure 4.4. No direct radiation can pass through the microchannel plate so on the photographic film, used to photograph the output image generated by the phosphor, only the strips displaying the spectrum at various times are present.

4.1.2. HP5-Plus black and white film

We use photographic film to record the spectra obtained with the GISVUV spectrometer. The spectra presented in this thesis are recorded on HP5-Plus black and white film from Ilford. We use the roll-film, length 120 (19 pictures). Detailed information on this film is available online [Ilford 2000]. Below in Figure 4.5 the characteristic curve of film density *vs.* relative log exposure is reproduced. Over the straight-line part of the characteristic the film density, D, is related to the exposure, E, that the film is subjected to by the relation:

$$D = \gamma \log \frac{E}{E_0} \qquad (4.4).$$

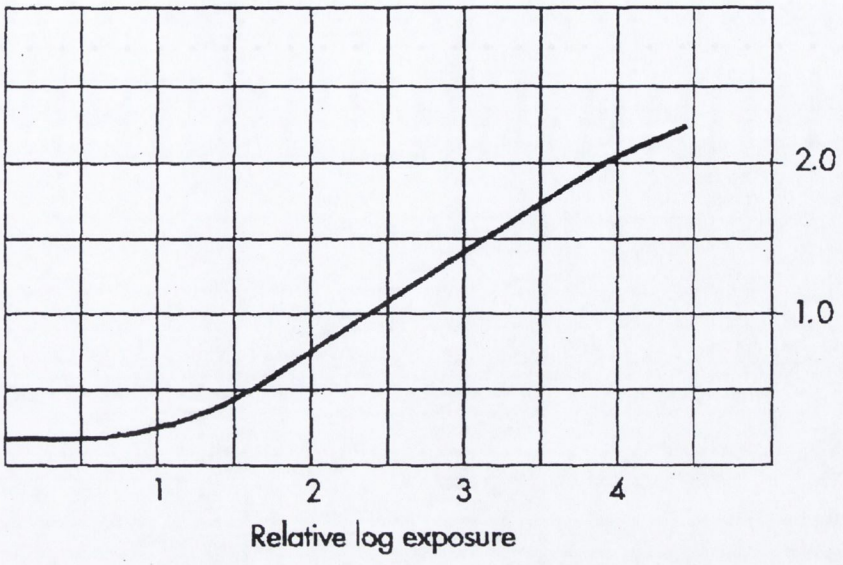

Figure 4.5: Characteristic curve of HP5 Plus. Abscissa: film density [Ilford 2000].

Here E_0 is the exposure where the density would be 0 if the straight line fit could be applied to the whole characteristic. The slope of the curve is termed γ. From Figure 4.5 it follows that $\gamma \sim 0.65$. Further, the density is related as well to the transmission T, which is measured on the developed film:

$$D = -\log_{10} T \tag{4.5}.$$

To analyse the spectrum the film is scanned using a commercial scanner (Agfa, Arcus II). The distance scale, x (see Figure 4.2), on the film is calculated from the line density (2400 ppi) used when scanning. Each pixel in the scan is assigned a value in between {0...65535} with 0 corresponding to no transmission. The transmission, T, is calculated from this number and it follows from (4.4) and (4.5) that the relative exposure on the film is proportional to:

$$E \propto \left(\frac{1}{T}\right)^{1/\gamma} \tag{4.6}.$$

The exposure is related to the incident photon flux on the MCP. In order to estimate the relative no of photons hitting the MCP several assumptions are made. The first is that the quantum detection efficiency is constant over the limited spectral region we observe in the spectrum, usually 10 - 40 nm. This is a good assumption for a bare MCP (Figure 4.3). Further, we can write the power on the entrance slit in a wavelength interval $\delta\lambda$ as: $I_\lambda \times \delta\lambda \times S \times (L \times w)/R_1^2$ were I_λ is the emitted spectral intensity (J cm^{-2} s^{-1} m^{-1} Ω^{-1}), S the area of the plasma, L and w the dimensions of the slit and R_1 the distance from the plasma to the slit. If R_2 is the total distance from the plasma to the MCP this power (in $\delta\lambda$) is spread out over an area $L \times (R_2/R_1) \times (dx/d\lambda)\delta\lambda$ on the detector. By dividing the power with the area we arrive at the *exposure on the MCP* in a time Δt: $E_{MCP} \sim I_\lambda \times (S \times w/R_1R_2) \times (d\lambda/dx)\Delta t$. The *exposure on the film* is given by this expression corrected for the sensitivity of the MCP which is proportional to the photon energy, hence $E_{film} \sim I_\lambda \times (S \times w/R_1R_2) \times (d\lambda/dx) \times (a/\lambda)\Delta t$ where a is constant. The dispersion relation, $dx/d\lambda$, presented later in this chapter, will vary by less than ~15% over a 10 nm spectral region, which is typically the region over which we make detailed line investigations, and we will hence disregard this factor in the analysis to come. When analysing a spectrum, the exposure Eq. (4.6) is multiplied by λ to be $\sim I_\lambda$.

Further, the spectra are compared to synthetic spectra from the FLY-code (see section 2.2) that plots the emission in I_ν ($ergs\ cm^{-2}\ s^{-1}\ Hz^{-1}\ \Omega^{1}$). These spectra are converted to I_λ by multiplying with λ^{-2} ($I_\nu \delta\nu = I_\nu \delta\lambda\ c/\lambda^2 = I_\lambda \delta\lambda$).

4.2 Calibration of the GISVUV spectrometer using a laser ablation plasma source

4.2.1. Introduction

The GISVUV spectrometer presented in Chapter 4.1 is used to record the spectra from the micro capillary discharge plasma source as well as other capillary plasma sources under operation in the FACADIX network. To help determine the dispersion relation (4.2) for the spectrometer it was used at Trinity College Dublin to record the emission spectra from laser ablation of various targets. The identification presented in this section is by Mr. Pierre Loiseleur from LPTP in Ecole Polytechnique.

Laser generated plasma soft X-ray sources have long been an intensely investigated subject [Turcu & Dance 1999]. Also, the spectra in the short wavelength region are extensively tabulated for most elements. One useful source of reference is the online "*Kelly's database*" [Kelly 2001] that is used throughout this thesis.

4.2.2. Experiment

In the experiment at TCD, time resolved spectroscopic measurements were done on ablation of single element targets of C, Al and Ti as well as multi-component targets of Alumina (Al_2O_3), Mylar or PTFE (Polytetrafluoroethylene or Teflon®). The two last targets are of interest to compare with the spectra from the microcapillary discharge source where the dielectric is either Mylar or PVDF (Polyvinylidenefluoride). We did not have PVDF available at the time of the experiment but PTFE was used as a substitute since, like PVDF, it contains fluorine and carbon.

Figure 4.6 is a sketch of the setup of the laser ablation experiment. The Nd:YAG laser ($\lambda_l = 1.06$ mm, $\tau_{pulse} \sim 6$ ns) is focused on a plane target at an angle of 45° to the target normal using a $f = 30$ cm plano-convex lens. The peak intensity is varied in the experiments in between $I_p = 1.1\times10^9 - 5.5\times10^9$ W cm^{-2} on the target. The chamber with the target and the spectrometer is evacuated to $\sim 5\times10^{-5}$ mbar (5 mPa).

An electrostatic probe held at a negative potential of –30 V is used to monitor the outflow of ions perpendicular to the target. The projected area of the cylindrical probe tip perpendicular to the flow measures $A = 4\times0.5$ mm^2 with the probe to target distance being $d_{probe} = 4.5$ cm. Initially the position of the focusing lens is varied while observing the recorded ion time-of-flight (TOF) distribution until the ion energy is maximised at which position the lens is fixed.

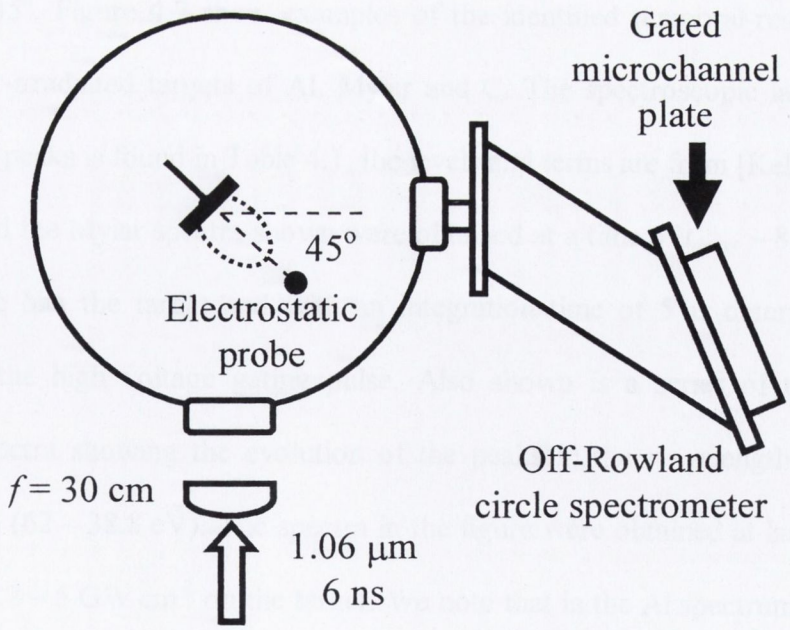

Figure 4.6: Laser ablation setup for time resolved soft X-ray spectroscopy.

A photodiode (BPX65, Si) placed outside the chamber but pointing at the target detects the unfiltered emission. In the figures below, zero time refers to a time on the leading edge of the laser pulse, when the plasma emission is initiated, and is determined from the rising edge on the photodiode signal.

The vacuum ultraviolet spectrograph uses a 600 line mm^{-1} gold-coated concave grating at a grazing incident angle ~ 4° to disperse the spectrum onto the detector plane. The detector is a gated multi-frame microchannel plate providing a time resolution of ~5 ns and with individual frames gated at a ~5 ns delay, see chapter 4.1.1. The spectrum was recorded on photographic film (HP5 Plus, roll film) and subsequently scanned.

4.2.3. Results

The spectrum is spatially integrated over the laser spot on the target viewed at an angle of 45°. Figure 4.7 show examples of the identified temporal-resolved spectra from laser-irradiated targets of Al, Mylar and C. The spectroscopic labelling of the numbered peaks is found in Table 4.1, the levels and terms are from [Kelly 2001].

The Al and the Mylar spectra shown were obtained at a time of t_{delay} ~ 8.5 ns after the laser pulse hits the target and with an integration time of 5 ns determined by the width of the high voltage gating pulse. Also shown is a series of time resolved carbon spectra showing the evolution of the peaks in the wavelength region from 20 –32 nm (62 – 38.8 eV). The spectra in the figure were obtained at laser intensities of about 4.2 – 5 GW cm^{-2} on the target. We note that in the Al spectrum a number of the lines are identified as belonging to oxygen ions. This oxygen is believed to be impurities forming on the Al surface.

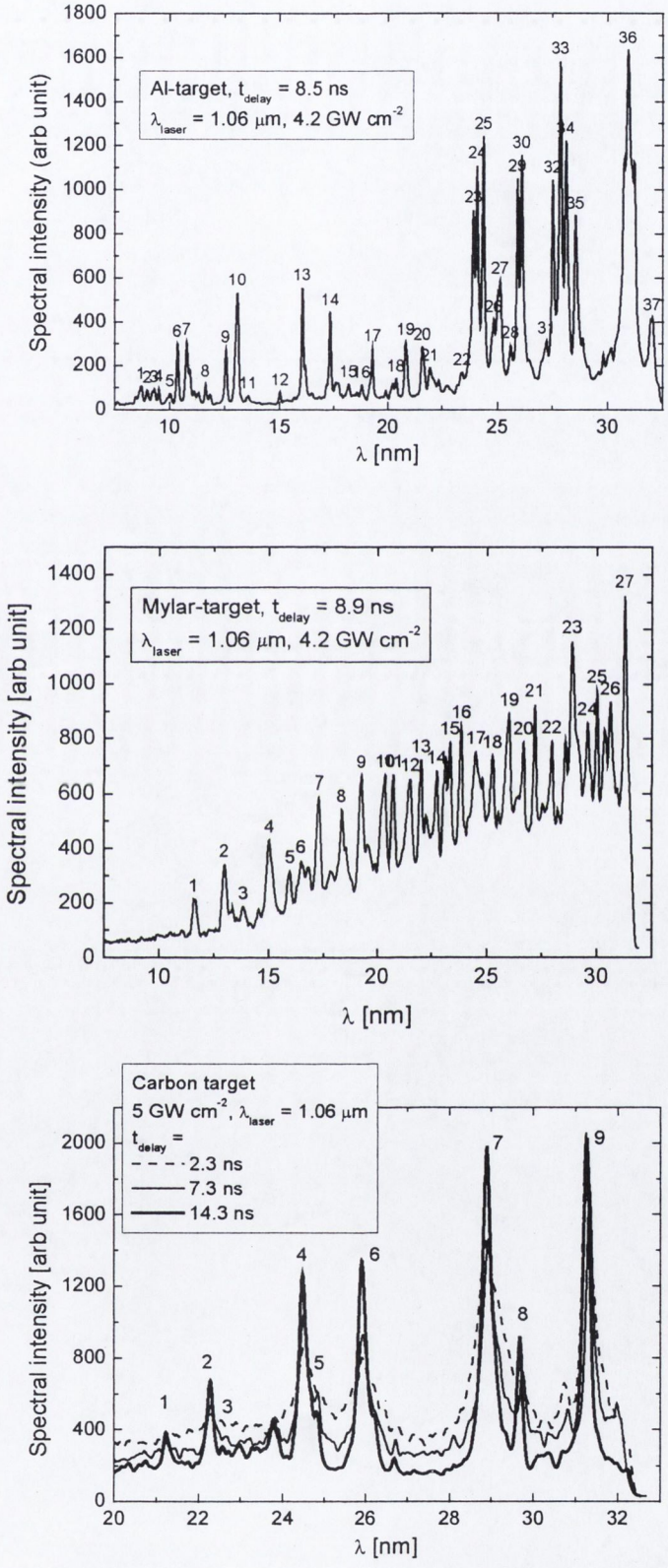

Figure 4.7: Soft X-ray spectra obtained with GISVUV spectrograph from laser produced plasma.

Table 4.1: Spectroscopic identification of spectra in Figure 4.7 [Loiseleur 2001].

Al-spectrum				
No.	λ [nm]	Ion	Transition	Term
1	8.76	Al +5	$2p^4$-$2p^3$3d	^{3}P-^{3}P
2	9.02	Al +5	$2p^4$-$2p^3$3d	^{1}D-^{1}F
3	9.29	Al +5	$2p^4$-$2p^3$3d	^{3}P-^{3}D
4	9.54	Al +5	$2p^4$-$2p^3$3d	^{1}S-^{3}D
5	10.09	Al +5	$2p^4$-$2p^3$3s	^{3}P-^{3}P
6	10.40	Al +5	$2p^4$-$2p^3$3s	^{3}P-^{3}D
7	10.76	Al +5	$2p^4$-$2p^3$3s	^{1}D-^{1}D
8	11.66	Al +3	$2p^6$-$2p^5$4d	^{1}S-1/2[3/2]^o
9	12.55	Al +4	$2p^5$-$2p^4$3s	^{2}P-^{2}D
10	13.08	Al +4	$2p^5$-$2p^4$3s	^{2}P-^{2}P
11	13.67	Al +4	2s$2p^6$-2s$2p^5$3s	^{2}S-^{2}P
12	15.01	O +5	2s-3p	^{2}S-^{2}P
13	16.01	Al +3	$2p^6$-$2p^5$3s	^{1}S-^{1}P
14	17.31	O +5	2p-3d	^{2}P-^{2}D
15	18.27	O +3	$2s^2$2p-2s2p3p	^{2}P-^{2}D
16	18.82	O +3	2s$2p^2$-$2p^2$3p	^{4}P-^{4}D
17	19.29	O +4	2s2p-2s3d	^{3}P-^{3}D
18	20.23	O +4	$2p^2$-2p3d	^{3}P-^{3}P
19	20.81	Al +6	$2s^2$$2p^3$-2s$2p^4$	^{4}S-^{2}P
20	21.52	O +4	2s2p-2s3s	^{1}P-^{3}S
21	22.04	O +4	2s2p-2s3d	^{1}P-^{1}D
22	23.36	O +3	2s$2p^2$-2s2p3d	^{4}P-^{4}D
23	23.90	Al +6	$2s^2$$2p^3$-2s$2p^4$	^{2}D-^{2}P
24	24.08	Al +6	$2s^2$$2p^3$-2s$2p^4$	^{2}D-^{2}P
25	24.38	Al +5	$2s^2$$2p^5$-2s$2p^5$	^{1}D-^{1}P
26	24.85	O +4	2s2p-2s3s	^{1}P-^{1}S
27	25.01	Al +7	$2s^2$$2p^2$-2s$2p^3$	^{3}P-^{3}S
28	25.60	?	?	?
29	25.90	Al +6	$2s^2$$2p^3$-2s$2p^4$	^{2}P-^{2}P
30	26.10	Al +6	$2s^2$$2p^3$-2s$2p^4$	^{2}P-^{2}P
31	27.21	O +3	2s$2p^2$-2s2p3s	^{4}P-^{4}P
32	27.53	Al +5	$2s^2$$2p^2$-2s$2p^5$	^{1}S-^{1}P
33	27.87	Al +4	$2s^2$$2p^5$-2s$2p^6$	^{2}P-^{2}S
34	28.14	Al +4	$2s^2$$2p^5$-2s$2p^6$	^{2}P-^{2}S
35	25.58	Al +6	2s$2p^4$-$2p^5$	^{2}D-^{2}P
36	30.91	Al +6	$2s^2$$2p^3$-2s$2p^4$	^{2}D-^{2}D
37	32.02	O +2	$2s^2$$2p^2$-$2s^2$2p3d	^{1}D-^{1}F

Mylar-spectrum

No.	λ [nm]	Ion	Transition	Term
1	11.58	O +5	2s-4p	^2S-^2P
2	12.99	O +5	2p-4d	^2P-^2D
3	13.81	O +4	2p-5d	^3P-^3D
4	15.01	O +5	2s-3p	^2S-^2P
5	15.94	O +4	$2p^2$-2p4d	^3P-^3D
6	16.47	O +4	2s2p-2p3p	^3P-^3P
7	17.30	O +5	2p-3d	^2P-^2D
8	18.41	O +5	2p-3s	^2P-^2S
9	19.28	O +4	2s2p-2s3d	^3P-^3D
10	20.39	O +4	$2p^2$-2p3d	^3P-^3D
11	20.78	O +4	$2p^2$-2p3d	^1D-^1F
12	21.52	O +4	2s2p-2s3s	^3P-^3S
13	22.04	O +4	2s2p-2s3d	^1P-^1D
14	22.75	O +4	2p2-2p3s	^3P-^3P
15	23.35	C +3	2p-8d	^2P-^2D
16	23.83	C +3	2p-7d	^2P-^2D
17	24.49	C +3	2s-4p	^2S-^2P
18	25.26	O +3	$2p^3$-$2p^2$3d	^2D-^2F
19	25.95 26.04	C +3 O +3	2p-5d 2s$2p^2$-2s2p3d	^2P-^2D ^2D-^2F
20	26.70	O +2	$2s^22p^2$-2s$2p^2$3p	^3P-^3D
21	27.21	O +3	2s$2p^2$-2s2p3s	^4P-^4P
22	27.99	O +3	2p-3s	^2P-^2S
23	28.92	C +3	2p-4d	^2P-^2D
24	29.56	O +2	2s$2p^3$-2s$2p^2$3d	^5S-^5D
25	29.99	O +3	2s$2p^2$-2s2p3d	^2P-^2P
26	30.57	O +2	$2p^2$-2p3d	^3P-^3D
27	31.25	C +3	2s-3p	^2S-^2P
28	38.4	C +3	$1s^2$2p-$1s^2$3d	^2P-^2D
29	25.85	O +4	2s2p-2s3s	^1P-^1S

(28 and 29 are referred to in section 4.3)

C-spectrum:

No.	λ [nm]	Ion	Transition	Term
1	21.24	C +3	2s-6p	^2S-^2P
2	22.28	C +3	2s-5p	^2S-^2P
3	22.72	C +4	2s-3p	^3S-^3P
4	24.49	C +3	2s-4p	^2S-^2P
5	24.87	C +4	2p-3d	^3P-^3D
6	25.95	C +3	2p-5d	^2P-^2D
7	28.92	C +3	2p-4d	^2P-^2D
8	29.69	C +3	2p-4s	^2P-^2S
9	31.25	C +3	2s-3p	^2S-^2P

4.2.4 Discussion

As mentioned in the introduction, laser generated plasma soft X-ray sources, is an active field of research. Let us here just point out to the reader the recent papers by [Atwee *et al.* 2001] and [Harilal *et al.* 2001] on time resolved laser generated plasma spectroscopic measurements. In the latter of these, XUV pinhole images were compared to an isothermal hydrodynamic expansion model [Singh & Narayan 1990]. Here we will discuss the *carbon* laser produced plasma and compare the plasma parameters to that obtained from the isentropic expansion model of chapter 2. As is clear from the spectra shown the Li-like ion, CIV, is the predominant ion radiating in the investigated wavelength region. A number of the lines observed in the time-resolved carbon spectra are included in Figure 4.8 along with their transition wavelengths and upper level energies. When we compare with Figure 2.6 in section 2.2 we see that the necessary condition on the density for LTE to be achieved is $n_e > 10^{25}$ m^{-3} (10^{19} cm^{-3}) for radiation with a wavelength of 20 nm. This is not unrealistic under the present experimental conditions, and we shall argue why.

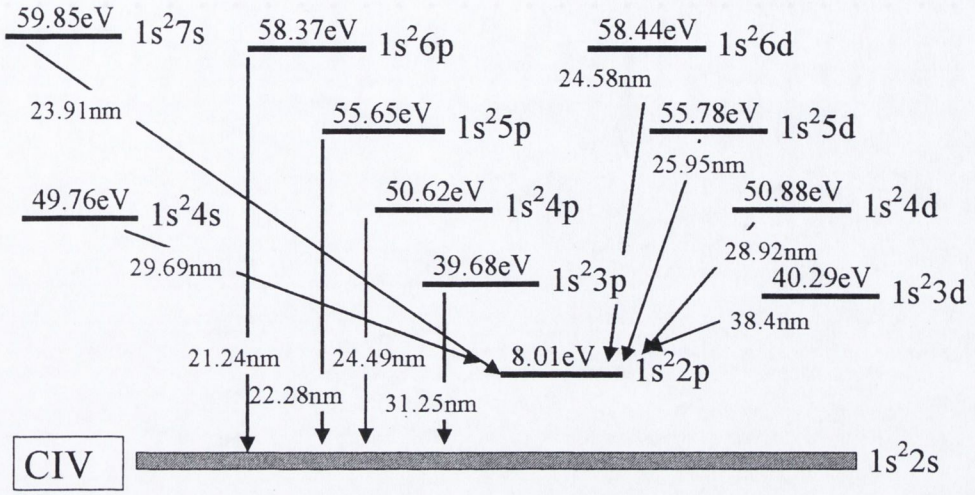

Figure 4.8: Carbon +3 level diagram of the transitions investigated in this work. The energy levels above the $1s^2 2s$ ground level are given in electron volts. The ionisation potential of CIV is 64.49 eV.

The analytical expression in [Phipps & Dreyfus 1993] for the electron density in a self-regulating ablation:

$$n_e = 3.59\times10^{11}\frac{m_{ion}^{5/16}}{Z^{1/8}(Z+1)^{9/16}}\frac{I_p^{1/4}}{\lambda_l^{3/4}\tau_{pulse}^{3/8}}\ [\mathrm{cm}^{-3}] \qquad (4.7),$$

where m_{ion} is in atomic-mass units u, λ_l is the laser wavelength in cm, τ_{pulse} the laser pulse width in seconds, yields a value of $\sim10^{20}$ cm^{-3} for our intensity $I_p \sim 5$ GW cm^{-2} and $Z = 3$. Even if the lines observed in Figure 4.7 are not fully in LTE with the ground state the upper levels can be in equilibrium with the continuum free electrons. Equation (2.31) also of section 2.2 can be used to estimate the limits for this, the result of which is presented in Figure 4.9. As we see the density requirement is relaxed so that for the p = 6 level in Li-like carbon the critical density is $< 10^{18}$ cm^{-3} over a wide temperature range.

We shall first present an analysis based on the assumption of LTE, which will be followed by a more detailed study using the FLY-code.

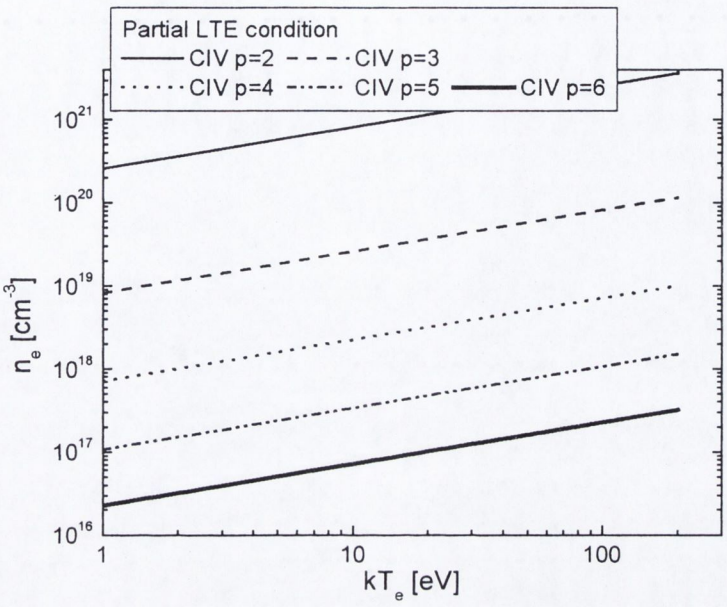

Figure 4.9: Partial LTE condition for electron density in CIV for principal quantum numbers p = 1-6.

To determine the temperature we use a Boltzman-plot in which $\log(I\lambda/gA_{ij})$ is plotted *vs.* the upper level energy E_{upper} and where the slope of the resulting straight line is $1/k_BT_e$ [Thorne et al. 1999]. As levels we include the CIV (6p→2s), (5p→2s), (5d→2p) and (4d→2p) lines all with upper levels higher that 50 eV (compare this to the ionisation energy of the CIV ground state $1s^22s$ of 64.5 eV). The transition probabilities A_{ij} are found at [NIST 1999]. The instrument broadening (4.3) is about ~20/80 = 0.25 nm. If we apply the equation (2.35) for the width of a Doppler broadened line, we find that $\Delta\lambda/\lambda \sim 1.5\times10^{-4}$, assuming k_BT_i~35 eV and $m_{ion} = 12$. The initial ion energy is deduced on the basis of the probe measurement. This gives a width smaller than the observed in Figure 4.7 and we therefore concluded that the lines are Stark broadened. As shown later in this section, a detailed optical thin collisional-radiative model (FLY-code) produced synthetic spectra that gave a good fit to the observed carbon spectrum. Taking this as

verification that the plasma can be treated as optically thin, we can proceed with the simple Boltzman-plot analysis outlined above. We note also the discussion in [Elton 1990, pp 39] [Atwee *et al.* 2000 and 2001], that in general the effective optical depth in expanding plasmas is lowered due to velocity and density gradients in the plume.

The electron temperatures deduced from the Boltzman plots are shown in Figure 4.10, as a function of delay time between triggering the MCP and the laser pulse on the target.

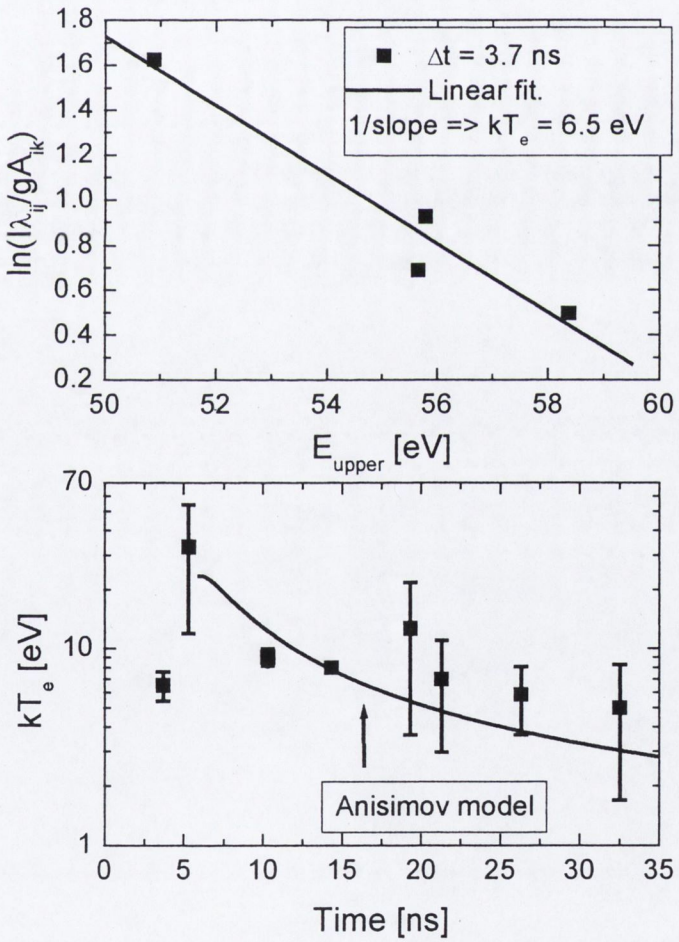

Figure 4.10: (TOP) Boltzman plot for determining $k_B T_e$ at $t_{delay} \sim 1.2$ ns. (BOTTOM) Plasma temperature of laser irradiated Carbon target at 5 GW cm^{-2}. Solid curve is predicted from the isentropic expansion model in section 2.1 and using the initial particle energy determined from electrostatic probe measurement.

The errors of the temperatures shown are calculated from the errors in the linear fit in the Boltzman-plot.

The electrostatic probe recordings are obtained at 4.5 cm distance from the target. The time-of-flight distribution of the recorded ion signal is modelled using the isentropic expansion model of Anisimov from section 2.1. We show this for two experiments on ablation of carbon at 5 GW cm^{-2} and 3 GW cm^{-2} respectively in Figure 4.11. In solving the expansion for the high intensity case we assume $X_0 = Y_0 = 0.05$ cm while Z_0 varies for the two intensities according to the initial sound velocities deduced from the probe signals, see equation (2.14) and (2.19).

At the highest intensity we find an expansion velocity of $\sim 1.8\times10^5$ m s^{-1} corresponding to an initial sound velocity $\sim 2.3\times10^4$ m s^{-1} for $\gamma = 1.26$. Using (2.15) we find the energy per particle

$$\varepsilon = \frac{c_{s,0}^2}{\gamma(\gamma-1)} m_{ion} \qquad (4.8).$$

With the numbers for the sound velocity from above, and using the carbon atomic mass $m_{ion} = 12$, we have that $\varepsilon \sim 200$ eV. Now solving for the expression for the temperature, Eq. (2.11), in the model with the assumption $(y,z) = (0,0)$, we can predict the temporal evolution of the temperature at the origin of the plume on the target. Note, that for this calculation we take specifically into account the contribution from the electrons by substituting $k_B T \rightarrow (1+\overline{Z})k_B T_e$ with $\overline{Z} = 3$. The result is depicted as the solid curve shown in the bottom graph of Figure 4.10. The starting time for the model has been set at 6 ns – at the end of the laser pulse where the plume is formed on the target. This calculation shows a satisfactory agreement taking into account the errors.

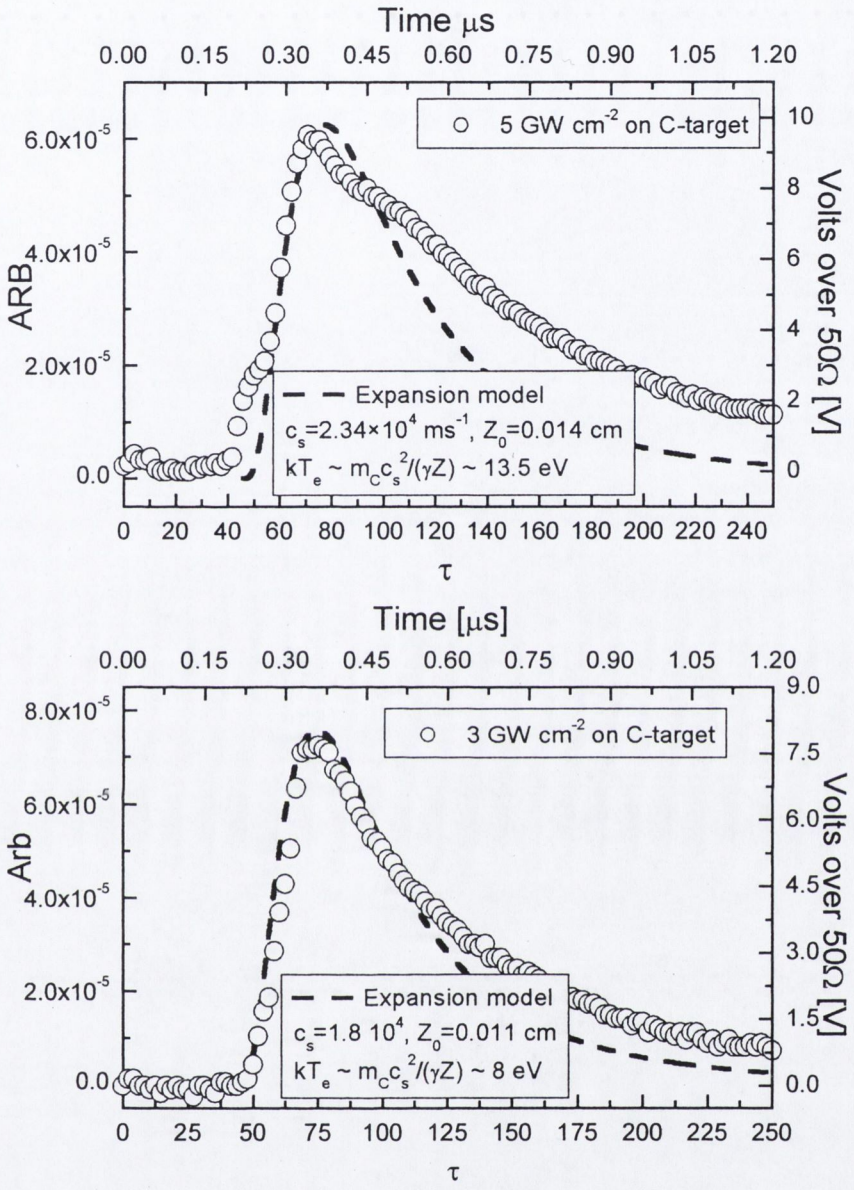

Figure 4.11: Experimental electrostatic probe recordings at 4.5 cm in laser irradiation of C-targets at 5 and 3 GW cm^{-2}. Probe area 2 mm^2. The expansion model from section 2.1 is run for the two cases as well with an initial thickness Z_0 depending on the measured expansion velocity.

The measured temperatures are in a reasonably range when we compare it to the time resolved measurements by [Atwee *et al.* 2000 and 20001] in a boron nitride plasma. Here temperatures of ~50 eV were measured but at a higher laser intensity. Also

good agreement is found with that calculated from the expression in [Phipps & Dreyfus 1993]

$$T_e = 2.98\times10^4 \frac{m_{ion}^{1/8} Z^{3/4}}{(Z+1)^{5/8}} \left(I_p \lambda_l \tau_{pulse}^{1/2}\right)^{1/2} \text{ [K]} \qquad (4.9).$$

The terms have the same meaning as in (4.7) and calculating the value of the temperature from it we arrive at ~23 eV.

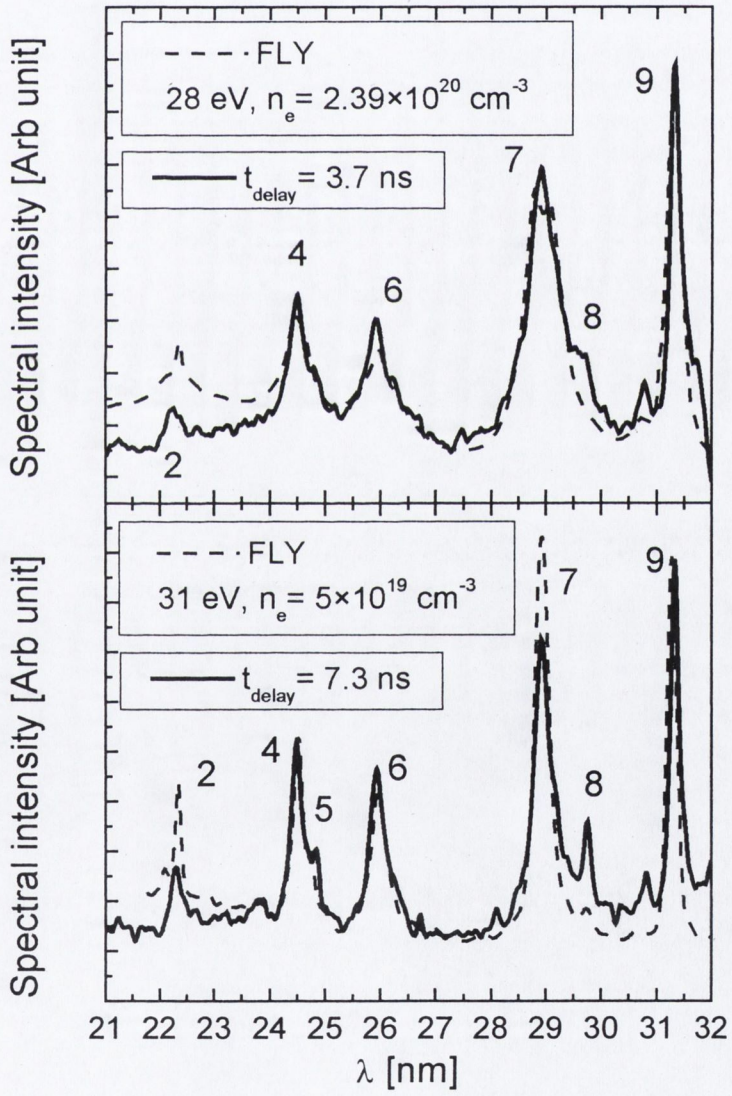

Figure 4.12: Comparison of time time-resolved spectrum (solid line) with FLY calculation (broken line) at two different delay times. The experimental gate-width is ~5 ns and the FLY spectra were calculated assuming an instrument resolution of 0.2 nm (FWHM). 2: CIV(2s-5p) 22.28 nm, 4: CIV(2s-4p) 24.49 nm, 5: CV(2p-3d) 24.87 nm, 6: CIV(2p-5d) 25.95 nm, 7: CIV(2p-4d) 28.92 nm, 8: CIV(2p-4s) 29.69 nm and 9: CIV(2s-3p) 31.25 nm.

Returning to the discussion of the electron density in the plume we proceed here to show the results of comparisons between synthetic spectra calculated using the FLY code (section 2.2) and the recorded spectra. The FLY model is an optical thin calculation of the emission taking into account collisional and radiative processes in the plasma. The comparison is done for the wavelength region 22 – 32 nm where the lines of CIV, as well as those for CV, have been identified. Figure 4.12 and 4.13 depicts the time-resolved spectra along with the FLY calculation.

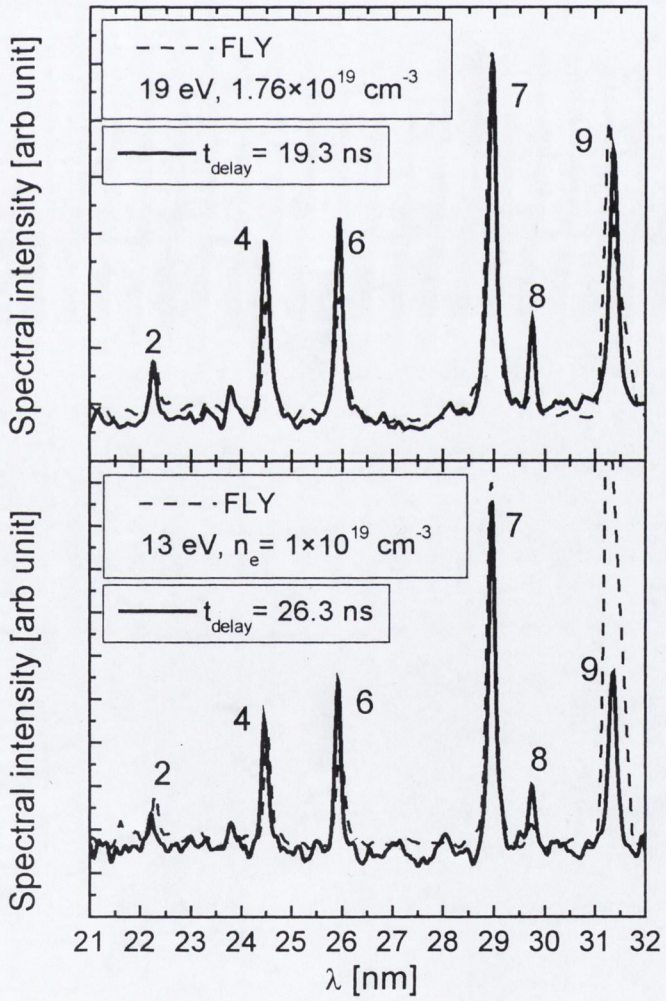

Figure 4.13: Comparison of time time-resolved spectrum (solid line) with FLY calculation (broken line) at two different delay times. The experimental gate-width is ~5 ns and the FLY spectra were calculated assuming an instrument resolution of 0.2 nm (FWHM). 2: CIV(2s-5p) 22.28 nm, 4: CIV(2s-4p) 24.49 nm, 5: CV(2p-3d) 24.87 nm, 6: CIV(2p-5d) 25.95 nm, 7: CIV(2p-4d) 28.92 nm, 8: CIV(2p-4s) 29.69 nm and 9: CIV(2s-3p) 31.25 nm.

In the calculation an instrument width of 0.2 nm was included, see discussion of the spectrometer resolution after Eq. (4.3). Good overall agreement is achieved over the spectral range, except at the resonance transition of CIV(2s-3p, 31.25 nm) at very late times where the measured intensity fall below that of the FLY synthetic spectrum. The resulting densities are seen to be broadly consistent with that assumed earlier (see Eq. (4.7)) varying from an initial maximum of ~2.4×10^{20} cm^{-3} to around 10^{19} cm^{-3} after 24 ns. These results are summarised in Figure 4.13, where both the temperature and electron density from the FLY calculation are shown along with the scaling calculated from the isentropic expansion model, Eqs. (2.11) and (2.8).

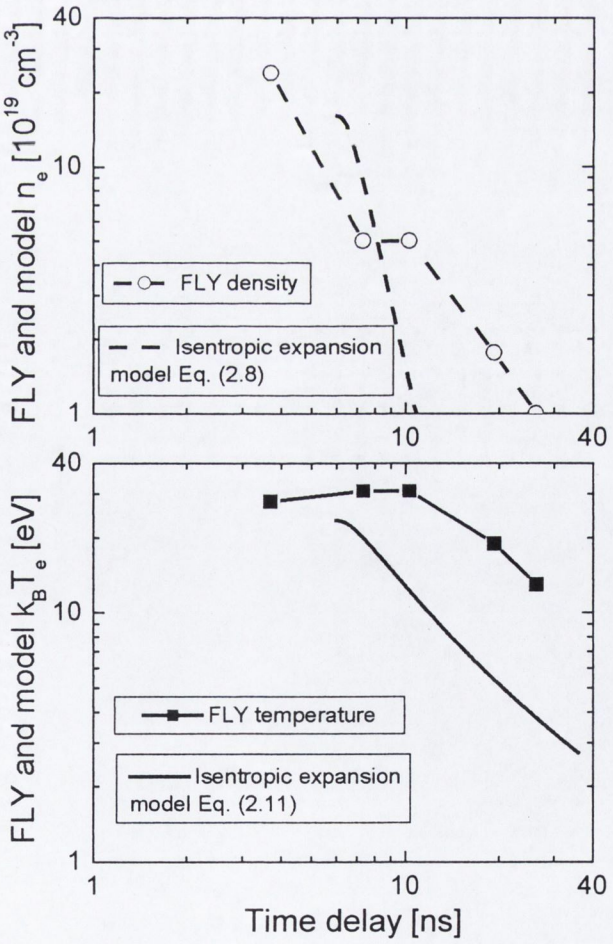

Figure 4.14: Temporal-resolved temperature and density from comparing the experimental spectra to synthetic FLY spectra. Also shown is the calculated variation of temperature and density in the isentropic expansion model at the position $(x,y,z) = (0,0,0)$, section 2.1.

The temperature scaling is the same as that shown in Figure 4.10 (BOTTOM). The plasma electron density is seen to qualitatively follow the sharp drop shown by the density in the isentropic model {~1/(XYZ)}. The initial particle density is taken to be ~10^{20} cm^{-3}. The temperature based on the isentropic model decreases more slowly in time than the density {~$1/(XYZ)^{(\gamma-1)}$} quantitatively confirmed by the spectroscopic temperature. The absolute value is lower than the spectroscopic temperature by a factor of about 2, which taking into account the somewhat arbitrary way the plasma state is taken into account in the model, can be said to be satisfactory.

4.2.5 Conclusion

Using the spectrometer in a simple laser ablation setup allowed us to compare the plasma parameters in the carbon plasma to that calculated on the basis of probe measurements, obtained when the plume expansion has become inertial. The time resolved measurements could be extended up to ~30 ns after the laser hits the target at which time the emission in the investigated soft X-ray range disappears. The hydrodynamic expansion model shows a good qualitatively agreement to the evolution of the spectroscopically deduced plasma parameters. With the identification of the lines from carbon and aluminium we can proceed to determine the dispersion curve for the spectrograph. This is shown in Figure 4.15. The physical setup of the spectrograph is the same in the experiments with the micro capillary discharge source as that reported above for the laser ablation experiments.

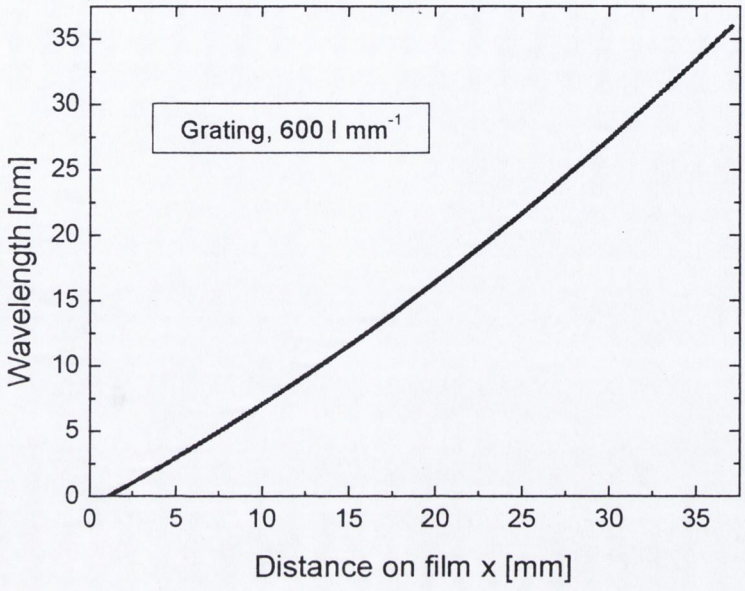

Figure 4.15: Dispersion curve for spectrograph as used in the laser ablation setup. The curve is a polynomial best fit to the identified lines: $\lambda = 0.00774x^2 + 0.70466x - 0.7567$.

4.3 Soft X-ray emission of the micro capillary discharge plasma

4.3.1 Introduction

The micro capillary discharge was presented in Chapter 3. A high voltage pulse is applied to the back electrode causing a dielectric surface self-breakdown through the sub-millimetre hole. Measurements presented in Chapter 3, of the ion outflow velocity and the electrical characterisation, indicate that a transient hot plasma with a temperature of about ~10 eV is generated in the initial breakdown phase. This section presents the details of measurements of the emission from the micro capillary undertaken as part of the work in the FACADIX network. Some earlier results have been presented at conferences as joint papers [Choi *et al.* 1999] [Engel *et al.* 1999] and [Hansen *et al.* 2001]. The spectra were recorded at LPTP in Ecole Polytechnique, France with the help of Dr. Ingo Krisch, Dr Axel Engel and Senior Researcher Dr. Jean Larour.

It is known that capillary discharges are intense sources of vacuum- and extreme ultraviolet radiation. Both, coherent "*X-ray lasers*" [Rocca 1999 and references therein] and incoherent radiation sources [Klostner & Silfvast 1998] [Juschkin *et al.* 1999] are reported in the literature. Typically in these devices a gas (such as Ar) at a pressure of ~10's Pa is used as the breakdown medium with maximum electron temperatures and densities reported to reach $T_e \sim$ 10-50 eV and $n_e \sim 10^{18}$-10^{19} cm^{-3}. We also mentioned in the previous section the interesting work that is taking place on laser-produced plasma soft X-ray sources. However the possibility of very

compact electrical discharge sources is a major drive for research into this type of devices.

4.3.2 Source size measurement from pinhole photography

We will start the characterisation of the emission from the high voltage micro capillary discharge plasma source by presenting an experiment of pinhole photography of the source.

In Figure 4.16 below, we present the geometry of a simple pinhole camera. The radiation source of diameter ϕ_s casts its shadow on the detector through a pinhole of diameter ϕ_a. The shadow of diameter $\phi_{s'}$ is surrounded by the penumbra of size $\phi'_{s'}$. The object and image distances are d and d' respectively, with the magnification being given by $M = d'/d$. It can be shown that

$$\phi'_{s'} = M\phi_s \quad \text{(A)} \qquad \phi_{s'} = (1+M)\phi_a - M\phi_s \quad \text{(B)} \tag{4.10}.$$

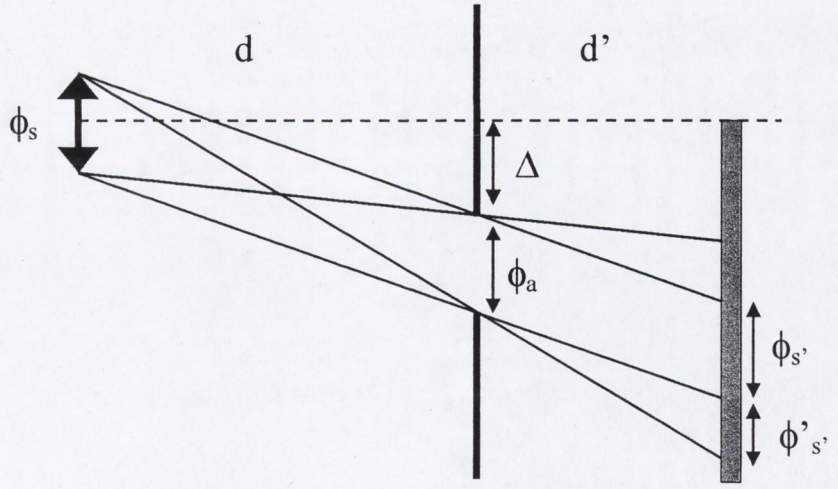

Figure 4.16: Sketch of pinhole camera geometry.

The detector used for the measurements is the same microchannel plate that was used with the Thomson parabola analyser, presented in section 3.4. The recording medium

is again HP5 Plus black and white film, the same as used for the Thomson parabola recordings. We note, that the MCP is blind to radiation with wavelength longer than ~124 nm [Sopkin *et al.* 1991]. This allows us to evaluate the degree to which diffraction will influence the results. The diffraction half-angle can be written:

$$\theta_d = \frac{1.22\lambda}{\phi_a} \qquad (4.11).$$

In the case of a pinhole of diameter $\phi_a = 100$ μm and a worse case scenario of a wavelength $\lambda = 124$ nm we find that $\theta_d = 1.5\times10^{-3}$. In Figure 4.17(A) we show a line scan of the image of the unfiltered radiation emitted by the microcapillary. The microchannel plate was gated on for ~5 ns starting at –2 ns before the voltage breakdown. Also shown in Figure 4.17(B) is the scan of an image of a pinhole that is covered by a 0.75 μm thick Al-film. Again the MCP was exposed for 5 ns during the breakdown of the voltage. Using an Al-filter limits the longest wavelength transmitted through the pinhole to ~20 nm, see Figure 4.18. For $\phi_a = 50$ μm and $\lambda = 20$ nm we find instead that $\theta_d = 4.8\times10^{-4}$. For an image distance of d'=37.55 cm we conclude that the diffracted spot is smaller than that measured which is a condition for deducing the size. Measuring the total spot ($\phi_{s'} + 2\phi'_{s'}$) we calculate from (4.10) a source size of roughly $\phi_s \sim 190$ μm for the un-filtered radiation while the shorter wavelength radiation yields a value of $\phi_s \sim 25$ μm. As the exact edge of the spot is somewhat undetermined these values should only be viewed as rough estimates with the accuracy no better than ~50%.

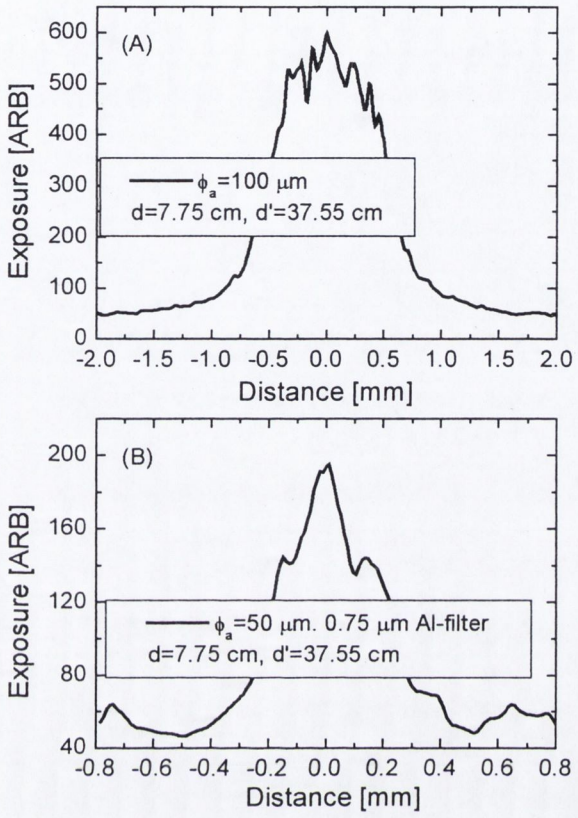

Figure 4.17: (A) Un-filtered pinhole image. (B) Pinhole image filtered through a 0.75 μm thick Al-filter. The back electrode is positive charged with V_p ~ 8.5 kV and discharge energy ~0.07 J.

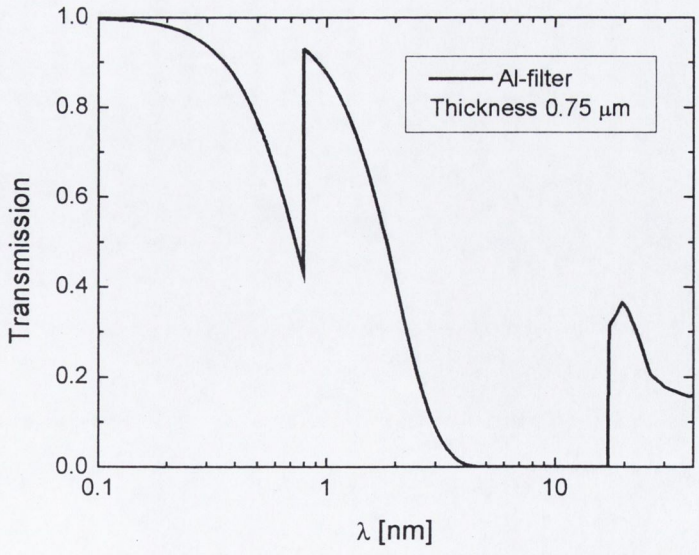

Figure 4.18: Transmission of Al-filter [CXRO].

The measurement indicates however, that the soft X-ray emitting region is confined to a small volume, probably of diameter less than the micro capillary, while the total emitting region is larger. Shifting the time-of-gating of the MCP reveals that already after 5-10 ns the transmission through the Al-filter becomes insufficient to detect.

4.3.3 Soft x-ray spectra from the micro capillary discharge plasma

The soft X-ray emission from the micro capillary discharge device is investigated using the GISVUV-spectrometer presented in section 4.1. The spectrum is dispersed using a 600 mm^{-1} gold grating at grazing incidence, identical to the setup used in the laser produced plasma experiment in the previous section. The spectrometer is mounted on the axis of the microcapillary and hence views the plasma end-on, Figure 4.19. To limit the number of ions entering the slit and possible damaging the grating the spectrometer has been placed some distance away. This however not only reduces the ion density but also the photon flux and thereby renders the detection of spectra more difficult.

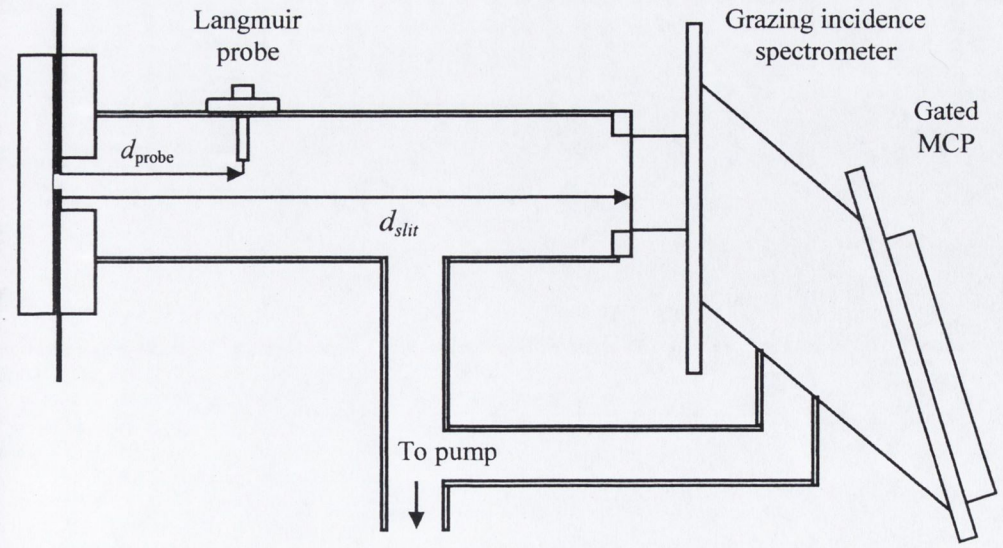

Figure 4.19: Micro capillary plasma spectroscopy setup, d_{probe} = 13 cm, d_{slit} = 42 cm.

The vacuum chamber is evacuated to a pressure of ~0.05 Pa (5×10^{-4} mbar) and the spectrograph is differential pumped to secure safe operation of the MCP. The MCP is gated on using a ~6.15 kV, 5 ns (FWHM) high-voltage pulse from the generator, see Figure 4.4.

Figure 4.20 below show the temporal development of the soft X-ray radiation emitted from a Mylar dielectric micro capillary discharge plasma. The lines are numbered using the numbers from Table 4.1 of the laser produced **Mylar** spectrum. The delay time, Δt_{delay}, is measured from the peak hold-on-voltage as usual, and the spectrum is integrated for a ~5 ns period *from the delay time onward.* We remind the reader that at the time of the peak hold-on-voltage the current has developed roughly by a ¼-period of the oscillation (see Figure 3.9). The spectrum is dominated by Li- and Be-like oxygen ions (O^{+5} and O^{+4}) and Li-like carbon (C^{+3}) ions. In this connection we note that the intense line at $\lambda \sim 17.3$ nm, assigned to O^{+5} (2p-3d), is so close to the resonance oxygen O^{+4} line ($\lambda \sim 17.22$ nm, 2s-3p) that we can not distinguish the two within the accuracy of the experiment. The spectra obtained were all for positive charging of the microcapillary which produces the least energetic plasma as we have seen in the previous chapter.

Combining the results from several series of shots like Figure 4.20, we have measured the dependence of the maximum radiant intensity on the input energy ($\frac{1}{2}CV_p^2$), for the Li-like carbon and oxygen resonance lines (2s-3p). The results from the measurements obtained at a time delay of –4 ns and 1 ns after the breakdown are shown in Figure 4.21.

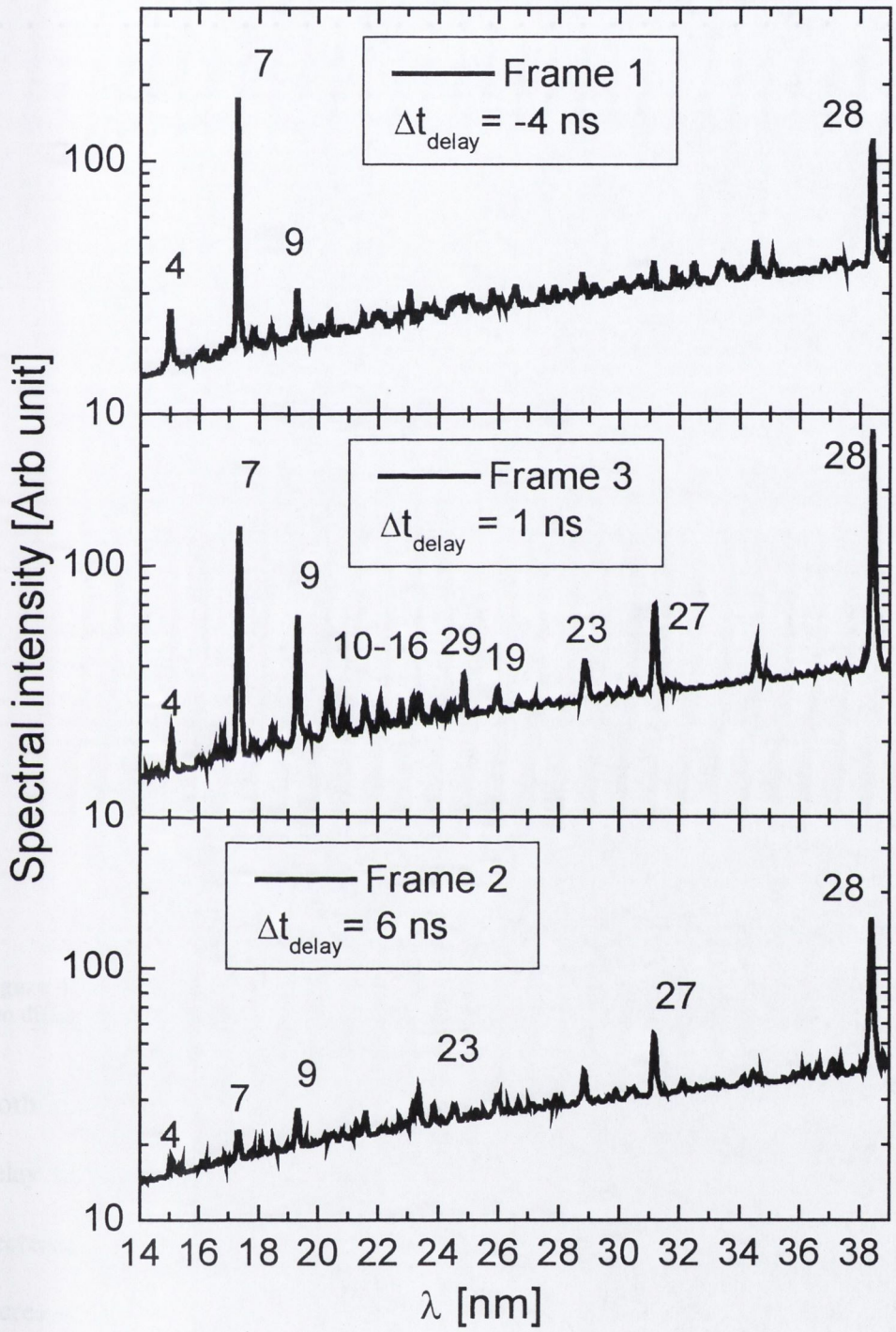

Figure 4.20: Time-resolved soft X-ray spectra of microcapillary discharge plasma. Positive charging of a Mylar-dielectric cell with a discharge energy 0.04 J. The numbers refer to the **Mylar** identification in Table 4.1. The feature at ~34.6 nm is believed to be the second-order line of the intense O+5 line (7).

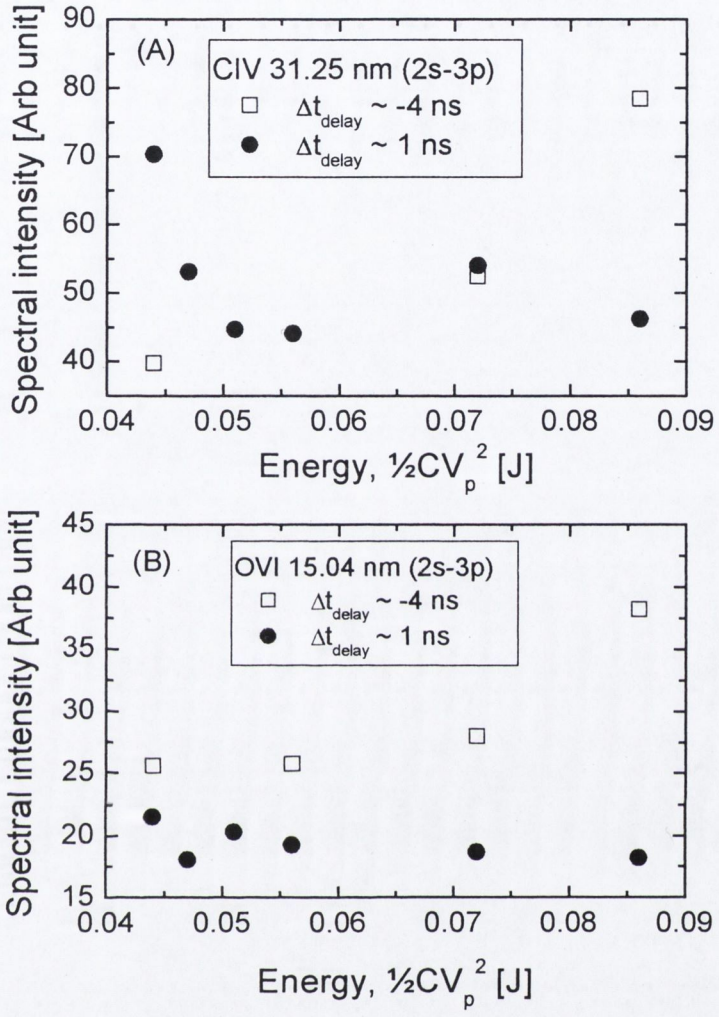

Figure 4.21: Maximum recorded intensity for Li-like resonance lines in Carbon and Oxygen ions at two different delay times as function of input energy.

Both ions show an increase in emission with an increased input energy at the earliest delay time (at breakdown) while at later delay times the output is constant or even decreasing with higher input energy. We conclude that the initial burst of radiation increases for a higher input energy, but as the discharge evolves the plasma radiates less on the resonance lines monitored above for an increased input energy. A collection of the time-dependence of the emission is depicted in Figure 4.22 for an electrical input energy of ~0.05 J and 0.09 J.

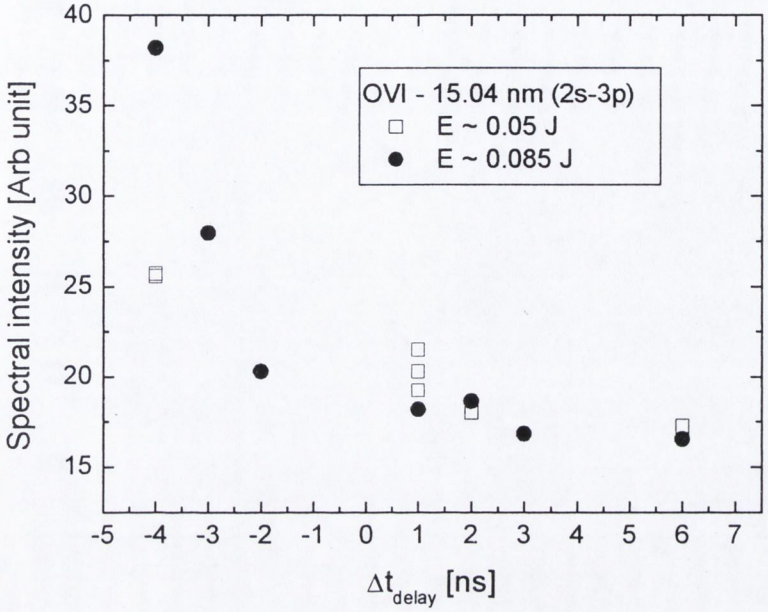

Figure 4.22: Time resolved intensity registered for the Li-like O^{+5} line at λ = 15.04 nm. The MCP is gated on for a time of ~5 ns at the time Δt_{delay} from the peak hold-on-voltage.

4.3.4 Discussion and conclusions

The raw spectra of the microcapillary discharge plasma are much weaker than those recorded in the laser produced plasma experiments. A single frame, corresponding to the spectrum shown in frame 3 in Figure 4.20, is shown in Figure 4.23. The lines are mostly very thinned out, which makes it difficult to obtain information of the line profile. This has prevented detailed comparisons, like those achieved in the previous section on the laser produced plasma source, with the FLY-code.

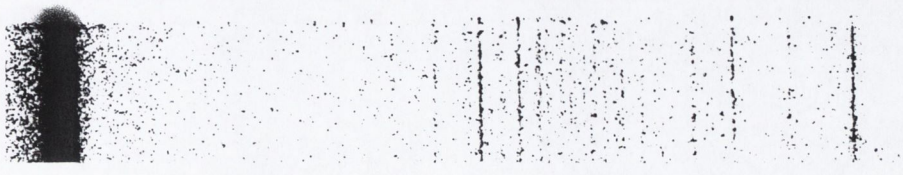

Figure 4.23: Mylar-dielectric microcapillary discharge spectrum (Frame 3 of Figure 4.20).

It was reported in Figure 3.17 that the expansion velocity of the plume front in a positive charged microcapillary is about 2×10^5 m s^{-1}. This is similar to the laser produced carbon plasma that was investigated in detail in section 4.2 and would imply a similar initial temperature of ~20 eV based on the expansion scaling. A rather high initial density (~10^{21} cm^{-3}) was inferred in section 3.3.2 on the basis of the expansion measurements. However, there is evidence from the pinhole measurements discussed above, that only a small part of the volume of the microcapillary plasma is hot enough to emit significantly in the soft x-ray region for the charging applied in these experiments. This observation along with the long distance from the source to the entrance slit helps to explain the low intensity.

Griem [Griem 1997, pp 288] discuss the possibility of temperature measurements from the intensity ratio of isoelectronic transitions of different elements. This reference discusses an example where it is found that the intensity ratio of transitions in Li-like vanadium and titanium ions is constant over a vide range of densities and for a given temperature. We have attempted a similar analysis, using the FLY suite to generate synthetic spectra for carbon and oxygen at identical values of temperature and density. From these spectra the ratio of peak intensities are calculated and plotted in Figure 4.24(A) for the OVI and CIV lines observed. We observe indeed that for a given temperature the ratio of oxygen to carbon peak intensities is roughly constant over many orders of magnitude of the density. This allows us to plot the peak intensity ratio against temperature and this is shown in Figure 4.24(B).

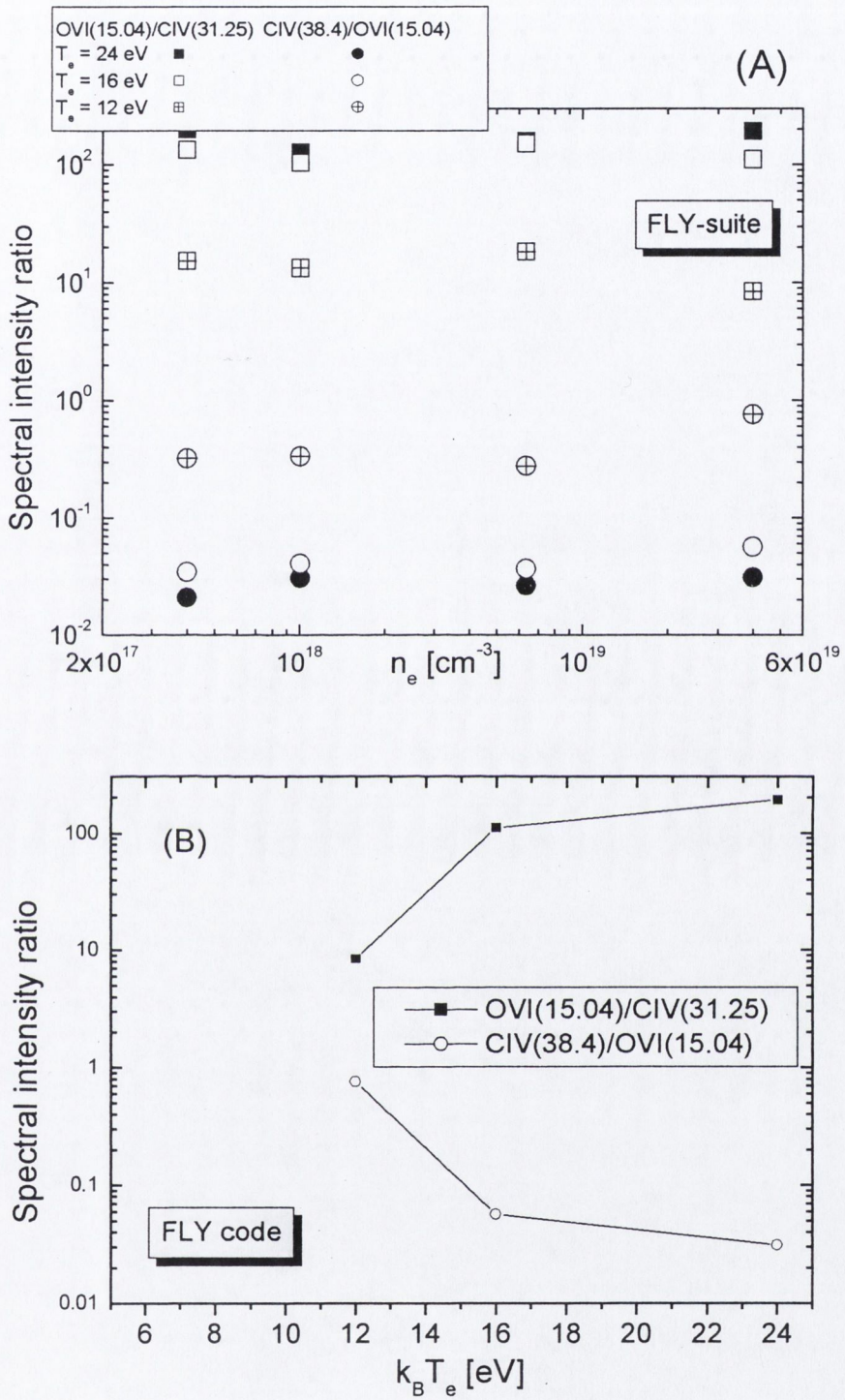

Figure 4.24: (A) Intensity ratio from FLY generated synthetic spectra. (B) Same data as in (A) but shown *vs.* temperature.

The experimental line ratio as a function of discharge energy and for two different delay times is shown in Figure 4.25. If we compare Figure 4.24(B) with the experimental ratio, we can put an upper limit on the temperature achieved here in the Mylar dielectric, positively charged, micro capillary discharge of ≤ 12 eV.

A more detailed treatment of the ionisation balance is not attempted here. [McWhirter 1965] states, that for a corona model, the atomic relaxation time is to within an order of magnitude $\tau \sim 10^{12}/n_e$, with n_e in cm^{-3} and τ in s. For electron densities below $\sim 10^{21}\ cm^{-3}$ (which is likely the case for the microcapillary experiments above) we observe that the plasma lifetime is less than the characteristic time which means that a time-dependent method should be used. The FLY calculations presented above are more elaborate than the corona-model. It is however a steady-state calculation also, limiting the applicability.

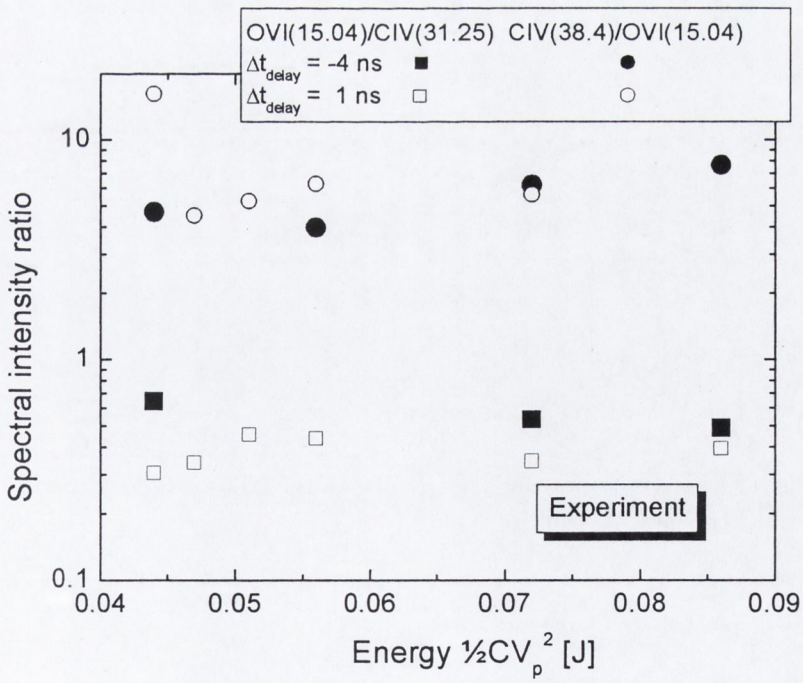

Figure 4.25: Experimental line ratio of isoelectronic ions.

4.4 Conclusion and outlook of spectroscopy measurements

The spectroscopic measurements of the laser produced plasma experiments were analysed using both the LTE approximation and the FLY-code. The results from the two methods were consistent, and the deduced plasma parameters were in accordance with analytical expressions covering high intensity (>1 GW cm^{-2}) laser produced plasma interactions [Phipps & Dreyfus 1993]. As an extra result, we showed how the isentropic expansion model from Chapter 2, with a few modifications to take account for the plasma parameters, could be used to predict the evolution of the temperature and density, based on probe recordings in a region where the expansion has become inertial.

Using the information gathered from the laser produced plasma experiments the spectra from the microcapillary source could be identified. The spectra were obtained for a positive charging of the back plate, the electrical energy input being about 50 mJ. This is significantly lower than the about 250 mJ of laser pulse energy in the laser ablation experiments and is an important contribution, to the less intense spectra observed in the microcapillary experiment. The temperature at about 10 eV was estimated to be lower than in the carbon laser produced plasma. It has already been pointed out in section 3.3 that a change to negative charging of the microcapillary could lead to a favourable scaling to higher plasma electron temperatures.

One drawback of previous work on micro scale plasma is that the plasma is usually not stable [Koshelev and Pereira (1991)]. The microcapillary discharge is a small, scaled device that can help overcome this problem by fixing the position of the plasma. Further, the study by [Koshelev & Kunze 1997] on neck formation in discharges shows the possible application of these micro-plasma sources. The neck

forms as a magnetohydrodynamic instability in the discharge column in pinch plasmas, where they can act as centres of population inversion in the VUV/Soft X-ray region. One of the shortcomings of the present microcapillary setup is the limited number of shots that can be made before the thin sheet of dielectric fails. To overcome this, we have purchased thin (100 μm) ceramic discs with drilled holes of diameter 100 μm, intended for use as microcapillary in the discharge setup. With more shots from one discharge cell it can also be possible to think about integrating the recorded spectra over several shots to obtain a higher exposure on the film.

References

[chap 4] Attwood D. (2000). "*Soft X-rays and extreme ultraviolet radiation: principles and applications*". (Cambridge University Press).

[chap 4] Atwee T, Aschke L. and Kunze H-J. (2000). "*Investigations of laser-produced plasmas from boron nitride targets*". J. Phys. D: Appl. Phys. **33**, pp 2263.

[chap 4] Atwee T. Harilal S.S. and Kunze H-J. (2001). "*XUV spectroscopic studies of plasma plumes produced from boron, boron carbide and boron nitride targets by a laser*". J. Phys. D: Appl. Phys. **34**, pp 1213.

[chap 4] Choi P. Lunney J.G. Engel A. Dumitrescu C. Hansen T.N. Krisch I. Larour J. Rous J. (1999). "*A 10^13 A/s High Energy Density Micro Discharge Radiation Source*". In "*12th IEEE Int. Pulsed Power Conference, Monterey June 1999*". Eds. C. Stallings and H. Kirbie. (IEEE, Piscataway, NJ, USA, 1999 Vol **1**, pp 287).

[chap 4] CXRO. "*Centre for X-ray Optics*". http://cindy.lbl.gov/

[chap 4] Dumetrescu-Zoita C. (1996). "X-ray emission from hot, dense, magnetized plasmas". These Le Grade de Doctor en Sciences. Universite de Paris-Sud U.F.R. Scientific D'Orsay.

[chap 4] Elton R.C. (1990). "*X-ray lasers*". (Academic Press Inc).

[chap 4] Engel A. Hansen T.N. Choi P. Dumitrescu C. Lunney J.G. Krisch I. Larour J. Rous J. (1999). "*A High Brilliance VUV/Soft X-ray Microcapillary Radiation*

Source Powered by an 10^13 A/s Compact Driver". In "*International Symposium Plasma '99*". Eds. E. Infeld, H. Rothkaehl, M. Sadowski. (J. Tech. Phys. (Poland), Warszawa 1999, Vol. **40**(1), pp 497).

[chap 4] Griem H.R. (1997). "*Principles of plasma spectroscopy*". (Cambridge University Press).

[chap 4] Hansen T.N. Krisch I. Choi P. Larour J. Lunney J.G. Castro J. Engel A. Guilbert A. Rous J. (2001). "*Dynamcis of the EUV radiation in a fast micro-capillary plasma discharge source*". In "*X-ray lasers 2000. 7th International Conference on X-ray Lasers*". Eds. G. Jamelot, C. Möller, A. Klisnick. (Journal de Physique IV (Proceedings) 2001, Vol. **11**, Pr2-417).

[chap 4] Harilal S.S. Bindhu C.V. and Kunze H-J. (2001). "*Space and time-resolved soft x-ray emission from laser produced magnesium plasma*". J. Phys. D: Appl. Phys. **34**, pp 560.

[chap 4] Ilford (2000). "*Online technical information*". http://www.ilford.com/html/us_english/bw.html.

[chap 4] Juschkin L. Hildebrand A. and Kunze H-J. (1999). "*A capillary discharge as a pseudo-Planck radiator in the vacuum ultraviolet*". Plasma. Sources Sci. Technol. **8**, pp 370.

[chap 4] Kelly R.L. (2001). "*Kelly atomic line database*". http://cfa-www.harvard.edu/amdata/ampdata/kelly/kelly.html.

[chap 4] Kilkenny J.D. Bell P. Hanks R. Power G. Turner R.E. and Wiedwald J. (1988). "*High-speed gated x-ray imagers*". Rev. Sci. Instrum. **59**(8), pp 1793.

[chap 4] Klosner M.A. and Silfvast W.T. (1998). "*Intense xenon capillary discharge extreme-ultraviolet source in the 10-16-nm wavelength region*". Optics Lett. **23**(20), pp 1609.

[chap 4] Koshelev K.N. and Kunze H-J. (1997). "*Population inversion in a discharge plasma with neck-type instabilities*". Quantum Electronics **27**(2), pp 164.

[chap 3] Koshelev K.N. and Pereira N.R. (1991). "*Plasma points and radiative collapse in vacuum sparks*". **69**(10), pp R21.

[chap 4] Krisch I. (2000). At LPTP in France. *Private communication.*

[chap 4] Loiseleur P. (2001). At LPTP in France. *Private communication.*

[chap 2] McWhirter R.W.P. (1965). "*Spectral Intensities*". In "*Plasma diagnostics techniques*". Eds. R.H. Huddlestone and S.L. Leonard. (Academic Press, London).

[chap 4] NIST (1999). "*NIST Atomic Spectra Database*". http://physics.nist.gov/cgi-bin/AtData/main_asd.

[chap 4] Padmore H.A. Howels M.R. and McKinney W.R. (2000). "*Grazing-incident monochromators for third-generation synchrotron radiation sources*". In "*Vacuum Ultraviolet Spectroscopy*". Eds. J.A. Samson and D.L. Ederer. (Academic Press).

[chap 4] Phipps C.R. and Dreyfus R.W. (1993) "*The high laser irradiance regime*". In "*Laser Ionization Mass Analysis*". Eds. A. Vertes, R. Gijbels and F. Adams. Chemical Analysis Series vol **124**, pp 369. (John Wiley & Sons).

[chap 4] Rocca J.J. (1999). "*Table-top soft x-ray lasers*". Rev. Sci. Instrum. **70**(10), pp 3799.

[chap 4] Singh R.K. and Narayan J. (1990). "*Pulsed-laser evaporation technique for deposition of thin films: Physics and theoretical model*". Phys. Rev. B **41**(13), pp 8843.

[chap 4] Siegmund O.H.W. (2000). "*Amplifying and position sensitive detectors*". In "*Vacuum Ultraviolet Spectroscopy*". Eds. J.A. Samson and D.L. Ederer. (Academic Press).

[chap 3] Sopkin Y.V. Dorokhin L.A. Koshelev K.N. and Sidelnikov Y.V. (1991). "*Dynamics of sausage instabilities of a gas-puff Z-pinch*". Phys. Lett. A **152**(3,4), pp 215.

[chap 4] Thorne A. Litzen U. and Johansson S. (1999). "*Spectrophysics: Principles and Applications*". (Springer-Verlag, Berlin Heidelberg).

[chap 4] Turcu I.C.E. and Dance J.B. (1999). "*X-ray From Laser Plasmas: Generation and Applications*". (John Wiley & Sons Ltd).

CHAPTER 5

Plume expansion in pulsed laser ablation

5.1: Langmuir probe study of plasma expansion from a plane target

5.1.1 Overview

The micro capillary plasma discharge source was extensively discussed in the previous chapter. This is one of the topics on which Trinity College has been working in the FACADIX project. In the same project it was proposed to elaborate on existing "long" capillary, collision pumped, discharge schemes championed since the late 80's by Rocca at Colorado State Univiversity, US [Rocca 1999]. This type of source relies on the breakdown and on-axis plasma-column formation in a gas, such as Ar, but it was suggested under FACADIX, to work to modify this type of experiment, to be able to introduce other ions. These can be generated by laser ablation of e.g. a metal target. In the proposal the electrical stored energy in the capacitor is to be discharged through the capillary after the plasma has been injected. This can open the possibility of new transitions to be favourably populated and thereby for new laser wavelengths to be obtained. Laser ablation lends itself directly to this purpose since it has successfully been used to ablate a range of materials, see list in [Bäuerle 1995]. Some experiments on introducing a laser ablated metal target into a capillary discharge were undertaken in Chile at the group of Prof. M. Favre and reported at the 2000 APS conference [Wyndham *et al.* 2000].

5.1.2 Experiment

To study the expansion dynamics of a laser produced plasma, we have investigated the ablation from a plane target using Langmuir probes. In Chapter 2 we described the relative simple hydrodynamic expansion model of Anisimov and co-workers. This model is shown, through experiments described in this thesis, to predict, at least qualitatively, the plume expansion well under different irradiance parameters.

The results reported in this section illustrate the applicability of the model to plumes generated at low laser energy and expanding into vacuum. The measurements concern an experiment of laser ablation of silver, done at Risø National Laboratory in Denmark by the group of Dr. Jørgen Schou, and with the analysis done by the author [Hansen *et al.* 1999].

The experimental arrangement is depicted in Figure 5.1. A 6 ns (FWHM), $\lambda_l = 355$ nm laser, is used to ablate a silver target in vacuum ($<10^{-7}$ mbar) at a low fluence of 0.8 J cm^{-2}. The laser spot on the target is an ellipse with the semi-major axis X_0 =1.4 mm (vertical plane) and semi-minor axis Y_0 = 0.9 mm (horizontal plane)

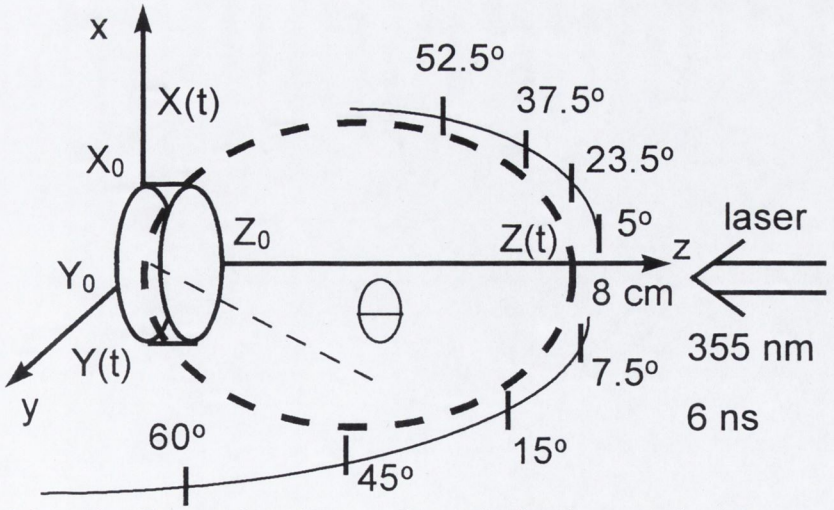

Figure 5.1: Schematic of Langmuir probe setup for monitoring the expansion into vacuum of a silver target. The probes are placed in a half-circle of 8 cm radius centred on the laser spot on the target.

Plane electrostatic probes (see section 3.3), facing the laser spot on the target, is used to monitor the ion outflow. The collecting area of a probe measures 0.5×0.5 cm^2.

5.1.3 Results and discussion

The hydrodynamic expansion model of section 2.1.1 is used to analyse the results. The numerical solution of the differential equation (Eq. (2.9)) is shown in Figure 2.3. For this problem the initial thickness was estimated to be $Z_0 = 15$ μm on the basis of a measured expansion velocity of $v_{front} = 2.1 \times 10^4$ m s^{-1}. This solution allows the normalised current density predicted by the model (see Eq. (2.10)) to be calculated for different angles. Figure 5.2 shows the model calculation, as well as the experimental recorded ion signals at three different angles.

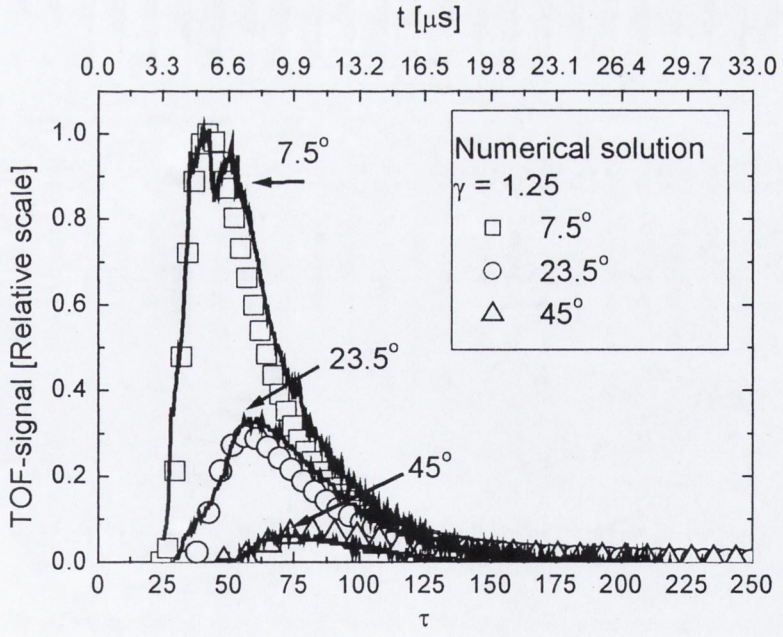

Figure 5.2: Measured ion TOF-signal angular variation (*line*) and calculated from Eq. (2.10) (*symbols*) at a radius of 8 cm from the laser spot on target. The experimental peak current at 7.5° corresponds to ~16 mA.

It is found from Figure 5.3 that the dimensionless unit of time $\tau = 1$ of the model, corresponds to 131 ns in this experiment. Since $\tau = t\,\beta^{1/2}/X_0$ we find that $\beta \sim 1.1\times10^8$ m^2 s^{-2} where $\beta = (5\gamma\text{-}3)E_0/M$ is proportional to the initial energy per mass of the plume.

In [Hansen *et al.* 1999] we determined the asymptotic aspect ratio of the expanding plume, Z_{inf}/Y_{inf}, from fitting the integrated probe current with Eq. (2.12). This quantity is of interest when we consider injecting a laser produced plasma into a capillary. Eq. (2.12) however is deduced under the limited assumption that $\tan\theta << Y/Z$ [Anisimov *et al.* 1993] besides, it is a cumbersome work to perform the initial integrations of the TOF-signals followed by the fitting. We proceed here to present a shorter calculation, again based on Anisimov's model of the plume expansion. For $t_{front} >> X_0 / \beta^{1/2}$, where t_{front} is the time the plume reaches the probe, the expansion has become practically inertial (see Figure 2.3), this means that the velocity of the plume front is constant. It follows from Eq. (2.8) that the density of an iso-density contour then will decrease as $n \sim t^{-3}$. Since the ion current is proportional to $n\times v$, the peak TOF-current $I_m \sim t_m^{-4}$, where t_m is the time of maximum current. Or alternatively the maximum ion current $I_m(\theta) \sim v^4(\theta) \sim R^4(\theta)$ where R is the distance to the point (y^*,z^*) on the iso-density contour of Figure 2.1. Using the formula for an ellipse $R^2 = z^{*2}/(z^{*2}\sin^2\theta + y^{*2}\cos^2\theta)$ we deduce that:

$$\sqrt{I_m(\theta)}\Big/\sqrt{I_m(0)} = \frac{1}{1+\left(\dfrac{z^{*2}}{y^{*2}}-1\right)\sin^2\theta} \qquad (5.1).$$

From a simple measurement of the peak current at different angles we can then determine the elongation of the plume z^*/y^* from (5.1). This is shown in Figure 5.3,

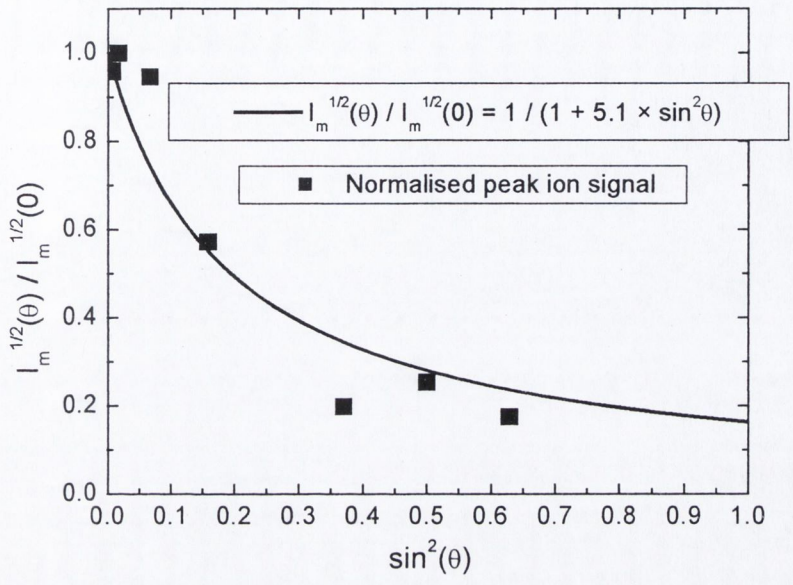

Figure 5.3: Square root of measured maximum current (*symbols*).Fit using Eq. (5.1) (*line*).

where the normalised current $I_m^{1/2}(\theta)$ is plotted *vs.* $\sin^2\theta$. From the fit we find that $z^*/y^* = 6.1^{1/2} = 2.5$ at the distance of 8 cm of the probes in the experiment.

In [Hansen *et al.* 1999] we determined the electron temperature as a function of time using the Langmuir probe. This is done by recording the TOF-current for each of the applied probe potentials and then evaluating the *I-V*-curve at a given time [Koopman 1971]. Figure 5.4 shows the variation of the measured electron temperature as well as the calculated temperature at a distance of 8 cm from the target and at an angle of 5° (Eq. (2.11)). It is of interest to note that the time-dependence of the measured temperature is qualitatively similar to the calculated. The peak temperature coincides almost in time with the peak ion current. The fact that the absolute value is not equal and the measured electron temperature is higher than the calculated is not surprising. The hydrodynamic model considers only one type of (uncharged) particles and does

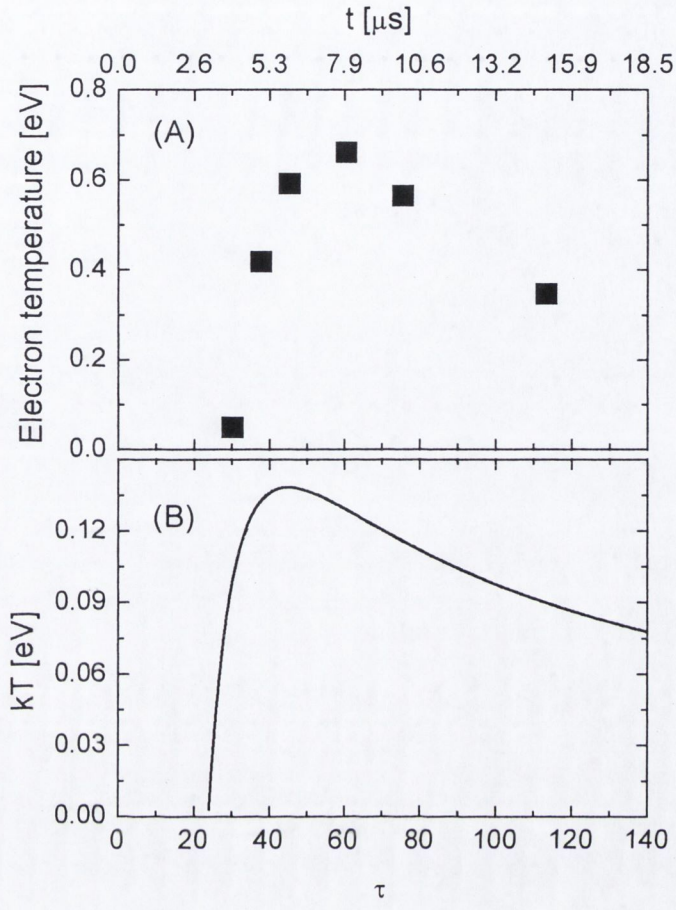

Figure 5.4: Measured electron temperature (TOP) and calculated gas temperature with $\gamma = 1.25$ (BOTTOM) at 5° and 8 cm from the target. τ is the normalised time defined after (2.13).

not account for the various energy equilibration processes between electrons and ions in the plasma. As an example we mention the discussion in section 3.4.6 where it is argued, that energy returned to the free electrons from 3-body recombination can modify the temperature scaling. The temperature range is similar to that measured by electrostatic probes by [Hendron *et al.* 1997] at a similar distance from the target. These authors ablated a copper target at 2.5 J cm^{-2} using a KrF-laser of 248 nm, but only measured the electron temperatures at late times (after the peak). The typical electron density, from the probe measurement, close to the normal is ~4×10^{17} m^{-3} [Toftmann et al. 2000] also consistent with [Hendron *et al.* 1997].

5.1.4 Conclusion

The investigations reported in this section have established, that the asymptotic expansion of the laser produced plasma from a plane target is well characterised by the isentropic solution to the hydrodynamic equations, presented in chapter 2. There is good correspondence between the angular distributions of the particle currents, Figure 5.2 and the temporal evolution of the electron temperature is consistent with the model. These measurements were done at a low laser fluence where the plume is only partly ionised [Hansen *et al.* 1997]. The measurements in chapter 4 and appendix B show that many of the scaling properties can be applied as well to fully developed plasma plumes.

5.2 Fast ICCD photography of pulsed laser ablation with modified target geometry.

5.2.1 Introduction

Fast intensified-CCD (ICCD) photography has been extensively used in pulsed laser ablation (PLA) experiments as *in situ* monitoring to obtain spatial and temporal information of the plume expansion. This is partly due to the ability to work as a diagnostic tool and provide information over a broad range of time scales, see schematic representation in Figure 5.5. An early example of the use of framed image photography in pulsed laser ablation experiments can be found in [Hughes 1975].

The expansion of a Li plume was investigated by [Whitty and Mosnier 1998] using ICCD frame photography and shadowgraphy. The expansion contours from the ablation of several multi-component targets (i.e. AlN, $BaTiO_3$, BN and $PbZr_{0.53}Ti_{0.47}O_3$) has been obtained in [Schenck *et al.* 1996]. The authors of that paper also compare their results with those obtained from a simulation of the expansion using an isothermal hydrodynamic model suggested by [Singh and Narayan 1990].

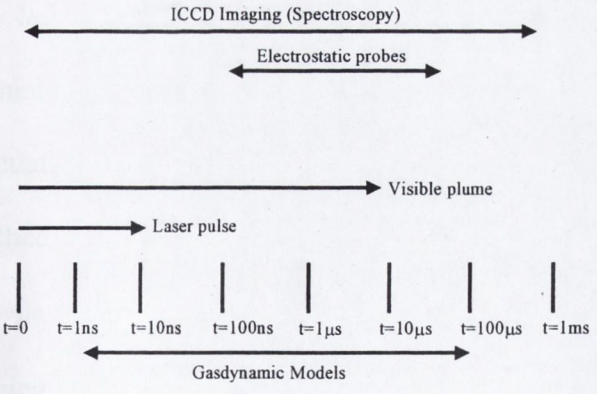

Figure 5.5: Applicability of different diagnostics technique discussed in this thesis compared to typical time scales in a PLA plume, based on [Schenck *et al.* 1996].

All of the above mentioned experiments were conducted with ablation of plane target surfaces. In [Andreić *et al.* 1999] and [Nishikawa *et al.* 1999] the influence of the target geometry on the soft x-ray emission, when ablated

with pulsed laser radiation, are discussed. Andreić ablated 0.5 mm diameter capillaries drilled in 1 – 2 mm slabs of Al. The XUV spectrum recorded from the plume, at the back of the capillary, is about an order of magnitude weaker and is dominated by lower ionisation stages than in the front. However after about 60 ns the XUV brightness of the back plasma is the same as for the front, and at later times their evolution was similar. Plume interaction with the sidewalls in a grooved Al-target is reported by Nishikawa to prolong the soft-x-ray signal. Finally, Weaver [Weaver and Lewis 2000] ablated a threaded cylindrical Al screw and investigated the polar particle flux distribution for different thread pitch length. They found that for large neck-to-neck distances of the thread the distribution becomes more forward peaked with increasing thread pitch distance.

5.2.2 Experimental setup

The experimental setup for our experiment is outlined in Figure 5.6. We use a Nd:YAG laser with a wavelength λ_l = 1064 nm and pulse width at FWHM of ~ 6 ns. The laser details as given by the manufacturer are summarised in Table 5.1. An aluminium (^{13}Al) target was ablated in a vacuum chamber. The chamber was evacuated using a turbomolecular pump whereby a base pressure $P < 10^{-4}$ mbar was reached. All experiments were undertaken at this background pressure. The target had flat bottom holes milled in it with a diameter of ϕ_{hole} = 1.5 mm and depths ranging from D_{hole} = 1 - 3 mm. For comparison the experiment was also conducted with ablation from a plane target.

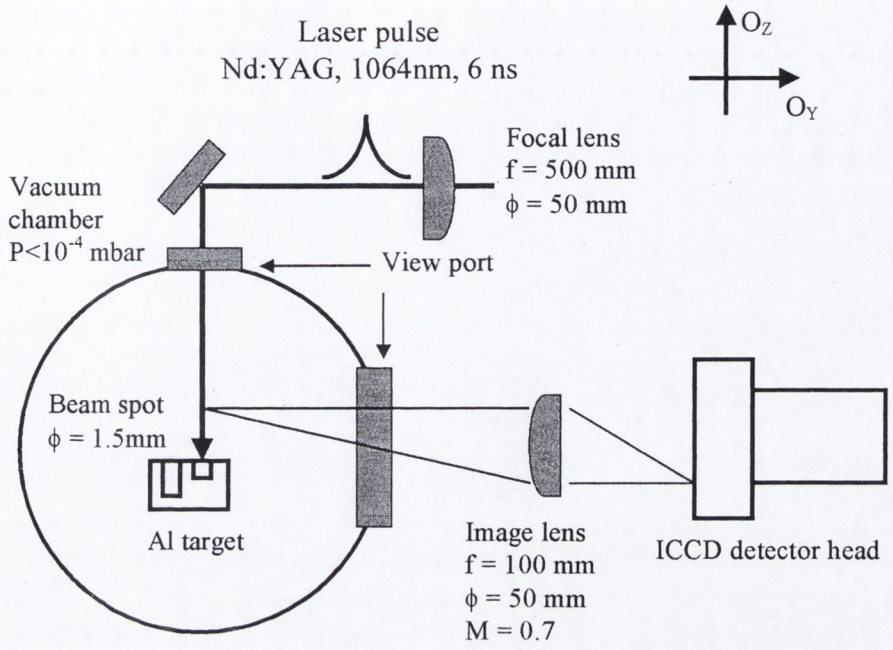

Figure 5.6: Schematic outline of the pulsed laser ablation setup for fast ICCD photography of the unfiltered spatial distribution of the plume emission from an Al target. The plume was imaged onto the detector head with a magnification M = 0.7. NB An electrostatic probe that was positioned 3 cm from the target surface is not shown on this drawing.

The laser pulse is partly focused onto the plane target or into the bottom of the drilled holes to form a spot with a diameter of ϕ_{laser} = 1.5 mm, the same as the diameter of the hole. An electrostatic probe with a cross section of 10^{-2} cm^2, placed 3 cm from the top surface of the Al target was used to monitor the ion outflow. The position of the probe was as close to normal as it could be without being hit by the laser pulse.

Table 5.1: Specifications of Nd:YAG Surelite Laser, model SL-20, at 10 Hz / 20 Hz repetition rate, respectively. From [Continuum].

	10 Hz / 20 Hz		10 Hz / 20 Hz
Max Energy (mJ) 1064 nm	320 / 300	Energy stability (%) 1064 nm	2.5 / 2.5
Pulse width (ns) FWHM for 1064 nm	5-7 / 5-7	Beam spatial profile* Near field (<1m) Far field	 0.7 / 0.7 0.95 / 0.95
Divergence (mrad)	0.6 / 0.6	Rod diameter (mm)	6 / 6

* Least squares fit to Gaussian profile. A perfect fit would have a coefficient of 1.

The probe circuit is similar to that described in chapter 3.3 – notably the load resistance is 50 Ω.

The ICCD used is from Andor Technology and is part of a spectroscopic system including an Oriel spectrograph model 260i. The spectrometer has been used to make spectroscopic measurements of the reactive plume in pulsed laser deposition of superconducting thin films [de Posada 2001]. In short the image intensifier head of the ICCD camera is made up by a photocathode where the input light strikes and releases electrons. The electrons are accelerated onto a microchannel plate that works as a super-fast shutter: for as long as the gate pulse is applied, the electrons are multiplied. On the output side of the microchannel plate the electrons are accelerated onto a phosphor coated on a fibre face plate. This component couples the image onto the CCD where it is detected. Further details of the quantum efficiency, phosphor relaxing time and optical gate widths for a given TTL pulse can be found in the manual [Andor Technology].

The triggering scheme for the recording of the ICCD images of the plume expansion is shown in Figure 5.7. The delay- and gating times were controlled by a Stanford Research System Inc., digital delay generator model DG535. The pulse width, Δt_{TTL}, of the TTL signal from the DG535 sent to the ICCD detector head determines the "opening" of the micro channel plate, hence what could be called the exposure time of the recorded image. Exposure here is understood as the time where electrons hitting the front of the MCP will be multiplied and transmitted through the MCP.

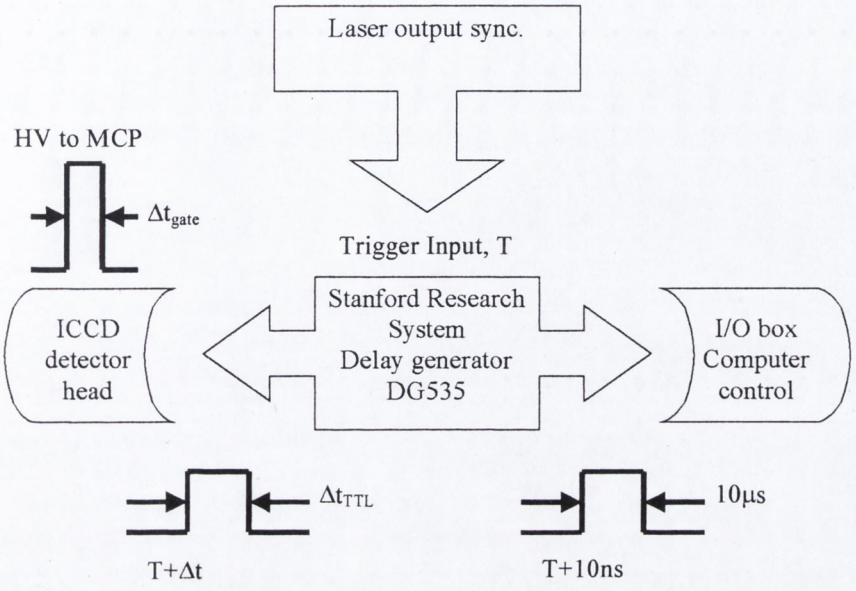

Figure 5.7: Schematic layout of the triggering used in the experiment.

This opening time will hereafter be referred to as the optical gate width, Δt_{gate}, and its value is tabulated in the manual [Andor Technology] for a given Δt_{TTL}. One picture is acquired for every shot and by changing the delay time, Δt, the time evolution of the plume expansion is recorded. The plume can be followed up to about 1.2 μs after the laser pulse has hit the target due to the limited field-of-view imposed by the viewport in the setup.

Before the chamber is evacuated, a screw is positioned just above the target where the laser will hit and the light from a He-Ne laser is flushed over the edges of the screw. An image is taken with the ICCD camera and after inspection the relative positions of the imaging lens and detector head are adjusted. The procedure is repeated until the image of the screw appears at its sharpest at which position the lens and detector head are locked in position. The image obtained along the length of the screw is shown in Figure 5.8 with the maximum intensity corresponding to the necks

pitched at an interval of an average Z_{CCD}=11 ±0.4 pixels. Hence from the measured distance from neck to neck on the thread of 400 ± 50 μm it is concluded that 1 pixel in the image corresponds to 37 ±6 μm in the object plane i.e. vertical along the surface normal of the target:

$$Z\,(or\ X) = [37 \pm 6] \times Z_{CCD}^{pixel}\,(or\ X_{CCD}^{pixel})\ \ \mu m\,. \qquad (5.2)$$

This confirms the measurement of the image and object distance in the setup where the demagnification was calculated to be ~0.7 (see Figure 5.6). Since one pixel has a dimension of 26 μm [Andor Technology] this should translate into 26 μm/0.7 = 37 μm along the target normal.

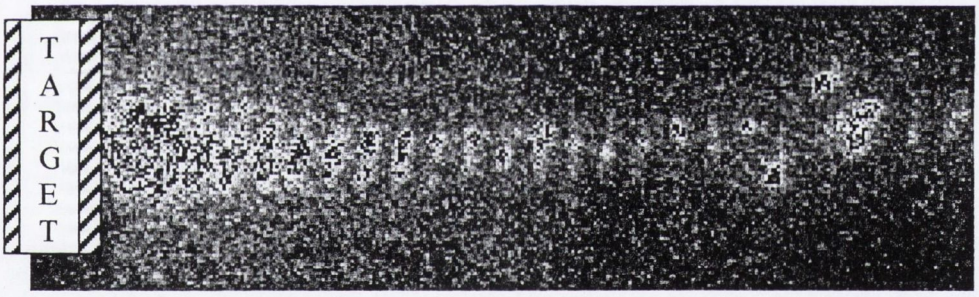

Figure 5.8: Image along the length of a screw positioned above the target at the position where the laser hits. The neck-to-neck distance is 11 pixels corresponding to 400μm. (False greyscale)

5.2.3 Results

As described above, the setup allowed us to record the unfiltered spatial distribution of the temporal evolution of the plume emission from an Al target with a modified surface structure. The aim is to investigate to what extent the plume expansion is influenced by the walls of the holes in the target for a possible future application involving a laser ablation filling of a capillary discharge. Table 5.2 summarises the conditions for the experiments reported in the rest of this section.

Table 5.2: Fluence and target conditions for the experiments reported in this section. The error in the fluence is calculated on the basis of the variation in the beam diameter of the laser on the target ϕ_{laser} = (1.5 ±0.2) mm.

Fluence	Δt_{gate}	Plane Al-target	Al-target with 1.5 mm diameter, 1 mm deep hole	Al-target with 1.5 mm diameter, 3 mm deep hole
(3.3 ± 1.1) J cm^{-2}.	4 ns	×	×	×
(2.1 ± 0.7) J cm^{-2}.	4 ns	×	×	×

To compare the different recordings the contours where the emission intensity has fallen to 33%, 50% and 80% of its maximum value is identified using the Andor software. The maximum lateral expansion, $2X_{CCD}$ in pixels, for the three contours is measured at the thickest point of the plume and then used to calculate the plume diameter $2X$, using equation (5.2). In Figure 5.9 we show the difference of the plume diameter measured at 33% of maximum intensity for the three different target geometries in the experiments.

When measuring the contour on the picture we estimate an error. The error in the plume dimension in the graphs below is taken as the maximum of either this estimated error or that given by equation (5.2) - whichever is largest. The similar plot for the expansion along the Z-direction, normal to the target surface, is shown in Figure 5.10. It is observed that there is no change in the height over the target *vs.* time in the longitudinal expansion of the plume whereas the lateral expansion is suppressed and the effect gets more pronounced the deeper the hole is.

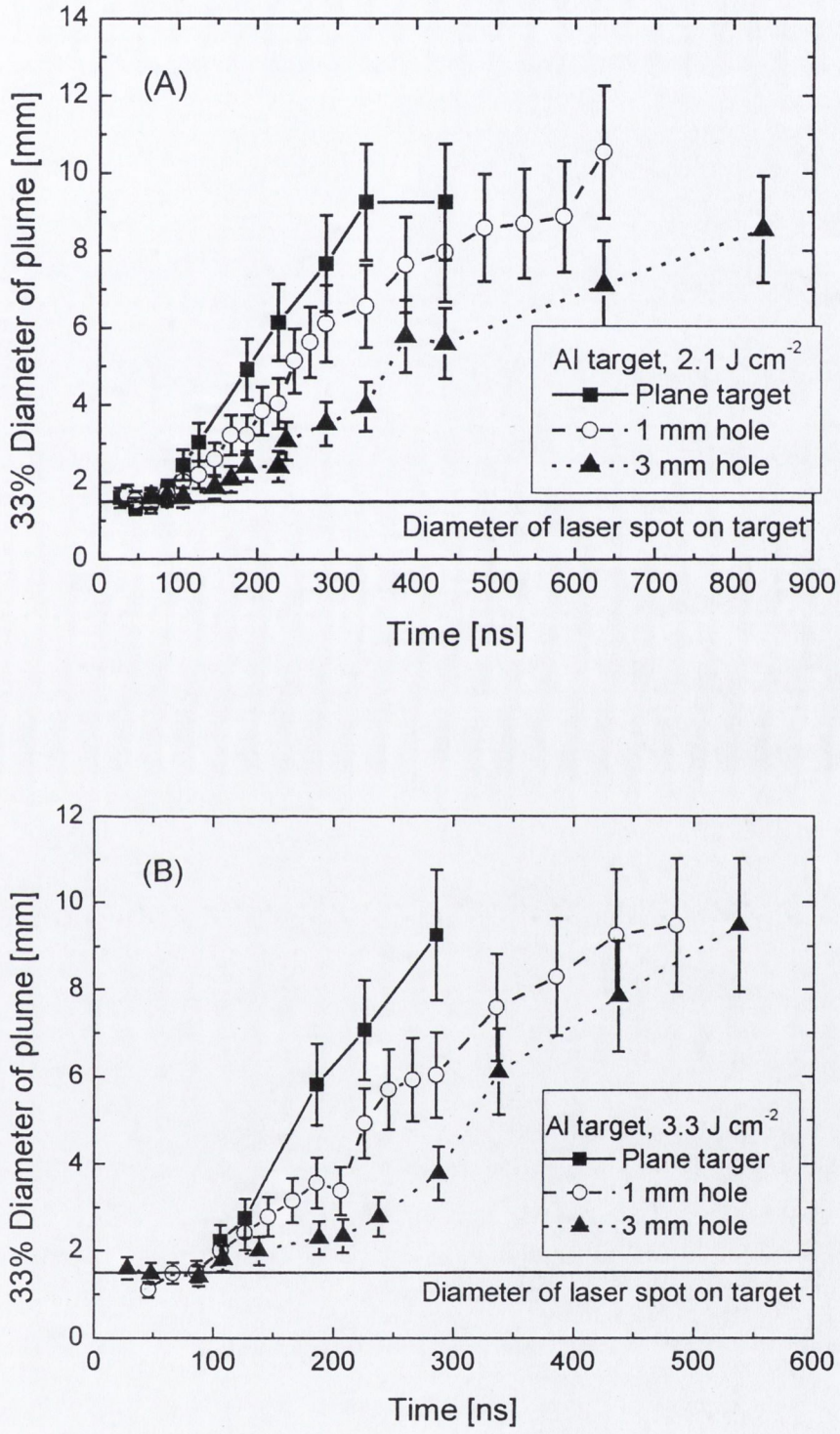

Figure 5.9: The diameter of the plume measured at the 33% contour *vs.* time when ablating an Al-target, either plane, 1 mm or 3 mm hole geometry. (A) Fluence 2.1 J cm^{-2}. (B) Fluence 3.3 J cm^{-2}. Solid line is a guide to the eye.

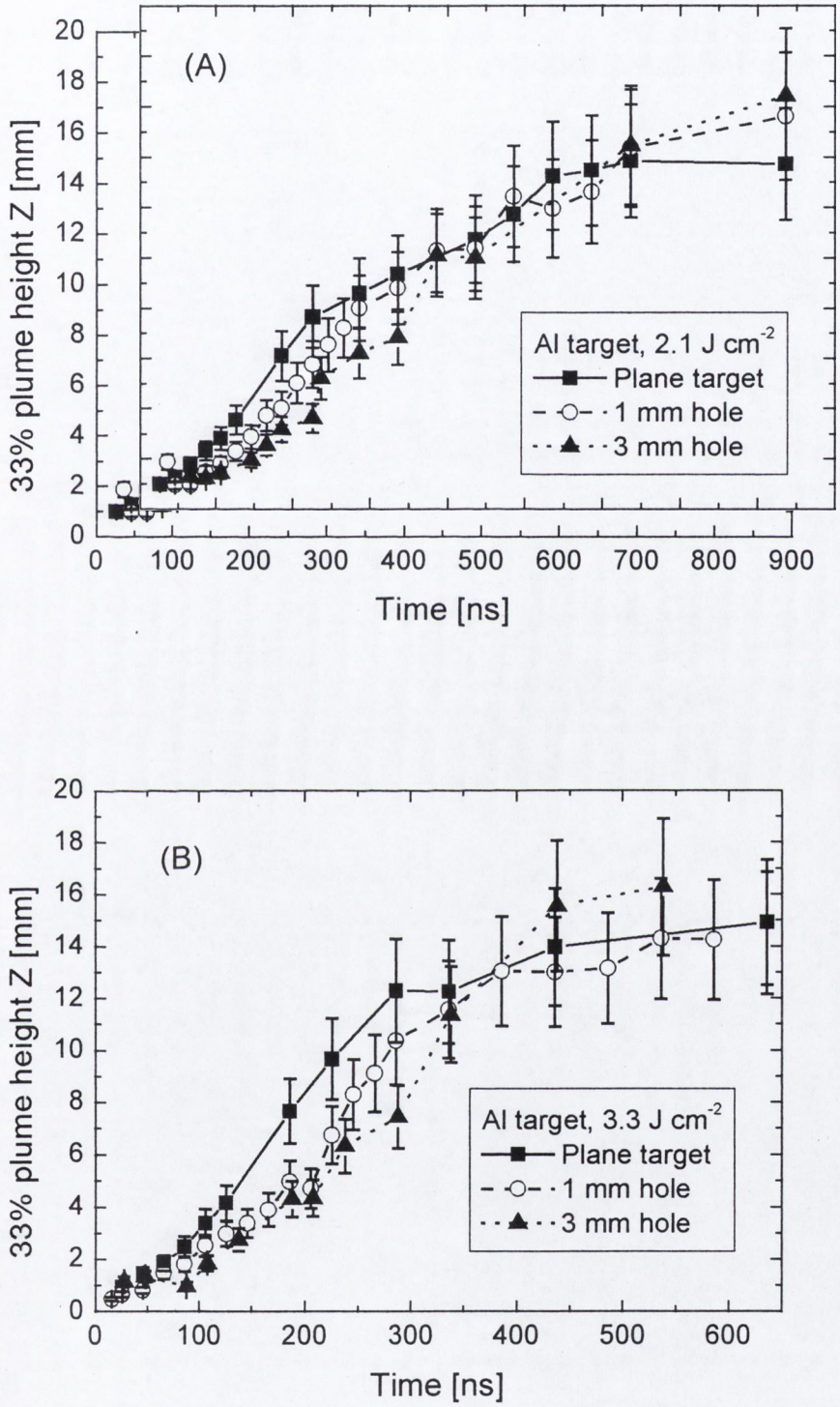

Figure 5.10: Height over the target of 33% contour *vs.* time. (A) Fluence 2.1 J cm^{-2}. (B) Fluence 3.3 J cm^{-2}. The velocity obtained from a linear fit to the plane target data is: (A) $v_z = (2.5 \pm 0.2) \times 10^4$ m s^{-1} and (B) $v_z = (3.6 \pm 0.2) \times 10^4$ m s^{-1}.

5.2.4 Discussion and analysis

Several authors have used hydrodynamic models to represent the expansion of the laser ablation plume, often relying on a multitude of assumptions to simplify the problem and obtain a "semi-" analytical solution of the basic hydrodynamic equations. A number of these rely on the assumption of an isothermal expansion, as is presented by [Singh and Narayan 1990] or [Kools *et al.* 1993]. Kools also applied the result to fit the experimental time-of-flight distributions obtained with a mass spectrometer from ablation of a Cu target [Kools *et al.* 1992].

Figure 5.9 shows that the asymptotic lateral expansion of the plume is reduced when the ablation takes place from the bottom of the hole. As the plume height over the target is less affected according to Figure 5.10 we conclude that the aspect ratio of plume is increased when ablating from the hole. We can apply the isentropic hydrodynamic model described in the previous section to the experiment here with the plane target geometry. The initial plume thickness, Z_0, that is needed to run the program, is estimated to be 37 μm (using Eq. (2.14)). In Figure 5.11 we plot the coordinates of the plume edge in the x and z directions along with the lateral velocity. It is observed that the plume expands to a height $Z = 3$ mm over the target in about 150 ns, in good accordance with Figure 5.10(A). At the same time the lateral acceleration has slowed down considerably and the velocity in the x and y direction has become almost constant as seen from dX/dt. This is the condition we expect for restricting the plume expansion in the directions perpendicular to the target normal. The narrower plume observed emerging from ablation in the hole is then a consequence of restricting the lateral plume expansion for a time equal to the time needed to reduce the lateral pressure gradient to almost zero.

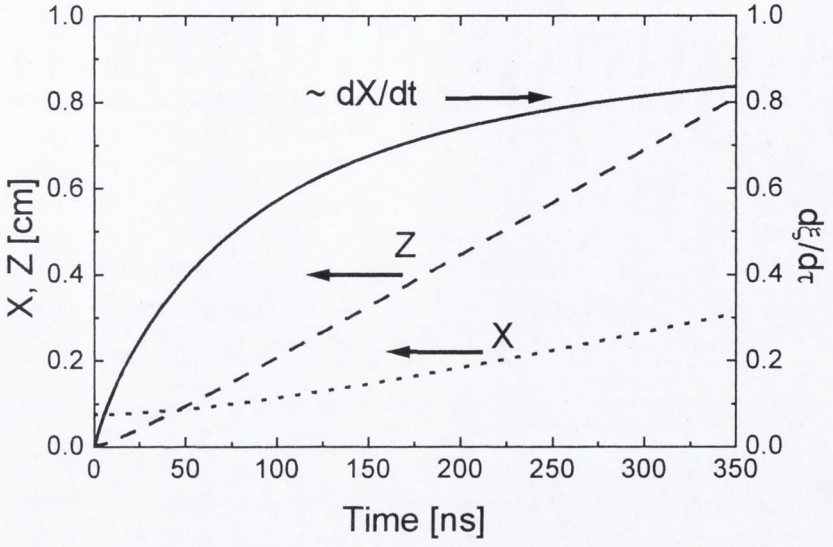

Figure 5.11: Isentropic hydrodynamic model for $X_0 = Y_0 = 0.075$ cm and $Z_0 = 37$ mm. Corresponding to low fluence case of (2.1±0.7) J cm^{-2}.

5.2.5 Conclusion and outlook

It has been shown that the asymptotic expansion of a laser produced plume can be considerably changed if the initial expansion is constricted in some dimensions. In terms of the isentropic expansion model, we can expect that the expansion will become increasingly influenced if the confinement is applied over a length comparable to the length scale where the plume expansion along that dimension would become inertial in the unrestricted expansion. In the experiments above this is almost achieved for the 3 mm deep hole.

To achieve an even better collimation of the flow one possible way forward is to look into the use of a hole with shaped walls. The use of optimum shaped nozzles to produce uniform supersonic flows is well known in the literature [Atkinson and Smith 1995] [Anderson 1982]. In short the nozzle angle θ_M, see Figure 5.12, is

determined from the Prandtl-Meyer function $\nu(M)$ where M is the Mach-number of the flow by the relationship:

$$\theta_M = \frac{\nu(M)}{2} \tag{5.2}$$

The Prandtl-Meyer function is given by:

$$\nu(M) = \sqrt{\frac{\gamma+1}{\gamma-1}}\arctan\sqrt{\frac{\gamma-1}{\gamma+1}\left(M^2-1\right)} - \arctan\sqrt{M^2-1} \tag{5.3}$$

For $\gamma = 1.26$ and $M \sim 8$ corresponding to $2/(\gamma\text{-}1)$, see Eq. (2.19), we find that $\nu = 122.5°$. In this case the nozzle angle should be ~62°. This discussion is of course based on the assumption of gas dynamics with no mention of plasma effect. It remains to be seen if it can be applied to a laser-produced plasma.

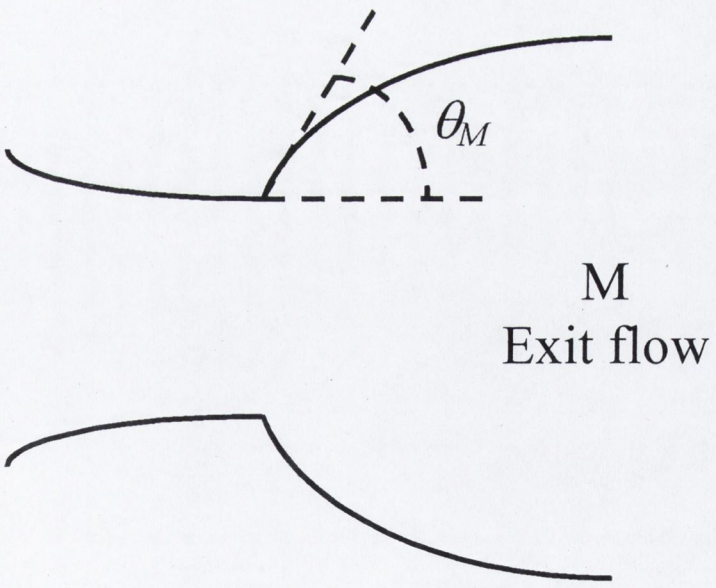

Figure 5.12: Sketch of nozzle design.

References

[chap 5] Anderson J.D. Jr. (1982). "*Modern Compressible flow – with historical pespective*". (McGraw-Hill).

[chap 5] Andor Technology "*System Performance*". Manual, Issue I, Rev 6.

[chap 5] Andreić Ž. Aschke L. and Kunze H.-J. (1999) "*Plasma plumes generated by laser ablation of capillaries*". Inst. Phys. Conf. Ser. No **159** (IOP Publishing) pp 495.

[chap 5] Anisimov S.I. Bäuerle D. and Luk'yanchuk B.S. (1993) "*Gas dynamics and film profiles in pulsed-laser deposition of materials*". Phys. Rev. B **48**(16) pp 12076.

[chap 5] Anisimov S.I. Luk'yanchuk B.S. and Luches A. (1996) "*An analytical model for three-dimensional laser plume expansion into vacuum in hydrodynamic regime*". Appl. Surf. Sci. **96-98** pp 24.

[chap 5] Atkinson D.B. and Smith M.A. (1995). "*Design and characterisation of pulsed uniform supersonic expansions for chemical applications*". Rev. Sci. Instrum. **66**(9), pp 4434.

[chap 5] Bäuerle D. (1995) "*Laser Processing and Chemistry*". Springer-Verlag, Second Edition, Berlin.

[chap 5] Continuum Manual, Continuum, 3150 Central Expressway, Santa Clara, CA 95051, US.

[chap 5] de Posada E. (2001). Transfer report, Trinity College Dublin.

[chap 5] Hansen T.N. Schou J. and Lunney J.G. (1997). "*Angular distribution of silver ions and neutrals emitted in vacuum by laser ions*". Europhys. Lett. **40**(4) pp 441.

[chap 5] Hansen T.N. Toftmann B. Schou J. and Lunney J.G. (1999) "*Lanmuir probe study of plasma expansion in pulsed laser ablation*". Appl. Phys. A **69**(Suppl.) pp S601.

[chap 5] Hendron J.M. Mahony C.M.O. Morrow T. and Graham W.G. (1997). "*Langmuir probe measurements of plasma parameters in the late stages of a laser ablated plume*". J. Appl. Phys. **81**(5), pp 2131.

[chap 5] Hughes T.P. (1975) "*Plasma and Laser Light*". Adam Hilger, London.

[chap 5] Kools J.C.S. Baller T.S. De Zwart S.T. and Dieleman J. (1992) "*Gas flow dynamics in laser ablation deposition*". J. Appl. Phys. **71**(9) pp 4547.

[chap 5] Kools J.C.S. van de Riet E. and Dieleman J. (1993) "*A simple formalism for the prediction of angular distributions in laser ablation deposition*". Appl. Surf. Sci. **69** pp 133.

[chap 5] Koopman D.W. (1971). "*Langmuir Probe and Microwave Measurements of the Properties of Streaming Plasmas Generated by Focused Laser Pulses*". Phys. Fluids **14**(8), pp 1707.

[chap 5] Nishikawa T. Nakano H. and Uesugi N. (1999) "*Enhancement of soft x-ray emission from femtosecond laser-produced plasma with a rectangular groove target*". Inst. Phys. Conf. Ser. No **159** (IOP Publishing) pp 539.

[chap 5] Puretzky A.A. Geohegan D.B. Hurst G.B. Buchanan M.V. and Luk'yanchuk B.S. (1999). "*Imaging of Vapour Plumes Produced by Matrix Assisted Laser Desorption: A Plume Sharpening Effect*". Phys. Rev. Lett. **83**(2), pp 444.

[chap 5] Rocca J.J. (1999) "*Table-top soft x-ray lasers*". Rev. Sci. Instrum. **70**(10) pp 3799.

[chap 5] Schenck P.K. Hastie J.W. Paul A.J. and Bonnell D.W. (1996) "*Imaging and gasdynamic modelling of pulsed laser deposition plumes*". Opt. Eng. **35**(11) pp 3199.

[chap 5] Singh R.K. and Narayan J. (1990) "*Pulsed-laser evaporation technique for deposition of thin films: Physics and theoretical model*". Phys. Rev. B **41**(13) pp 8843.

[chap 5] Toftmann B. Schou J. Hansen T.N. and Lunney J.G. (2000) "*Angular Distribution of Electron Temperature and Density in a Laser-Ablation Plume*". Phys. Rev. Lett. **84**(17) pp 3998.

[chap 5] Weaver I. and Lewis C.L.S. (2000) "*A case study with a new novel geometry for pulsed laser deposition*". J. Phys. D: Appl. Phys. **33**(3) pp 175.

[chap 5] Whitty W. and Mosnier J.-P. (1998) "*Diagnostic of an expanding laser-produced lithium plasma using ICCD frame photography and shadowgraphy*". Appl. Surf. Sci. **127-129** pp 1035.

[chap 5] Wyndham E. Aliaga-Rossel R. Chuaqui H. Favre M. Mitchel I. Choi P. and Krisch I. (2000). "*X-ray and Plasma Dynamics of an intermediate size capillary discharge*". 42nd Annual meeting of the APS Division of Plasma Physics. Session MP1 – Poster Session VII, Poster MP1.087.

CHAPTER 6

Conclusions

In this thesis I have described the investigation of a fast micro capillary discharge plasma source, as well as laser produced plasmas generated using nanosecond laser pulses. The pulsed plasma, produced in the two experiments, is a source of ion outflow, with the kinetic energy of particles reaching several keV, and line radiation emission into the soft X-ray region.

6.1 The micro capillary discharge source

The micro capillary discharge represents a novel close-coupled low-inductance discharge source. Applications for such a micro volume high energy density discharge were suggested at the beginning of Chapter 3, where it is mentioned that it could be used to investigate physical phenomena previously only produced in much larger electrical discharge installations or soft X-ray laser experiments.

In the electrical measurements we found from the current recordings that, within the uncertainty of the data, the current rate of change, dI/dt, which can be achieved is 10^{13} As^{-1}. This value is sufficiently high for pinching of the plasma column in e.g. the soft X-ray laser of Rocca [Rocca 1999]. For the micro capillary experiment we concluded in section 3.3.3 that pinching was not achieved based on the equilibrium considerations of the Bennett-equation. We note that the line density in Rocca's experiment is typical about $N_i \sim 10^{15}$ cm^{-1} at the time of lasing [Rocca 1999] while it in the micro capillary is around $N_i \sim 5\times10^{17}$ cm^{-1} (p 63). A lower line density in the micro capillary discharge would favour pinching. It is suggested here that by

changing the micro capillary to e.g. a ceramic material, mentioned as well in section 4.4 for improving the lifetime of a discharge cell, we would solve both the problem of producing pinching as well as the short life time of an experiment with a micro capillary discharge cell due to less material removal from the dielectric during the discharge.

The ion outflow from the micro capillary plasma was measured using an ion probe (Langmuir probe) and a Thomson parabola analyser. The ion probe measurements were performed at different distances from the discharge cell, in the stage of the plasma expansion where the flow has become inertial. Here it produces important information about the ion flow time-of-flight. The ion probe signal was split into a fast pulse, that was found to travel at a constant expansion velocity, and a slower pulse that appeared to be slowing down. We believe this can be explained by part of the plasma from the micro capillary (that in the slow pulse) expanding in a blast wave formed due to collisions with the background atmosphere in the chamber. To quantify that we calculated on p 57 the mean-free-path for the plasma ions at a background pressure of 10^{-3} mbar in the chamber and concluded that it was of the order of the distance to the probe, which is known from laser produced plasma experiments to lead to plume spitting [Wood *et al.* 1997]. One drawback in using the ion probe with the micro capillary is that secondary electron emission will take place because of the ~kV energies of the ions in the flow. The secondary electron emission increases the uncertainty in determining the ion density from the probe signal.

The Thomson parabola analyser was a simple tool to obtain the partial charge resolved velocity distribution of the ions in the plasma downstream from the micro capillary. As a result, we find that multiple charged ions are present in the plume far

from the discharge cell. At first, it can be surprising that we find high charge ions far from the micro capillary, since the 3-body recombination process responsible for recombination should proceed rapidly as the plasma cools due to the dependence $T_e^{-4.5}$. However the data can be explained by a model of *freezing-in* of the charge states in an expanding plasma being in a non-equilibrium state as discussed in section 3.4.6. Further, in the Thomson analyser data we do not register Aluminium ions that could have come from the back electrode. This confirms partly the spectroscopic data where Aluminium lines were also not seen. It may be that the Aluminium is hidden by the plasma from the dielectric. The measurements are limited at low velocities by the decreasing efficiency of the MCP when detecting ions with energies below ~ 1 kV.

The time-resolved soft x-ray emission spectrum of the micro capillary discharge was due to lack of time only done for the positive charging of the back electrode where the energy density is smallest as confirmed by the ion probe measurements as well. The lines in the spectra are identified as belonging to Be- and Li-like oxygen and Li-like carbon lines. By applying a collisional-radiative plasma physics model named FLY we could calculate an expected line strength ratios for the Li-like carbon to Li-like oxygen lines as a function of temperature. Comparing the result to that from the detected spectra we deduced a temperature of less than 10 eV. This agrees with the temperature deduced from the ion expansion velocity measured with the ion probe. This analysis shows the versatility of the FLY model that was used as well in connection with the laser produced plasma experiments. On the future perspectives of the work with the micro capillary we can say that work is ongoing on designing a

revised discharge geometry producing a higher resistance whereby increased heating of the plasma will be possible.

6.2 Laser produced plasma

The first detailed comparison with measurements of Anisimov's model, presented in section 2.1.1, was made possible with the use of laser produced plasma. Experiments were conducted at low laser intensity with a silver target where the plume is expected to be only partial ionised and the gas dynamical model is expected to apply best. The measurement of the angular ion distribution was particularly well correlated with the predictions from the model. Also the temporal evolution of the temperature as measured locally with an ion probe downstream in the plasma outflow from the target also showed good correlation with that of the model.

The work on the Anisimov's model was extended to higher laser intensities where the plasma parameters are similar to those that can be obtained in the micro capillary discharge. Using time resolved soft x-ray emission spectra obtained from a carbon target irradiated at 5 $GWcm^{-2}$, and comparing to theoretical spectra calculated using the FLY-code, we deduced the time evolution of the plasma temperature and density during the early time of evolution of the plume at the target surface. The time evolution of the temperature and density at the target as calculated from Ansimov's model showed again good correlation with the data provided account is taken of the mean ionisation in the expression for the temperature. This shows that it is possible to adopt Anisimov's gas dynamic model to deal with the expansion of a fully ionised plasma.

The laser produced plasma source was also investigated in a geometry where the expansion of the plume is constricted. Visible plume imaging using a gated intensified CCD was used to map the change in the expansion dynamics when the ablation takes place from the bottom of a hole. The observed plume angular distribution becomes narrower the deeper the hole. Since we are thinking of ways to fill a capillary discharge it is thought that the more peaked the angular distribution the better. Here, an improved design using a nozzle shaped hole is suggested as the next step. The Anisimov model has been established as a versatile tool for interpreting the results of plasma expansion under many conditions. The elliptical dependence of the flow parameters provides an easy scaling to be applied to many results from expanding plasma into vacuum.

References

[chap 6] Rocca J.J. (1999). "*Table-top soft x-ray lasers*". Rev. Sci. Instrum. **70**(10), pp 3799.

[chap 6] Wood R.F. Chen K.R. Leboeuf J.N. Puretzky A.A. and Geohegan D.B. (1997). "*Dynamics of plume propagation and splitting during pulsed laser ablation*". Phys. Rev. Lett. **79**(8), pp 1571.

APPENDIX A

A.1 Computer program to solve Anisimov's expansion model

In Chapter 2 we presented the expansion model by Anisimov *et al.* [Anismov *et al.* 1993, 1996]. It was shown in those references that the hydrodynamic equations could be solved under the assumption of constant flow variables on elliptical surfaces. The problem reduces to that of three coupled second-order differential equations of the plume edge coordinates X, Y and Z:

$$\frac{X}{\beta}\frac{\partial^2 X}{\partial t^2} = \frac{Y}{\beta}\frac{\partial^2 Y}{\partial t^2} = \frac{Z}{\beta}\frac{\partial^2 Z}{\partial t^2} = \left[\frac{X_0 Y_0 Z_0}{XYZ}\right]^{\gamma-1} \tag{2.9}$$

β being defined as $\beta = (5\gamma\text{-}3)E/M$, where E and M are the total energy of the vapour plume and total mass of the plume, respectively. Introducing, like in Anisimov, the dimensionless variables $\xi = X/X_0$, $\eta = Y/X_0$, $\zeta = Z/Z_0$ and $\tau = t\beta^{1/2}/X_0$ the above equation becomes:

$$\xi\ddot{\xi} = \eta\ddot{\eta} = \zeta\ddot{\zeta} = \left[\frac{\eta_0\zeta_0}{\xi\eta\zeta}\right] \tag{A.1}$$

The subscript 0 refers to initial values, $\xi_0 = 1$, $\eta_0 = Y_0/X_0$, $\zeta_0 = Z_0/X_0$, $\dot{\xi}_0 = \dot{\eta}_0 = \dot{\zeta}_0 = 0$.

Equation (A.1) was solved using a fourth order Runge-Kutta-Nyström method [Kreyszig 1993]. The general problem is that of

$$y'' = f(x, y, y'),\ y(x_0) = y_0,\ y'(x_0) = y'_0 \tag{A.2}$$

Using the notation of Kreyszig the iteration step size is h and we define k =0.5h and we further define the variables:

$$
\begin{aligned}
A_n &= kf(x_n, y_n, y'_n) \\
B_n &= kf(x_n + k, y_n + \beta_n, y'_n + A_n), \ \beta_n = k\left(y'_n + \frac{1}{2}A_n\right) \\
C_n &= kf(x_n + k, y_n + \beta_n, y'_n + B_n) \\
D_n &= kf(x_n + h, y_n + \delta_n, y'_n + 2C_n), \delta_n = h(y'_n + C_n)
\end{aligned}
\tag{A.3}
$$

Then in each step we can calculate:

$$
\begin{aligned}
y_{n+1} &= y_n + h\left(y'_n + \frac{1}{3}(A_n + B_n + C_n)\right) \\
y'_{n+1} &= y'_n + \frac{1}{3}(A_n + 2B_n + 2C_n + D_n)
\end{aligned}
\tag{A.4}
$$

For the case of Equation (A.1) we can now calculate the coefficients from Equation (A.3). For ξ it follows that:

$$
\begin{aligned}
A_n(\xi) &= k\frac{1}{\xi_n}\left[\frac{\eta_0\zeta_0}{\xi_n\eta_n\zeta_n}\right]^{\gamma-1} \\
B_n(\xi) &= k\frac{1}{\xi_n + k\left(\dot{\xi}_n + \frac{1}{2}A_n\right)}\left[\frac{\eta_0\zeta_0}{\left(\xi_n + k\left(\dot{\xi}_n + \frac{1}{2}A_n\right)\right)\eta_n\zeta_n}\right]^{\gamma-1} \\
C_n(\xi) &= B_n(\xi) \\
D_n(\xi) &= \frac{1}{\xi_n + h(\dot{\xi}_n + C_n)}\left[\frac{\eta_0\zeta_0}{(\xi_n + h(\dot{\xi}_n + C_n))\eta_n\zeta_n}\right]^{\gamma-1}
\end{aligned}
\tag{A.5}
$$

The coefficients for η and ζ are obtained from (A.5) by cycling the letters above.

The program is written as a *LabTalk* program to run in the script window in the Origin mathematical program [Microcal™ Origin]. The raw commented code is pasted in below as Figure A.1.

```
# Integration of plasma expansion according to model in Appl. Surf. Sci 96-98, 24, (1996), Eq (12).
#The method is that of; a 4.-Order Runge-Kutta-Nystrom (RKN). This program works with the Origin
#project "ansmv.opj"
#
#============NOTES TO PROGRAM=================
# 1) The step-size, hlow, is used from tau=0 to tau=taulow. From tau=taulow to tau=tauhigh the step-
#size is hhigh. The mentioned variables should be written in the columns.
# 2) Initial γ, η0 and ζ0 values should alsa be inserted.
# 3) The last 7 colums should be blank before running the program.
#==========END NOTES TO PROGRAM===============;

#==========PROGRAM=====================;
# Initial conditions.
Data1_tau[1]=0;
Data1_xi[1]=1;
A= Data1_eta0[1];
B= Data1_zeta0[1];
Data1_eta[1]=A;
Data1_zeta[1]=B;
Data1_xipdot[1]=0;
Data1_etapdot[1]=0;
Data1_zetapdot[1]=0;
gamma=Data1_gamma[1];          # gamma is read.

taulow=Data1_tauplow[1];       # first interval.
tauhigh=Data1_tauphigh[1];     # second interval.
hlow=Data1_hplow[1];           # Increment in first interval.
hhigh=Data1_hphigh[1];         # Increment in second interval.
klow=hlow/2;                   # RKN step. 1. Interval.
khigh=hhigh/2;                 # RKN step. 2. Interval.

Nlow=taulow/hlow;              # No. of loops in 1. Interval.
Nhigh=(tauhigh-taulow)/hhigh;  # No. of loops in 2. Interval.

Loop(i,1,Nlow)                 # First interval.
{
C=Data1_xi[i];
D=Data1_eta[i];
E=Data1_xipdot[i];
F=Data1_etapdot[i];
G=Data1_zeta[i];
H=Data1_zetapdot[i];

# NB. The RKN variable "C??" is equal to "B??" for this particular diff. eq.

# Xi variable is treated.
Axi=klow*(1/C)*(A*B/(C*D*G))^(gamma-1);
Bxi=klow*(1/(C+klow*(E+0.5*Axi)))*(A*B/((C+klow*(E+0.5*Axi))*D*G))^(gamma-1);
Dxi=klow*(1/(C+hlow*(E+Bxi)))*(A*B/((C+hlow*(E+Bxi))*D*G))^(gamma-1);

Data1_xi[i+1]=C+hlow*(E+(1/3)*(Axi+2*Bxi));
Data1_xipdot[i+1]=E+(1/3)*(Axi+4*Bxi+Dxi);
# Eta variable is treated.
Aeta=klow*(1/D)*((A*B)/(C*D*G))^(gamma-1);
Beta=klow*(1/(D+klow*(F+0.5*Aeta)))*((A*B)/((D+klow*(F+0.5*Aeta))*C*G))^(gamma-1);
Deta=klow*(1/(D+hlow*(F+Beta)))*((A*B)/((D+hlow*(F+Beta))*C*G))^(gamma-1);
```

```
Data1_eta[i+1]=D+hlow*(F+(1/3)*(Aeta+2*Beta));
Data1_etapdot[i+1]=F+(1/3)*(Aeta+4*Beta+Deta);

# Zeta variable is treated.
Azeta=klow*(1/G)*((A*B)/(C*D*G))^(gamma-1);
Bzeta=klow*(1/(G+klow*(H+0.5*Azeta)))*((A*B)/((G+klow*(H+0.5*Azeta))*C*D))^(gamma-1);
Dzeta=klow*(1/(G+hlow*(H+Bzeta)))*((A*B)/((G+hlow*(H+Bzeta))*C*D))^(gamma-1);

Data1_zeta[i+1]=G+hlow*(H+(1/3)*(Azeta+2*Bzeta));
Data1_zetapdot[i+1]=H+(1/3)*(Azeta+4*Bzeta+Dzeta);

Data1_tau[i+1]=Data1_tau[i]+hlow;                    # Time is increased
};

Loop(i,1,Nhigh)                                      # Second interval.
{
C=Data1_xi[i+Nlow];
D=Data1_eta[i+Nlow];
E=Data1_xipdot[i+Nlow];
F=Data1_etapdot[i+Nlow];
G=Data1_zeta[i+Nlow];
H=Data1_zetapdot[i+Nlow];

# Same as before for new interval.

Axi=khigh*(1/C)*(A*B/(C*D*G))^(gamma-1);
Bxi=khigh*(1/(C+khigh*(E+0.5*Axi)))*(A*B/((C+khigh*(E+0.5*Axi))*D*G))^(gamma-1);
Dxi=khigh*(1/(C+hhigh*(E+Bxi)))*(A*B/((C+hhigh*(E+Bxi))*D*G))^(gamma-1);

Data1_xi[i+1+Nlow]=C+hhigh*(E+(1/3)*(Axi+2*Bxi));
Data1_xipdot[i+1+Nlow]=E+(1/3)*(Axi+4*Bxi+Dxi);

Aeta=khigh*(1/D)*((A*B)/(C*D*G))^(gamma-1);
Beta=khigh*(1/(D+khigh*(F+0.5*Aeta)))*((A*B)/((D+khigh*(F+0.5*Aeta))*C*G))^(gamma-1);
Deta=khigh*(1/(D+hhigh*(F+Beta)))*((A*B)/((D+hhigh*(F+Beta))*C*G))^(gamma-1);

Data1_eta[i+1+Nlow]=D+hhigh*(F+(1/3)*(Aeta+2*Beta));
Data1_etapdot[i+1+Nlow]=F+(1/3)*(Aeta+4*Beta+Deta);

Azeta=khigh*(1/G)*((A*B)/(C*D*G))^(gamma-1);
Bzeta=khigh*(1/(G+khigh*(H+0.5*Azeta)))*((A*B)/((G+khigh*(H+0.5*Azeta))*C*D))^(gamma-1);
Dzeta=khigh*(1/(G+hhigh*(H+Bzeta)))*((A*B)/((G+hhigh*(H+Bzeta))*C*D))^(gamma-1);

Data1_zeta[i+1+Nlow]=G+hhigh*(H+(1/3)*(Azeta+2*Bzeta));
Data1_zetapdot[i+1+Nlow]=H+(1/3)*(Azeta+4*Bzeta+Dzeta);

Data1_tau[i+1+Nlow]=Data1_tau[i+Nlow]+hhigh;
};
```

Figure A.1: Program for running Anisimov's model.

The program works with the worksheet, Data1 shown below Figur A.2.

Data1													
Gamma	eta0	zeta0	hplow	hphigh	tauplow	tauphigh	Tau	xi	eta	zeta	Xipdot	etapdot	zetapdot

Figure A.2: Worksheet for running Anisimov's model.

References

[chap A] Anisimov S.I. Bäuerle D. and Luk'yanchuk B.S. (1993) "*Gas dynamics and film profiles in pulsed-laser deposition of materials*". Phys. Rev. B **48**(16) pp 12076.

[chap A] Anisimov S.I. Luk'yanchuk B.S. and Luches A. (1996) "*An analytical model for three-dimensional laser plume expansion into vacuum in hydrodynamic regime*". Appl. Surf. Sci. **96-98** pp 24.

[chap A] Kreyszig E. (1993) "*Advanced Engineering Mathematics*" Wiley, New York, 5th edn.

[chap A] Microcal Origin 5.0 *or later*. Copyright 1991-1997. Microcal Software Inc.

APPENDIX B

B.1 Pulsed laser ablation of metal targets

This appendix presents further results of experiments conducted in order to cast light on the physical mechanism involved in the expansion of a laser generated ablation plume from metal targets in vacuum. The angular distribution of ejected particles is measured using electrostatic probes and the results compared to the hydrodynamic expansion model presented in section 2.1. These experiments were undertaken at Trinity College Dublin and they formed the basis of a final year project by one member of our group [Dogget 1999].

B.1.1 Introduction

Low-intensity laser ablation is a versatile technique for materials processing and deposition. Due to the possible congruent transfer from bulk to thin film much work has been done on pulsed laser deposition (PLD) of different complex materials. Much of the progress in the field has been summarised by [Chrisey and Hubler 1994]. The detailed physical plasma and hydrodynamic processes that take place in the interaction of the laser pulse with the vapour plume formed on the target, as well as the plume interaction with the background gas, are still the subject of investigations. The recent review by [Amoruso *et al.* 1999] presents an overview of much of the effort in understanding the physical mechanisms of laser ablation.

One area of interest to understand is that of the angular distribution of the laser ablation plume since this is of importance for the uniformity of the deposited films.

We did some investigations of this [Hansen *et al.* 1997], partly in response to a discrepancy in the reported literature about the distribution of the ions *vs.* that of the neutral part of the plume. This is also the subject of an extended investigation by [Buttini *et al.* 1998] and [Thum-Jäger and Rohr 1999]. These authors reported charge resolved angular distributions for several metals irradiated with an infrared pulsed laser ($\lambda_l = 1.06$ μm). They concluded that there is a correlation between the peaking of the angular distribution and the atomic mass of the target material. The work reported here sets about to complement this study by measuring the angular charge distribution for different metals at an UV-laser wavelength instead of the infrared used by the mentioned authors. Also we include a theoretical frame work to explain the observed trends in the form of the hydrodynamic expansion model reported by [Anisimov *et al.* 1996].

B.1.2 Experimental details

The experimental setup is sketched in Figure B.1. The laser pulse from a KrF laser ($\lambda_l = 248$ nm, $\tau_{laser} \sim 26$ ns) is used to ablate targets of Al, Ti and Cu respectively. An aperture in the beam path is imaged onto the target to produce a rectangular 1.5×0.5 mm^2 laser spot profile. The targets are mounted in a high-vacuum chamber with a background pressure $P < 10^{-5}$ mbar. A plane electrostatic probe (Langmuir probe), with area 3 mm^2, is used for charge collection measurements of positive ions in the ablation plume. The probe potential is set at –25 V. The electrical circuit of the probe is shown in Figure B.2. It is the same type as that of [Koopmann 1971] and that used previously in the group [Jordan 1997]. A digital oscilloscope is used to record the time-of-flight (TOF) spectrum of the ion outflow recorded by the probe.

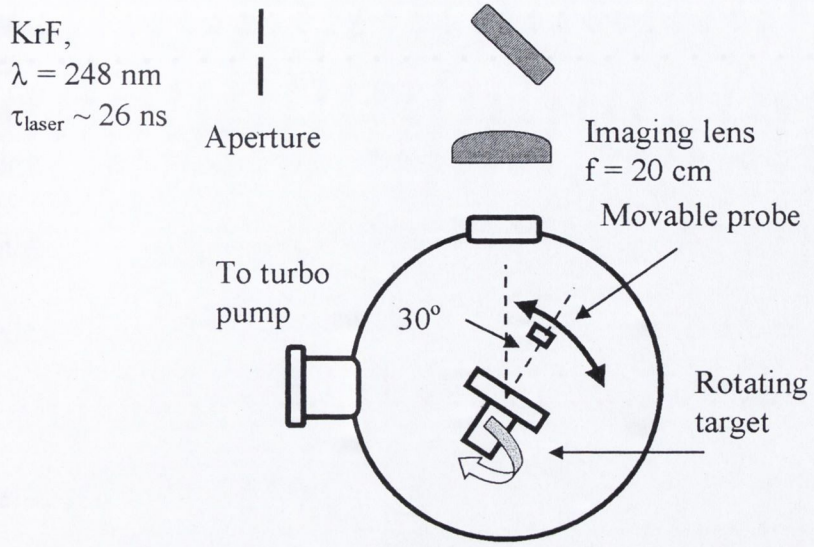

Figure B.1: Setup for laser ablation experiment of Al, Ti and Cu metal targets.

The probe can be rotated around the centre of the chamber in angles measured from the target normal from –20° to +50°, where the negative sign indicates angles towards the incoming laser beam. The corresponding ion TOF distribution is measured at a range of angles for each of the three target materials: Al, Ti and Cu.

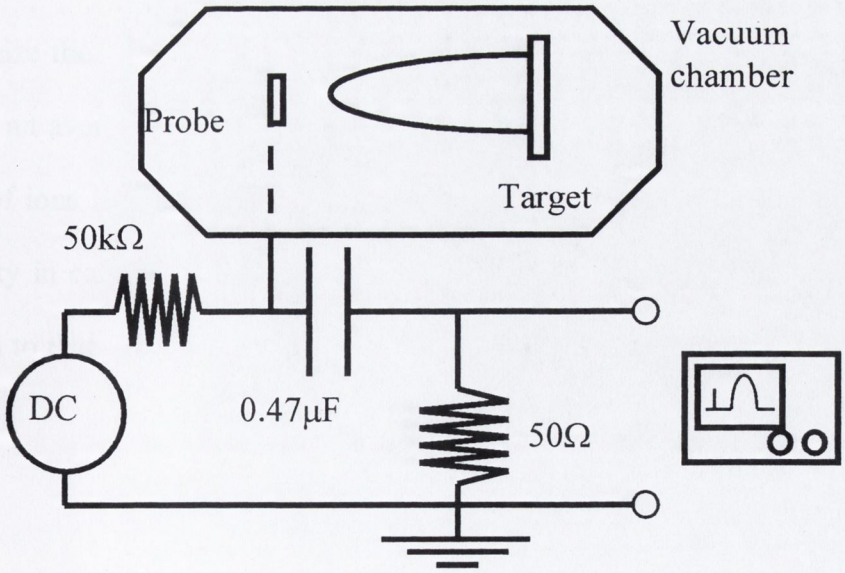

Figure B.2: Probe circuit.

The measurements are repeated for different target-to-probe distances d_{pr} from 4 - 6 cm and for different laser fluences on the target in the range ~ 5 – 11 J cm^{-2}.

The current collected by the probe I_{pr} as given by the TOF-distribution is integrated to give the total charge or no of ions $N = \int \sum n_i(t) Z_i \, dt$ intercepted by the probe. In general the probe current is written [Koopman 1971] (see also section 3.3):

$$I_{pr} = e\left\{\sum n_i(t) Z_i\right\} A v_i \qquad \text{(B.1)}$$

Here v_i is the ion velocity assumed equal to d_{pr}/t, n_i is the number density of ions with ionisation stage Z_i. We can assume that the ions are mostly singly ionised which simplifies the above expressions (on the ionisation degree in laser ablation of Cu and Al using pulsed UV laser see [Amoruso *et al.* 1999b]). As discussed in section 3.3, equation (B.1) is deduced under the assumption of $|e(V_B - V_p)| << 1/2\ m_i\ v_{flow}^2$, where V_B and V_p are the potential on the probe and the plasma potential, respectively, and m_i is the ion mass. Though in the plasma plume it was argued that the restriction is less important due to the small Debye length, section 3.3.

To minimize the effect of shot to shot variation in the collected ion TOF-signal each record is an average by the oscilloscope of 4 shots. The overall uncertainty for the number of ions is estimated to be < 25 % as in [Thum-Jäger and Rohr 1999]. The uncertainty in calculating the fluence is a measure of the ablated spot on the target compared to that expected with the demagnification of the imaging system.

B.1.3 Results

In Figure B.3 we show an example of the collected ion signal for a Ti target at 5 cm and a fluence of 8.5 ± 1.2 J cm^{-2}.

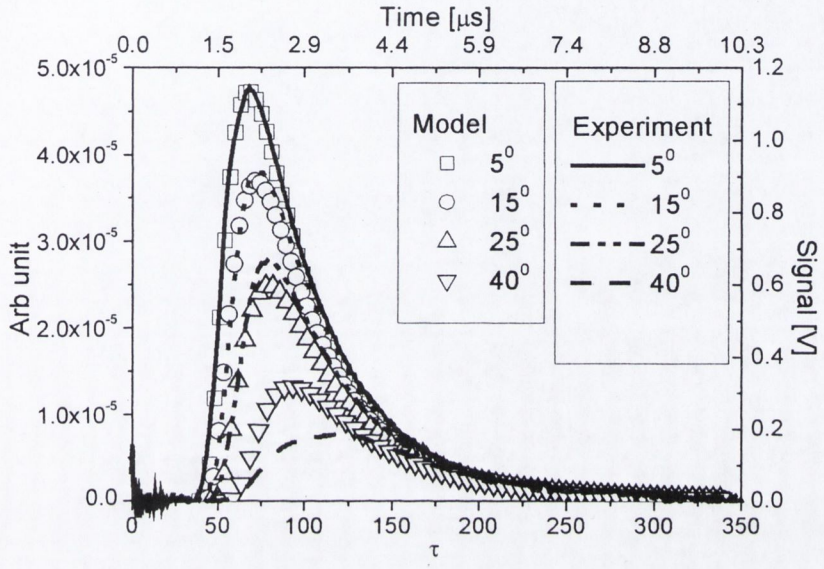

Figure B.3: Experimental time-of-flight signal for Ti-target recorded at 5 cm and 8.5 ± 1.2 J cm^{-2} (solid graphs). Time and amplitude on top- and right-axes. Also shown is the signals predicted from the isentropic expansion model (scatter graphs) on bottom and left axes.

From the expansion velocity of the front the initial sound velocity was estimated as $c_s \sim 4700$ m/s, corresponding to an initial temperature in the plume $kT_e \sim 4$ eV, see section 2.2. The calculated model particle flux shows good overall agreement in the temporal shape and relative amplitude of the signals for increasing angles are evident at least for angles up to ~ 30°.

Integrating in time the current collected by the Langmuir probe we can calculate the total number of particles (per steradian) at a given angle. Figure B.4 shows examples of the angular distributions obtained for the three different materials Al, Ti and Cu. Figure B.4(A) depicts the distribution at a distance of 5 cm and at the middle fluence (6.4 ± 0.9) J cm^{-2} for Al. The hydrodynamic model gives a good fit especially for the

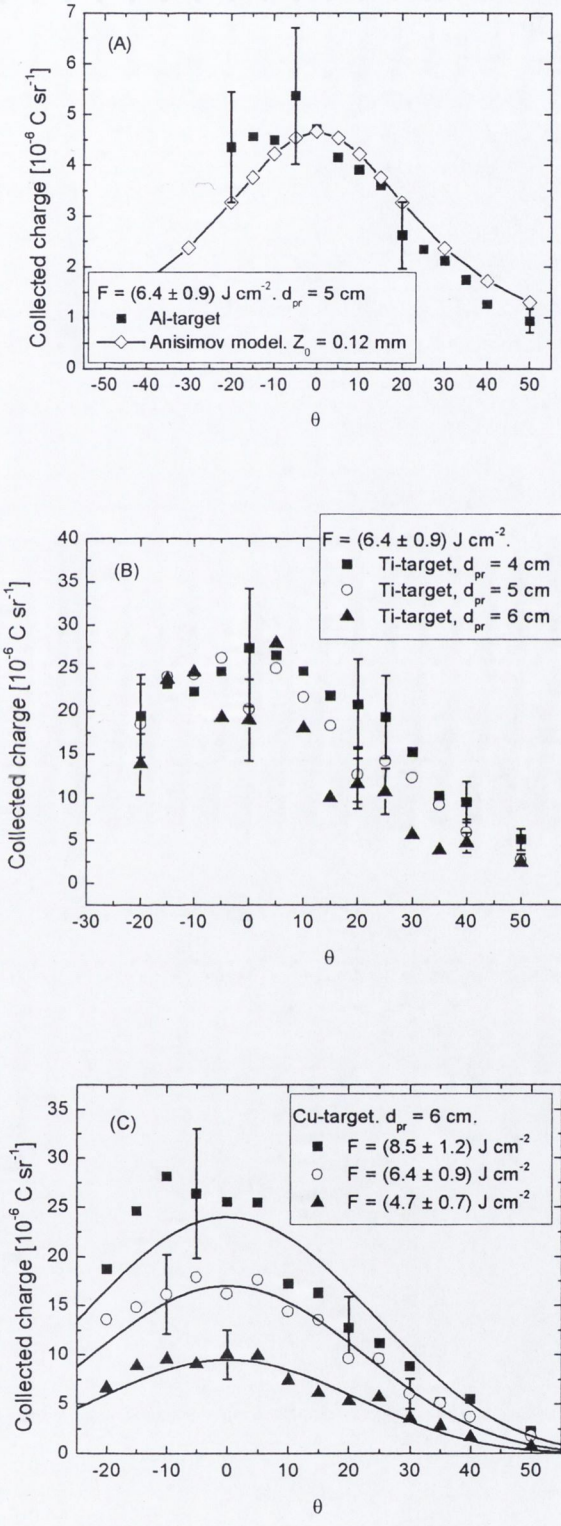

Figure B.4: Angular distributions. (A) Al-target compared to Anisimov's model. (B) Distance dependence of the charge per sterad for Ti. (C) Cu angular distribution dependence on fluence. Full curves show fit with $S \times \cos^p(\theta)$. The fit parameters (S,p) are: High fluence (24, 5.8), middle fluence (16,6.7) and low fluence (9.5, 7.5).

angles $< 40^{\circ}$ as seen also in the TOF-signals for Ti in Figure B.3. Figure B.4(B) illustrates the inertial expansion of the Ti-plume into vacuum: The charge collected per solid angle of the probe, seen from the target spot, is decreasing with increasing distance. Finally, the last Figure B.4(C) gives the fluence dependence of the angular distribution for a Cu target. As the fluence is increased a higher number of particles are detected. The solid curves show fits of the functional form $F(\theta) = S\cos^{p}(\theta)$. It was noted by [Thum-Jäger and Rohr 1999] that for the angular distribution of the charged particles only, this formula provided a good fit over the entire range of investigated materials.

Since we cannot in principle say what the charge state is of the ions we only give the collected charge per solid angle of the probe. If we assume the ions to be preferentially single charged the peak number of Ti ions (Figure B.4(B)) at (6.4 ± 0.9) J cm^{-2} is $\sim 1.5 \times 10^{14}$ sr^{-1}. This is at first surprisingly close to that reported in [Thum-Jäger and Rohr 1999] considering that Thum-Jäger and Rohr uses a much higher fluence (40 J cm^{-2}). But the longer wavelength of the laser used by those authors (Nd:YAG laser at 1.06 μm) can cause a relative lower yield compared to that of the shorter UV-laser wavelength of this experiment e.g. [Phipps and Dreyfus 1993]. The different laser wavelength used may explain also why [Buttini *et al.* 1998] reported a strong decrease in the absolute number of ablated particles with increasing target mass. That trend is not confirmed in Figure B.4 where the highest number of ablated particles is found for the Ti target followed by that of Cu and then Al.

B.1.4 Analysis and discussion

In this section we will discuss some general scaling behaviour of the results of the experiment. Figure B.5 shows the front velocity ($= d_{pr}/t_{front}$) along the target normal of the ablation plume calculated from the TOF-signals as a function of the fluence. The time of arrival at the probe of the front, t_{front}, was averaged over angles of $\theta = -5^{\circ}$, 0° and 5° and the velocity averaged over the result at the three distances. [Amoruso *et al.* 1998b] reported a steep increase in the average energy of Al up to a fluence of ~ 15 J cm^{-2}. The velocity for Cu is in good agreement with that in [Dyer 1989] and [Gutfeld and Dreyfus 1989] for similar laser and fluence conditions. Dyer also saw a steep increase in the velocity of Cu up to a fluence of ~ 5 J cm^{-2}. Gutfeld and Dreyfus reported a less steep dependence on laser fluence of $v \sim F^{0.33}$ over the range of fluences reported in Figure B.5; this scaling is assumed here for Cu and Al.

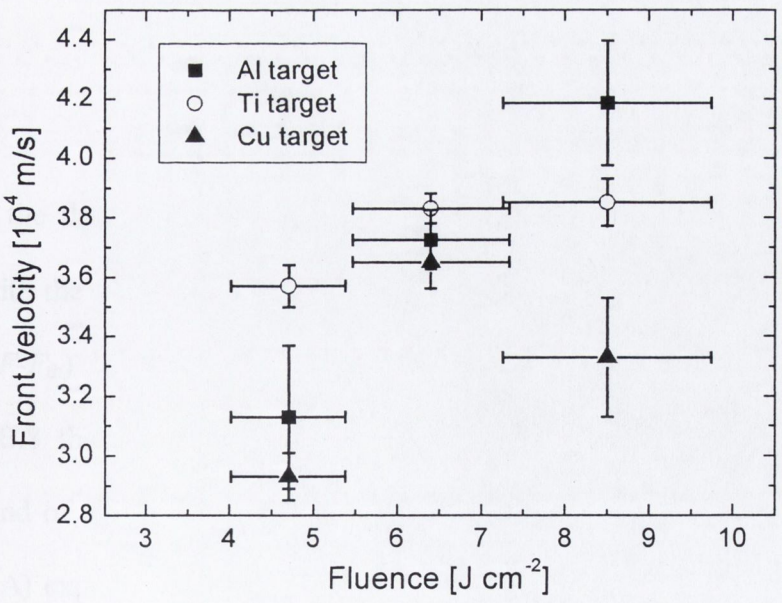

Figure B.5: Velocity *vs.* fluence.

For comparison with [Thum-Jäger and Rohr 1999] we fitted the angular distributions with the function:

$$F(\theta) = S\cos^{p}(\theta) \tag{B.2}$$

The exponent p characterises the distribution with S being a constant (dependent on irradiance parameters, e.g. fluence and wavelength). To establish the connection to Anisimov's model, we calculate the theoretical angular distribution, as shown in Figure B.4(A), and fit these with the formula (B.2) as well, Figure B.6 shows an example. This provides us with the scaling, depicted in Figure B.7, for the dependence of the exponent p on the initial thickness of the plume. From Figure B.7 it follows that according to the expansion model the exponent $p \sim \zeta_0^{-0.64}$. For comparison with experiments ζ_0 (or Z_0) is usually evaluated from the sound velocity, which in turn is taken to be proportional to the front velocity v_{front}, chapter 2.1. This means we can now write:

$$\begin{aligned} &(A)\quad p \propto \xi_0^{-0.64} \propto v_{front}^{-0.64} \propto \left(F - F_{th}\right)^{-0.64\alpha} \\ &and \\ &(B)\quad p \propto \xi_0^{-0.64} \propto \left(\tau_{laser} c_{s,0}\right)^{-0.64} \propto m_i^{0.32} \end{aligned} \tag{B.3}$$

Here F is the fluence, F_{th} is the threshold fluence and α is the scaling of the front velocity with the fluence. For a linear dependence of the velocity with the fluence we have $p \sim (F\text{-}F_{\text{th}})^{-0.64}$ while in the paper by [Gutfeld and Dreyfus 1989] $p \sim (F\text{-}F_{\text{th}})^{-0.21}$. In figure B.8 the experimental exponent p is shown as a function of fluence. An overall trend of decreasing exponent with increasing fluence is clear. The scaling of Eq. (B.3)(A) expected for the hydrodynamic expansion model is shown as well. The experiment observes nearly the scaling suggested by Equation (B.3)(A).

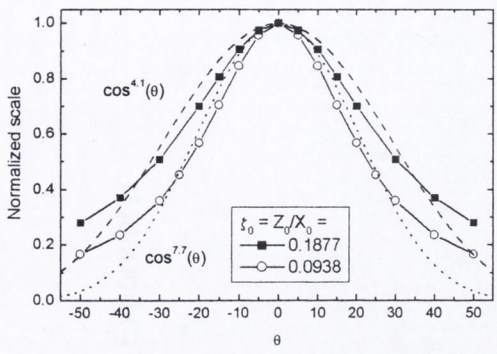

Figure B.6: $\cos^p(\theta)$ fit of the angular distribution from Anisimov's model for different initial values of the thickness to lateral dimension ratio ζ_0. Initial lateral dimension were taken for that of the beam spot in the experiment.

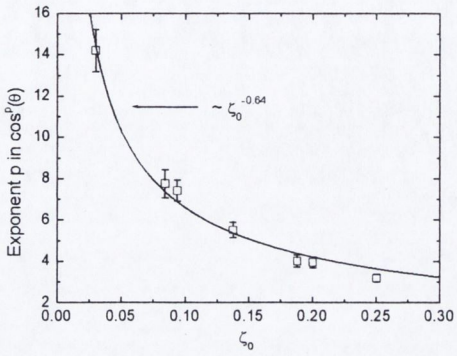

Figure B.7: Fitted $\cos^p(\theta)$ exponents of angular distributions from Anisimov's model for different values of the initial thickness to lateral dimension ratio ζ_0.

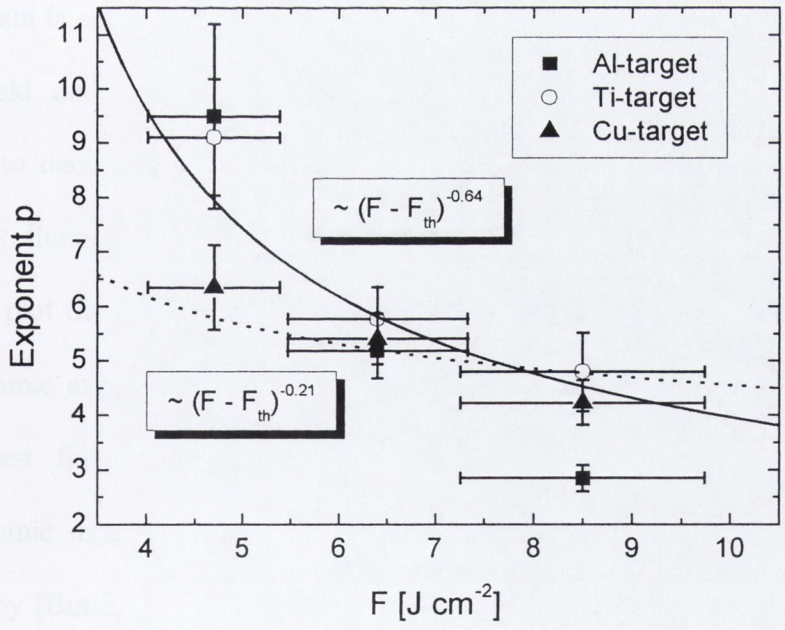

Figure B.8: Fitted $\cos^p(\theta)$ exponents of experimental angular distributions as a function of fluence F. The exponent has been averaged over the three probe distances. F_{th} was assumed to be 2 J cm^{-2} for the curves.

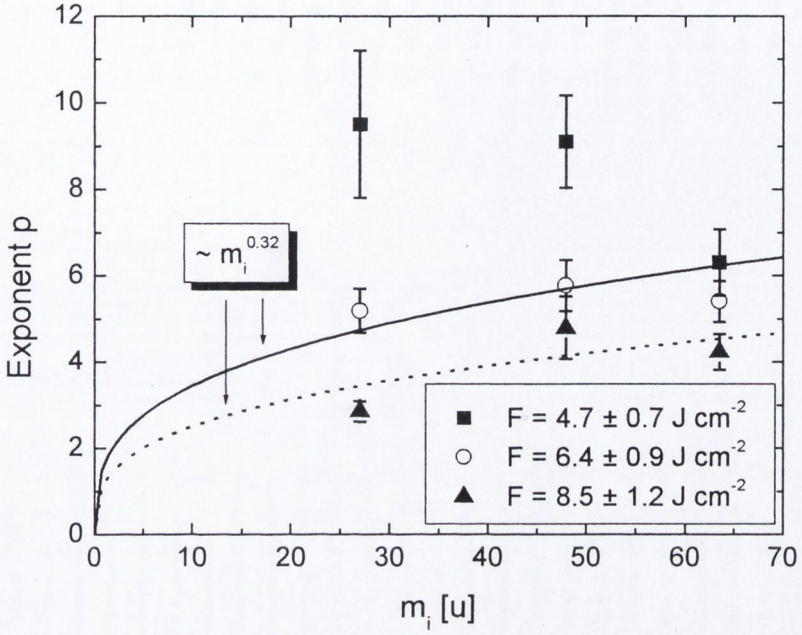

Figure B.9: Fitted $\cos^p(\theta)$ exponents of experimental angular distributions as a function of ion mass. The exponent has been averaged over the three probe distances.

The Cu data is seen to follow that expected for the velocity scaling *vs.* fluence stated by [Gutfeld and Dreyfus 1989]. However the Ti exponents would have been expected to decrease less rapidly from the slow scaling in Figure (B.5) of its front velocity *vs.* fluence

When we plot the exponent *p vs.* the ion mass and the fit from Equation (B.3)(B) the hydrodynamic expansion model is again seen to be relatively well observed for the two highest fluences used, Figure B.9. Though in agreement with that from hydrodynamic model the scaling of the exponent with the mass is less than that reported by [Buttini *et al.* 1998] who used a $\sim m_i^{1/2}$ dependence or [Thum-Jäger and Rohr 1999] who saw a $\sim m_i^{3/4}$ scaling. This could be due to the difference in irradiance parameters. The mentioned references use a more tightly focused laser spot ($0.5 - 1\times10^{-3}$ cm^2) compared to this experiment, 7.5×10^{-3} cm^2. This would lead

to larger ζ_0, and it was observed in Figure B.7, that if the fit is limited to higher ζ_0 values, p would scale with an exponent closer to 1.

B.1.5 Conclusion

Pulsed laser irradiance of metals is here investigated in a regime of higher fluences compared to that in section 5.1. The general scaling of the measured angular distribution of charge in the plume was found to follow that expected for the hydrodynamic expansion model using the initial experimental parameters. The general increase in the exponent characterising the angular distribution of the collected charge with the mass of the ions could be reproduced with the help of the model.

References

[App B] Amoruso S. Berardi V. Bruzzese R. Spinelli N. and Wang X. (1998) "*Kinetic energy distribution of ions in the laser ablation of copper targets*". Appl. Surf. Sci. **127-129**, pp 953.

[App B] Amoruso S. Armenante M. Berardi V. Bruzzese R. Velotta R. Wang X. (1998b) "*High fluence visible and ultravioled laser ablation of metallic targets*". Appl. Surf. Sci. **127-129**, pp 1017.

[App B] Amoruso S. Bruzzese R. Spinelli N. and Velotta R. (1999) "*Characterisation of laser-ablation plasmas*". J. Phys. B: At. Mol. Opt. Phys. **32**, pp R131.

[App B] Amoruso S. Berardi V. Bruzzese R. Velotta R. Spinelli N. and Wang X. (1999b) "*XeF eximer laser ablation of metallic targets probed by energy-selective time-of-flight mass spectrometry*" Appl. Surf. Sci. **138-139**, pp 250.

[App B] Anisimov S.I. Luk'yanchuk B.S. and Luches A. (1996) "*An analytical model for three-dimensional laser plume expansion into vacuum in hydrodynamic regime*". Appl. Surf. Sci. **96-98** pp 24.

[App B] Buttini E. Thum-Jäger A. Rohr K. (1998) "*The mass dependence of the jet formation in laser-produced particle beams*". J. Phys. D: Appl. Phys. **31**, pp 2165.

[App B] Chrisey D.B. and Hubler G.K. (1994) Editors "*Pulsed Laser Deposition of Thin Films*". (Wiley, New York.).

[App B] Dogget B. (1999). Final year project.

[App B] Dyer P.E. (1989) "*Electrical characterization of plasma generation in KrF laser Cu ablation*". Appl. Phys. Lett. **55**(16), pp 1630.

[App B] von Gutfeld R.J. and Dreyfus R.W. (1989) "*Electronic probe measurements of pulsed copper ablation at 248 nm*". Appl. Phys. Lett. **54**(13), pp 1212.

[App B] Hansen T.N. Scou J. and Lunney J.G. (1997) "*Angular distributions of silver ions and neutrals emitted in vacuum by laser ablation*". Euro. Phys. Lett. **40**(4), pp 441.

[App B] Jordan R. (1997) "*Development of Pulsed Laser Deposition Processes*". Ph.d. thesis. University of Dublin, Trinity College.

[App B] Koopman D.W. (1971) "*Langmuir Probe and Microwave Measurements of the Properties of Streaming Plasmas Generated by Focused Laser Pulses*". Phys. Fluids **14**(8), pp 1707.

[App B] Phipps C.R. and Dreyfus R.W. (1993) "*The high laser irradiance regime*". Eds A. Vertes, R. Gijbels and F. Adams. Chemical Analysis Series, Vol. **124**, pp 369.

[App B] Thum-Jäger A. and Rohr K. (1999) "*Angular emission distribution of neutrals and ions in laser ablated particle beams*". J. Phys. D: Appl. Phys. **32**, pp 2827.

[App B] Toftmann B. Schou J. Hansen T.N. Lunney J.G. (2000) "*Angular Distribution of Electron Temperature and Density in a Laser-Ablation Plume*". Phys. Rev. Lett. **84**(17), pp 3998.

APPENDIX C

C.1 List of publications

Refereed articles

P. Loiseleur, T.N. Hansen, J. Larour, J.G. Lunney (2001). *"Time-resolved EUV spectroscopy in the early stage of laser ablation of carbon"*. Submitted for publication.

B. Toftmann, J. Schou, T.N. Hansen, J.G. Lunney (2001). *"Evolution of the plasma parameters in the expanding laser ablation plume of silver"*. Appl. Surf. Sci. *To appear soon.*

B. Toftmann, J. Schou, T.N. Hansen, J.G. Lunney (2000). *"Angular distribution of electron temperature and density in a laser-ablation plume"*, Phys. Rev. Lett. **84**(17), pp 3998.

T.N. Hansen, J. Schou, B. Toftmann, J.G. Lunney (1999). *"Langmuir probe study of plasma expansion in pulsed laser ablation". Eds* J.S. Horwitz, H.-U Krebs, K. Murakami, M. Stuke (Springer-Verlag, 1999). Appl. Phys. A **69S**, pp S601.

T.N. Hansen, J.Schou, J.G. Lunney (1999). *"Ion time-of-flight study of laser ablation of silver in low pressure gases". Eds* D.E. Aspnes, F.H.P.M. Habraken, J. Nishizawa (Elsevier, 1999). Appl. Surf. Sci. **138-139**. pp 184.

T.N. Hansen, J. Schou, J.G. Lunney (1998). *"Angle-resolved energy distributions of laser ablated silver ions in vacuum"*. Appl. Phys. Lett. **72**, pp 1829.

W. Svendsen, J.Schou, T.N. Hansen, O. Ellegaard (1998). *"Angular distribution of emitted particles by laser ablation of silver at 355 nm"*. Appl. Phys. **A 66**, pp 493.

T.N. Hansen, J. Schou, J.G. Lunney (1997). *"Angular distribution of silver ions and neutrals emitted in vacuum by laser ablation"*. Europhys. Lett. **40**, pp 441.

Other published material

T.N. Hansen, I. Krisch, P. Choi, J. Larour, J.G. Lunney, J. Castro, A. Engel, A. Guilbert, J. Rous (2001). *"Dynamics of the EUV radiation in a fast micro-capillary plasma discharge source"*. Journal de Physique IV **11**(Pr2), pp Pr2-417.

P. Choi, J.G. Lunney, A. Engel, C. Dumitrescu, T.N. Hansen, I. Krish, J.Larour, J.Rous (1999). *"A 10^{13} A/s High Energy Density Micro Discharge Radiation Source", Eds* C. Stallings, H. Kirbie (IEEE, Piscataway, NJ, USA, 1999). 12th IEEE Int. Pulsed Power Conference **Vol I**, pp 287.

A. Engel, T.N. Hansen, P. Choi, C. Dumitrescu, J.G. Lunney, I. Krisch, J. Larour, J. Rous (1999). *"A High Brillance VUV/Soft X-Ray Microcapillary Radiation Source Powered by a 1013 A/s Compact Driver". Eds* E. Infeld, H. Rothkaehl, M. Sadowski (Polish Academy of Sciences, Warsaw, Poland, 1999). J. Techn. Phys. **40** (Poland), pp 497.

A. Engel, M. Sadowski, E. Skladnik-Sadowska, J. Larour, P. Choi, C. Dumitrescu, J.G. Lunney, T.N. Hansen, A. Guilbert, J. Rous (1999). *"Fast micro capillary discharge as a point-like source of pulsed ion beams". Eds* E. Infeld, H. Rothkaehl, M. Sadowski (Polish Academy of Sciences, Warsaw, Poland, 1999). J. Techn. Phys. **40** (Poland), pp 501.

T.N. Hansen, B.T. Christensen, J.G. Lunney, J. Schou (1998). *"Ion Dynamics and Electron Temperature of Laser Produced Plasmas in Vacuum and Low Pressure Gas". Eds* D. Riley, C.M.O. Mahony, W.G. Graham (European Physical Society, 1998). Europhysics Conference Abstract, **22H**. pp 446.